ANALYSIS OF ION EMITTING JET STRUCTURES DURING IONIC LIQUID

ELECTROSPRAYING

by

SHAWN WAYNE MILLER

A DISSERTATION

Presented to the Faculty of the Graduate School of the

MISSOURI UNIVERSITY OF SCIENCE AND TECHNOLOGY

In Partial Fulfillment of the Requirements for the Degree

DOCTOR OF PHILOSOPHY

in

AEROSPACE ENGINEERING

2015

Approved
J. L. Rovey, Advisor
K. M. Isaac
H. J. Pernicka
D. W. Riggins
B. D. Prince

PUBLICATION DISSERTATION OPTION

This dissertation is composed of the following journal articles that have been published or submitted for publication as follows:

Pages 21-52, Paper I "Electrospray of 1-Butyl-3-Methylimidazolium Dicyanamide Under Variable Flow Rate Operations" has been published in the AIAA *Journal of Propulsion and Power*, Vol. 30, No. 6, pg: 1701-1710, 2014, doi: 10.2514/1.B35170.

Pages 53-99, Paper II "Orthogonal Time-of-Flight Mass Spectrometry and Electric Field Model of 1-Butyl-3-Methylimidazolium Dicyanamide Electrospray" has been submitted (03/15/2015) to the Journal of Applied Physics and is currently under review.

ABSTRACT

The ionic liquid [Bmim][DCA] is a propellant candidate for a standalone electrospray thruster or a dual-mode propulsion system. Characterization of positive polarity ions produced by [Bmim][DCA] capillary emitters with a nominal extraction voltage of 2.0 kV within a quadrupole and time-of-flight mass spectrometers is presented along with the predictions of propulsion performance. Flow rates from 0.05 to 2.18 nL/s are used to investigate the impact variations in the flow parameter have on the electrospray plume. The retarding potential analysis reveals ions emitted from the capillary are formed below the emitter potential of 500 eV. Angular distributions indicate broadening of both the beam current and mass distribution for increasing flow rates. Derived thrust and specific impulse change from 0.84 μN and 200 s to 2.90 μN and 80 s, respectively.

Time-of-flight measurements delineate two distinct droplet distributions at approximately 2,000 to 40,000 amu/q and 50,000 to 300,000 amu/q. These multiply-charged droplet species, with wide mass-to-charge distributions, are due to the electric field conditions and associated charge range available within the parent jet. Additionally, the data show a transition to higher mass ions and droplets with increasing flow rate. The combination of two data sources allow for the assertion that ionic liquid electrospray from 0.05 to 2.18 nL/s does not conform to the traditional view of emission from the electrospray cone-jet. The mixed droplet and ion emission suggest that the primary jet disintegrates into secondary structures that are responsible for the emission species detected by the TOF instrument.

ACKNOWLEDGMENTS

I would like to acknowledge and thank my advisor, Dr. Joshua Rovey for his support and efforts while pursuing my course of study. I also thank the members of my committee for agreeing to serve on my committee and for their advice on this work. Additionally, I would like to thank the members of the Aerospace Plasma Laboratory for their support while working on this degree.

I would like to specifically recognize Drs. Benjamin Prince, Raymond Bemish, and Yu-Hui Chiu for their assistance and mentoring on this project as well as the opportunity for hands on research. In addition, past and current members of RVB Division at the Space Vehicles Directorate, Air Force Research Laboratory, Kirtland AFB are acknowledged for their contributions in discussions and moral support.

TABLE OF CONTENTS

LIST OF ILLUSTRATIONS

LIST OF TABLES

1. INTRODUCTION

This dissertation presents the work completed in examining the electrospray (also known as colloid) emission process for low flow rate conditions (i.e. flow rate < 2.2 nL/s). Specifically, this work analyzes experimentally obtained emission products, compares electric field results based on the experimental data, and provides an explanation of the origin of the emission products from the cone-jet structure. Two papers that have either been published or are intended for publication are presented on the results of research into electrospray emission. Paper I contains the electrospray results using a quadrupole mass spectrometer system and estimation of the associated propulsive output based on the measured electrospray products. Paper II describes the electrospray results using a higher mass range orthogonal time-of-flight system. Also presented is the electric field model of the cone-jet structure, the development of large mass droplets, and the associated droplet charges. The data shows that the droplets are uniform in size, but not charge, due to the effect of the surrounding electric field on the jet tip. The electric field is the driver of the charge distribution of the droplets.

1.1. MOTIVATION

The selection of space propulsion options for near Earth is currently limited to chemical combustion, cold gas, or electric propulsion (i.e. Hall effect or ion thruster). Chemical combustion does provide large, instantaneous thrust, but is inefficient and does not provide precision thrust and control. Cold gas systems require a significant storage of gas propellant in heavy high pressure tanks onboard the spacecraft resulting in extra inert mass. High pressure storage is needed due to limited densities of the gas propellants. The added inert mass outweighs the benefit of the better performance that a cold gas system can achieve. Electric propulsion is limited by scalability of the thruster system. In Hall effect thrusters, the magnetic components can only be decreased so far. In ion thrusters, space-charge limitation becomes a factor due to limits on current for a given plane gap size.

As spacecraft become smaller from masses ranging in the hundreds of kilograms to only a few kilograms[1], propulsion systems must also be reduced to handle the

precise control and low thrust needed for stationkeeping and compensation of the atmospheric drag on the spacecraft. An electrospray thruster can be easily scaled by the construction of an array of emitters and by varying the number of emitters within the array to achieve the desired propulsive performance. Additionally, electrospray has the potential for dual-mode or dual-use application where common propellants or components can be utilized by multiple systems. In the case of electrospray, a common propellant that can be emitted by electrospray and combusted for both low, efficient thrust and high thrust would enable dual-use or dual-mode operation [2-11]. This would be advantageous toward eliminating multiple propellant sources and additional mass from the spacecraft. The model system exhibiting these qualities is an ionic liquid based electrospray thruster. Busek Co. Inc. has developed an ionic liquid electrospray thruster called the Colloid Micro-Newton Thruster (CMNT) for the canceled joint ESA-NASA Laser Interferometer Space Antenna (LISA) and LISA Path Finder missions [12-14]. The requirement to meet mission goals and performance drove the design of the CMNT and little analysis went into defining the cone-jet operation. To fully understand the ionic liquid electrospray thruster, the system must be analyzed to define the emission output and performance associated with such output within the desired propellant flow rate regime. By identifying the emission products, the goal would be to work toward improving or correcting the emission toward the highly efficient pure ionic regime emission. At this point, detailed analysis has only been conducted for polar liquids such as glycerol and formamide doped with an ionic species at higher flow rates. The work that follows examines the ionic liquid electrospray emission to shed light on the species generated, the propulsive performance of such species, and identifying the origination of the species from the electrospray cone-jet at a given flow rate.

1.2. GENERAL DESCRIPTION OF A COLLOID THRUSTER

Electrospray emission is simply the electrostatic acceleration of particles to achieve a momentum change and thus thrust. Though this description sounds simplistic, in reality the electrospray process is very much electrohydrodynamic. Electrospray from a capillary style emitter is illustrated in Figure 1.1. Here, the propellant at a flow rate of Q travels down to the end of the capillary. At the end, the liquid surface tension balances

the force from an applied electric field between the capillary and extractor. The field is achieved simply by applying a voltage potential, $\Delta\Phi$, between the two electrodes of the setup. The liquid tip becomes depressed and forms a cone or more specifically a Taylor cone. From this cone, a jet is issued that is orders of magnitude smaller than the size of the cone. Based on Figure 1.1, two proposed emission zones are identified and generally accepted by most electrospray scholars. The first zone occurs at the transition region or neck of the cone-jet structure. This region results in ion emission from the surface of the liquid propellant. At the end of the jet is the second emission zone. This zone is composed of droplets to a mixed mode regime of both ions and droplets. Only in extremely low propellant flow rate and with the appropriate propellant does the emission from this region approach or obtain pure ionic [15, 16]. In most cases, obtaining a nearly pure ionic regime (PIR) is critical for most research endeavors.

   1.2.1. Taylor Cone Formation. Applying a strong electric field to a meniscus of an electrically conductive liquid results in the deformation of the liquid surface. The deformed liquid assumes a conical shape referred to as a Taylor cone, as shown in Figure 1.2. Though this reaction to an electric field hasbeen known for some time, G. I. Taylor was first to explain this phenomenon of surface deformation in 1964 through an analytical model for the cone structure. The detailed processes into the formation of the cone can be found in references [17, 18]. Here the electrostatic pressure due to the normal component of the electric field balances the surface tension of the liquid given by Eq. (1). E_n is the normal component of the electric field, γ is the surface tension of the liquid, ε_0 is the permittivity of free space, and R_c is the radius of curvature of the liquid surface. This radius is related to the distance from the tip, r, through the cotangent of α_T. The angle formed, α_T, also referred to as the Taylor angle, equates to 49.29 deg. The conductive liquid surface is assumed static and equipotential. For this surface geometry, the general solution to the Laplace equation in spherical coordinates, assuming axial symmetry, is given by Eq. (2). Here P_l is the Legendre function of order l. The restriction on Eq. (1) requires that the electric field at the cone surface be proportional to $r^{-1/2}$, therefore the potential must be proportional to $r^{1/2}$ and the order of Eq. (2) is now ½. $P_{1/2}(\cos(180 \deg - \alpha_T))$ must be zero for the cone surface to an equipotential at that θ

angle. As a result, θ = 130.7 deg = 180 deg- α_T and the resulting half angle of the Taylor cone is the Taylor angle value (49.29 deg).
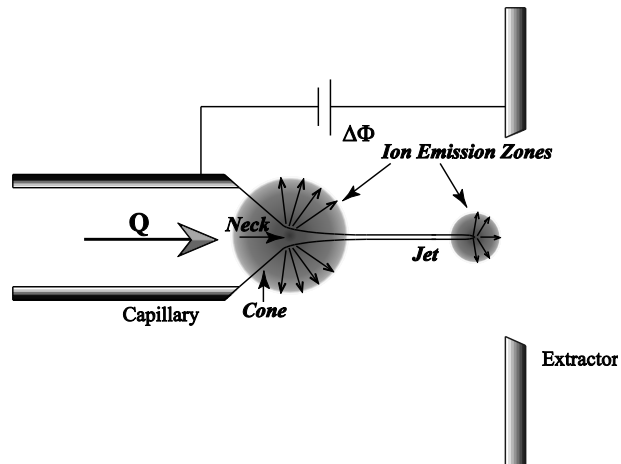
Figure 1.1. Simplified diagram of an electrospray capillary emitter and extractor assembly.
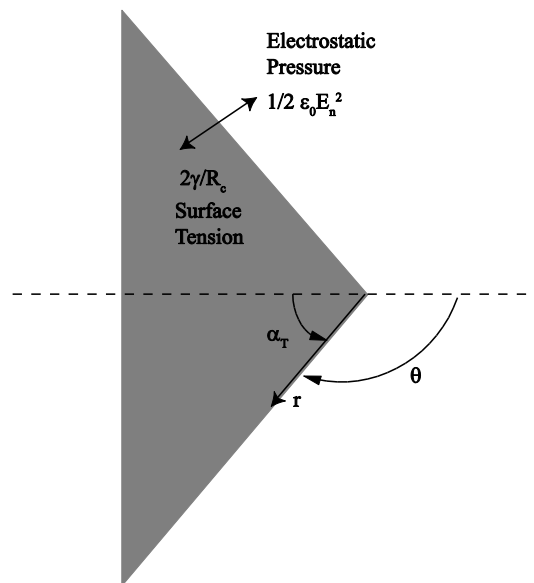
Figure 1.2. Diagram of a Taylor cone.

$$\frac{1}{2}\varepsilon_0 E_n^2 = \frac{2\gamma}{R_c} , \ R_c = r(\cot\alpha_T) \tag{1}$$

$$\Phi(r,\vartheta) = \sum_{l=0}^{\infty} r^l P_l(\cos\vartheta) \tag{2}$$

The only drawback from this model of a perfectly conical surface is that the electric field will approach infinity as r goes to zero due to the $r^{-1/2}$ dependence. This results in a nonphysical solution. In reality, two possible outcomes occur that eliminates this nonphysical solution. These possibilities are the formation of the cone-jet and ion evaporation, both of which will be discussed further.

  1.2.2. Jet Emission in the Cone-Jet Regime. At the tip of the cone, the electric field is strong enough to overcome the surface tension. As a result, the static approximation breaks down. When this happens the Taylor cone begins to operate in what is called the cone-jet mode. Here, a jet structure emanates for the cone tip and a transition region also referred to as the neck connects the two structures. Figure 1.3 provides a magnified view of the transition region between the cone and jet. Here the current transitions from being conducted by the bulk liquid, I_{tot} or I_{cd}, and into a convective current flow, I_{cv}. Essentially the liquid velocity is slow enough in the capillary that the liquid residence time, τ_{res}, is much greater than the relaxation time, τ_{rel}, of the flow. As the flow approaches the cone apex, the flow velocity increases and a singularity forms as a result of charge buildup at the apex. As a result, the jet forms from the cone and establishes a local electric field maximum. Associated with this field maximum is the radius of the transition region. It is in this region that the local field becomes maximum enough that field emission occurs. Passed the transition region the flow velocity is sufficiently high enough that all charge in the flow occurs at the surface of the jet structure. This charge forms a surface charge density, σ_{sc}, that is proportional to the electric field at a given location.

  Gamero- Castaño noted that the electric field for both the cone and jet maximize in the transition region. By solving both the electric field equations for the two unknowns of electric field and radius, Gamero-Castaño was able to determine the maximum electric field and radius as stated by Eq. (3) and (4), respectively. Here the

maximum radius indicates the radius of curvature that occurs when the cone reduces to the jet dimensions. With the electric field maximum in the transition region, this region is assumed to be the primary ion emission location of the cone-jet structure.
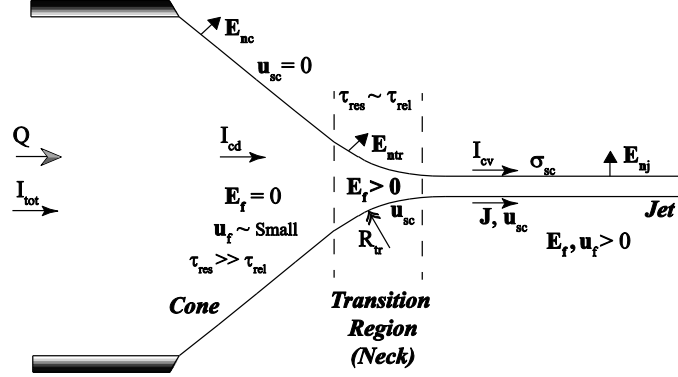
Figure 1.3. Close up view of the transition region and listed parameters as function of position.

$$E_{max} = \frac{\gamma^{1/2}}{\varepsilon_0^{2/3}} \left[\frac{K}{Q} \right]^{1/6} \tag{3}$$

$$R_{max} = \left[\frac{\varepsilon_0 Q}{K} \right]^{1/3} \tag{4}$$

In general, the jet will breakup into droplets due to fluid wave perturbations that form along the length of the jet instead of undergoing some field evaporation process as happens in the transition region. The amplitude of the perturbations increases until they are larger than the jet radius. The jet breaks up either as an axially, varicose instability or as a kink instability. Rayleigh was the first to study the breakup of liquid columns into droplets and describes the varicose instability [19]. Varicose break up can be described as sausaging of the jet and ultimately leads to droplet generation with radius of 1.89 times the nominal jet radius near the jet tip[19]. Each "sausage" of the jet reforms from a

cylindrical shape and into a spherical droplet. The kink break up is best described as a lateral whipping of the jet resulting in non-uniform sized droplet generation [20-22]. A lateral term is added to the harmonic perturbation equation describing the flow to replicate the whipping motion [23, 24]. For ion emission to occur at the end of the jet, the propellant must be volatile enough that Rayleigh instability can set in and the emitted droplets can undergo Coulombic fission. Or, the electric field must be sufficiently high that the mass flux from field evaporation (i.e. ion emission) from the surface is proportional to the mass flux arriving at the end of the jet. The cone-jet mode/structure is the most studied mode of electrospray[20-22]. The current produced by the cone-jet has been found to depend on the flow rate Q and the liquid physical properties of surface tension γ, conductivity K, and dielectric ε as seen in Eq. (5) [25-27].

$$I = f(\varepsilon)\left(\frac{\gamma K Q}{\varepsilon}\right)^{1/2} \tag{5}$$

1.2.3. Field Evaporation of Ions. For a highly conductive liquid source, it is possible for direct evaporation of ions in regions where the local electric field become strong on the cone-jet. The current emitted from these regions can be characterized by Schottky's field-enhanced thermionic emission relationship as given by Eq. (6). Here j is the current density, ε_0 is the permittivity of free space, E_n is the normal electric field, K is the Boltzmann constant, T is the liquid temperature, h is the Planck's constant, q is the ion charge, and G is the salvation energy of the bound ion. Ion emission will occur when the field condition of Eq. (7) is satisfied. G typically has a value within the range of 1-3 eV [15, 27, 28]. This value range results in the electric field needing to approach 1 V/nm for the extraction of singly charged ions.

$$j = \varepsilon_0 E_n \frac{KT}{h} e^{\frac{-1}{KT}[G-E]} \; , \; E = \sqrt{\frac{q^3 E_n}{4\pi\varepsilon_0}} \tag{6}$$

$$E_n > \frac{4\pi\varepsilon_0 G_0^2}{q^3} \tag{7}$$

1.3. EARLY COLLOID THRUSTER SYSTEMS

The use of electrospray emission has been around for several decades. Electrospray began with Zeleny's work [29-31] on electrified droplets and liquid surfaces at the beginning of the 1900's. Zeleny showed a stable cone spray issuing from a thin tube. It wasn't until 1964 that G. I. Taylor found that such a stable operating mode occurred only under specific flow and voltage conditions [17]. The balance between the electrical and surface tension stresses produced what is now known as a Taylor cone. Taylor's analytical model showed that a cone would be formed with a half-angle of 49.29 deg and he confirmed the angle experimentally. Further work by Fernández de la Mora [32] would later show that the Taylor angle of 49.29 deg was only one of many half-angles (in fact 49.29 deg is the maximum half-angle) that could be formed from a thin tube.

Focus on developing colloid or electrospray propulsion thrusters started with Krohn in the 1960's with the extraction of liquid metals and viscous organic liquids such as glycerol [33, 34]. It was in this early research that a mixed mode of emission consisting of both droplets and ions were first seen experimentally. Further works such as by Hendrick's [35] studied the effect of glycerine droplets and represent the first attempts to mathematically describe the droplet emission process. These developments were to explain the role of propellant flow rate and applied field dependence on specific charge of the colloid beam. Time-of-flight (TOF) techniques were first featured in glycerol experimentation work by Kidd [36, 37] along with Cohen [38]. Also Perel et al. [39] experimented with highly conductive liquids including Cesium and sulfuric acid (H_2SO_4). These two liquids featured emission beams containing only ions, which at the time were not of much interest. In addition, the corrosive nature (sulfuric acid) and the reactivity of a propellant which can spontaneously ignite when exposed to other elements such as water (Cesium), made such propellants not practical. During this time of early electrospray, the interest in electrospray was developing relatively large thrust densities to serve as main spacecraft propulsion engines, not necessarily precise stationkeeping. Ultimately, attention to electrospray waned as the interest into lower voltage ion engines built and a downturn in the space program occurred. It wasn't until almost two decades later did interest in electrospray slow return.

In 1989, Fenn et al. [40] revolutionized mass spectrometry and thus renewed electrospray interest. Fenn discovered that ionization of large biomolecules could be extracted intact from an electrostatic electrospray mass spectrometry without catastrophic, decomposition. Previous mass spectrometry required materials to exist as a gas without decomposing during the ionization process.   This mass spectrometry technique made use of more volatile solvents and the Rayleigh limit to achieve Coulomb fission of the emitted charge droplets. In using the Rayleigh limit, Fenn showed how to achieve, not high thrust, but low thrust and effective propellant usage by generation of smaller charged particles.

With that understanding, researchers began parametric studies such as done by Cloupeau [20-22] to evaluate how the variables going into forming a stable cone-jet influenced the performance output of the electrospray beam. These parametric studies also defined the single cone-jet electrospray structure used today. Cloupeau did show a variety of operating modes exist in electrospray, but the viable and stable mode was with a single cone-jet structure.   The 1990's research focused on using ethylene gycol, formamide, and other liquids doped with salts for electrospray extraction. The limitation on the body of works generated at this time was the size of the charged droplets and species. Instead of single ions, charged species with a mass-to-charge ratio of greater than 10,000 amu (assuming singly charged) or more were generated (see Figure 1.4). It was during this period that work by Fernández de la Mora [25], Loscertales [41], and Gañán-Calvo [42] focused on defining scaling laws relating emission current to properties such as flow rate and generated droplet diameters.

Attempts to provide a numerical model solution to the droplets were repeatedly tried by evaluating the results against experimentally collected data. In many cases, the shape of the cone was defined by use of one-dimensional Navier-Stokes equation calculated assuming axisymmetric, steady-state situations. This type of work was a feature of Hartman [23, 43-45] where droplets of 10 to 70 μm diameters were generated for flows of less than 8.0 μL/s. Hartman's modeling coincided with the compared experimental data. Higuera [46, 47] also considered modeling the generation of ions at the transition region through the use of the field-induced evaporation equation described by Iribarne and Thomson [28]. Higuera's model indicated ion evaporation provided

much of the electrical current while most of the injected still goes into droplet production. Carretero [48, 49] took the numerical solution further by incorporating a particle-in-cell component to provide a solution with beam divergence angles and allow for energy distributions to be obtained.

1.4. IONIC LIQUIDS

Ionic liquids (ILs) are molten salts for temperatures under 100 °C where the cation and anion of the liquid exist in a quasi-neutral state. More interests are in room temperature ILs due to ease of achieving advantageous physical properties with only limited application of controlling methods. ILs were first investigated because of the exhibited low vapor pressure, which allowed for easy use in vacuum environments [15, 50]. However, other physical properties besides vapor pressure tend to made ILs advantageous for electrospraying. These physical properties include a conductivity, $K \geq 1.0$ S/m, a surface tension value on the order of $\gamma \geq 0.04$ N/m, and a density of at least 1.0 g/cm^3. A IL with an conductivity of at least 1.0 S/m is more likely to achieve emission in or near the pure ionic regime if the IL flow rate is low enough [15, 51]. Table 1.1 lists a comparison of four common ILs used in electrospraying which include 1-butyl-3-methylimidazolium dicyanamide ([Bmim][DCA]), 1-ethyl-3-methylimidazolium bis(trifluromethylsulfonyl)imide ([Emim][Im]), 1-ethyl-3-methylimidazolium tetrafluoroborate ([Emim][BF$_4$]), 1-butyl-3-methylimidazolium tetrafluoroborate ([Bmim][BF$_4$]). Only the [Bmim][BF$_4$] has an conductivity of less than 1.0 S/m. Overall the ILs all possess advantageous properties as stated previously. The [Bmim][DCA] IL is featured as the primary electrospray fluid in the remainder of this dissertation.

Achieving a low mass-to-charge ratio (or high charge-to-mass ratio) is the primary feature of ILs and make ILs the predominate propellant over other electrospray propellants such as glycerol or formamide solutions. Figure 1.4 illustrates the mass-to-charge ratio obtained through electrospray of various propellants. This figure is courtesy of Romero-Sanz with some minor changes[51]. As can be seen in the figure, glycerol and formamide solutions could only generate droplets of at minimum 10^6 amu assuming singly charged species. However, ILs can achieve emission down to and including the

pure ionic regime if desired. Generally speaking, PIR is only achievable if the fluid flow rate is reduced sufficiently to minimize jet structure emission.

Table 1.1. Comparison of commonly used ionic liquids from electrospray.

Ionic Liquid	Formula	K, S/m	μ, cP	ρ, kg/m^3	γ, N/m	ε
[Bmim][DCA]	$C_{10}H_{15}N_5$	1.052 [52]	33.2 [53]	1063.1 [53]	0.0486 [54]	11.3 [55]
[Emim][Im]	$C_8H_{11}F_6N_3O_4S_2$	0.92 [56]	32.5 [56]	1519.3 [57]	0.0357 [57]	12.3 [58]
[Emim][BF$_4$]	$C_6H_{11}BF_4N_2$	1.539 [59]	36.54 [59]	1281.1 [59]	--	15 [59]
[Bmim][BF$_4$]	$C_8H_{15}BF_4N_2$	0.354 [59]	124.0 [59]	1200.0 [59]	--	--

1-butyl-3-methylimidazolium dicyanamide ([Bmim][DCA]) was used throughout this study. The initial intent was to feature a lesser known IL that exhibites hypergolicity with common oxidizers. In the case of [Bmim][DCA], white fluming nitric acid is the only know reactant to [Bmim][DCA] [60]. The molecular structure of [Bmim][DCA] is featured in Figure 1.5 in terms of the cation [Bmim] and the [DCA] anion. The [Bmim] component consists of the imidazolium ring in the center, a butyl chain extending from the left side of the ring, and the methyl group on the right. The [DCA] is a simple molecule of carbon and nitrogen with an angle of 102 deg between the two carbons. As can be seem from the structure, the [Bmim] cation is nearly twice the mass of the dicyanamide at 139 amu versus 66 amu, respectively. As such, emission of the cation is more desirable to try extracting since it is the more massive of the two ions. Thus, the experimentation segment of the work to be presented will focus on cation emission.
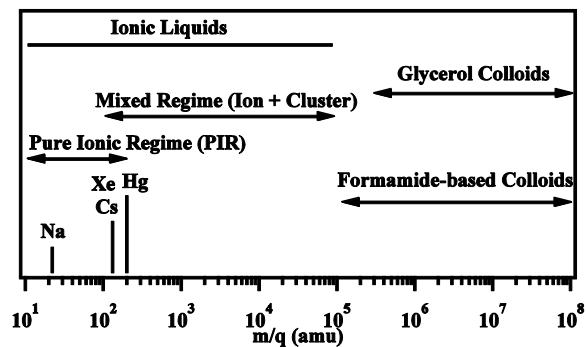
Figure 1.4. Delineation of mass-to-charge range being discussed [51].
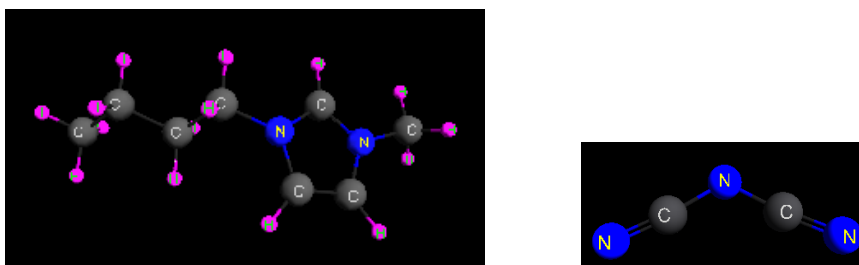
Figure 1.5. 1-butyl-3-methylimidazolium dicyanamide molecule divided into the [Bmim]$^+$ cation and [DCA]$^-$ anion.

1.5. IONIC LIQUID BASED COLLOID THRUSTERS

Romero-Sanz et al. produced one of the first publications extolling the benefits of ionic liquid based colloid thrusters [15, 51]. Through their work using a time-of-flight (TOF) data collection technique, they characterized capillary emission as a function of flow rate with a reservoir pressure from 28 to 2320 Torr. Put another way, the mass flux, as predicted by the TOF mass flux equation, was on the order of 0.5 x 10^{-12} to 112 x 10^{-12} kg/s for the same flow rate range. At these low flow rates, Romero-Sanz provided data on the 1-ethyl-3-methyl imidazolium tetrafluoroborate ([Emim][BF$_4$]) emission and indicated variable charged species output from single ions (at lowest rates) to single ions plus some droplet component.

Busek Co. Inc. developed and evaluated an 1-ethyl-3-methyl imidazolium bis(trifluoromethylsufonyl)imide ([Emim][Im]) thruster unit for use on the Laser Interferometer Space Antenna mission [12-14, 61, 62]. This thruster was to be first tested as part of the Space Technology 7 disturbance reduction system against a field emission electric propulsion (FEEP) unit. This Busek thruster demonstrated a thrust range of 4.35 to 35.8 μN with a precision of 0.08 μN. In addition, specific impulse was increased over the requirement of 150 s to a typical value of 200 s for a narrowly focused beam within a plume half angle of 23 deg. Unfortunately, funding prevented the LISA mission from proceeding as planned and last indications were for a scaled back mission to include only the FEEP thruster design.

Furthering the IL research, Chiu et al. paired an angle-resolving technique with a mass spectrometer to provide more data characterization of the electrospray beam divergence [50, 63-69]. No matter the style of emitter, the angle-resolving mass spectrometer could evaluate for beam current, mass flow rate, ion potential, and beam ion composition. The system developed by Chiu excelled at detecting small ions from ionic liquid ion sources or surface etched style emitters. For low mass flow rates, it was easy to record the beam composition up to 1000 amu for singly charged species. Chiu repeatedly indicated the presence of mass greater than 1000 amu in almost all studies suggesting some component as droplet. Whether this mass indication was due to a near 1000 amu charged species or some other larger masses remainsunknown.

REFERENCES

[1] Konecny, G., "Small Satellites-A Tool for Earth Observation?," *XXth ISPRS Congress Commission IV*, Instanbul, Turkey, 2004.

[2] Berg, S. P., Coleman, B. and Rovey, J. L., "Decomposition of Ionic Liquid Ferrofluids for Multi-Mode Spacecraft Propulsion," *50th AIAA/ASME/SAE/ASEE Joint Propulsion Conference*, Cleveland, OH, AIAA Paper 2014-3568, 2014.

[3] Berg, S. P. and Rovey, J. L., "Ignition Evaluation of Monopropellant Blends of HAN and Imidazole-Based Ionic Liquid Fuels," *50th Aerospace Sciences Meeting*, Nashville, TN, AIAA Paper 2012-0974, 2012.

[4] Berg, S. P. and Rovey, J. L., "Dual-Mode Propellant Properties and Performance Analysis of Energetic Ionic Liquids," *50th Aerospace Sciences Meeting*, Nashville, TN, AIAA Paper 2012-0975, 2012.

[5] Berg, S. P. and Rovey, J. L., "Assessment of Imidazole-Based Ionic Liquids as Dual-Mode Spacecraft Propellants," *Journal of Propulsion and Power*, Vol. 29, No. 2, 2013, pp. 339-351.

[6] Berg, S. P. and Rovey, J. L., "Decomposition of Monopropellant Blends of Hydroxylammonium Nitrate and Imidazole-Based Ionic Liquid Fuels," *Journal of Propulsion and Power*, Vol. 29, No. 1, 2012, pp. 125-135.

[7] Berg, S. P. and Rovey, J. L., "Performance Analysis of an Integrated Multi-Mode Chemical Monopropellant Inductive Plasma Thruster," *49th AIAA/ASME/SAE/ASEE Joint Propulsion Conference*, San Jose, CA, AIAA Paper 2013-3956, 2013.

[8] Berg, S. P. and Rovey, J. L., "Assessment of Multi-Mode Spacecraft Micropropulsion Systems," *50th AIAA/ASME/SAE/ASEE Joint Propulsion Conference*, Cleveland, OH, AIAA Paper 2014-3758, 2014.

[9] Berg, S. P. and Rovey, J. L., "Assessment of High-Power Electric Multi-Mode Spacecraft Propulsion Concepts," *33rd International Electric Propulsion Conference*, Washington D.C., IEPC-2013-308, 2013.

[10] Donius, B. R. and Rovey, J. L., "Ionic Liquid Dual-Mode Spacecraft Propulsion Assessment," *Journal of Spacecraft and Rocket*, Vol. 48, No. 1, 2011, pp. 110-123.

[11] Donius, B. R. and Rovey, J. L., "Analysis and Prediction of Dual-Mode Chemical and Electric Ionic Liquid Propulsion Preformance," *48th Aerospace Sciences Meeting*, Orlando, FL, AIAA Paper 2010-1328, 2010.

[12] Gamero-Castaño, M., Hruby, V., Spence, D., Demmons, N., McCormick, R., Gasdaska, C. and Falkos, P., "Micro Newton Colloid Thruster for ST7-DRS Mission," *39th AIAA/ASME/SAE/ASEE Joint Propulsion Conference and Exhibit*, Huntsville, AL, AIAA Paper 2003-4543, 2003.

[13] Hruby, V., Gamero-Castaño, M., Spence, D., Gasdaska, C., Demmons, N. and Connolly, W., "Colloid Thrusters for the New Millennium, ST7 DRS Mission," *IEEE Aerospace Conference*, 2004.

[14] Hruby, V., Spence, D., Demmons, N., Roy, T., Ehrbar, E., Zwahlen, J., Martin, R., Ziemer, J., Connolly, W., Rhodes, S. and Tolman, W., "ST7-DRS Colloid Thruster System Development and Performance Summary," *44th AIAA/ASME/SAE/ASEE Joint Propulsion Conference & Exhibit*, Hartford, CT, AIAA Paper 2008-4824, 2008.

[15] Romero-Sanz, I., Bocanegra, R., Fernandez de la Mora, J. and Gamero-Castaño, M., "Source of Heavy Molecular Ions Based on Taylor Cones of Ionic Liquids Operating in the Pure Ion Evaporation Regime," *Journal of Applied Physics*, Vol. 94, No. 5, 2003, pp. 3599-3605.

[16] Mahoney, J. F., Moore, R. D., Perel, J., Yahiku, A. Y., Ayoub, N. S. and Reitz, R. D., "Research and Development of a Charged-Particle Bipolar Thruster," *AIAA Journal*, Vol. 7, No. 3, 1969, pp. 507-511.

[17] Taylor, G. I., "Disintegration of Water Drops in an Electric Field," *Proceedings of the Royal Society of London. Series A, Mathematical and Physical Sciences*, Vol. 280, No. 1382, 1964, pp. 383-397.

[18] Fernández de la Mora, J., "The Fluid Dynamics of Taylor Cones," *Annual Review of Fluid Mechanics*, Vol. 39, No. 1, 2007, pp. 217-243.

[19] Rayleigh, L., "On the Instability of Jets," *Proceeding of the London Mathematical Society*, Vol. 10, No. 1878, pp. 4-13.

[20] Cloupeau, M. and Prunet-Foch, B., "Electrohydrodynamic Spraying Functioning Modes: A Critical Review," *Journal of Aerosol Science*, Vol. 25, No. 6, 1994, pp. 1021-1036.

[21] Cloupeau, M. and Prunet-Foch, B., "Electrostatic Spraying of Liquids in Cone-Jet Mode," *Journal of Electrostatics*, Vol. 22, No. 2, 1989, pp. 135-159.

[22] Cloupeau, M. and Prunet-Foch, B., "Electrostatic Spraying of Liquids: Main Functioning Modes," *Journal of Electrostatics*, Vol. 25, No. 2, 1990, pp. 165-184.

[23] Hartman, R. P. A., Brunner, D. J., Camelot, D. M. A., Marijnissen, J. C. M. and Scarlett, B., "Jet Break-up in Electrohydrodynamic Atomization in the Cone-Jet Mode," *Journal of Aerosol Science*, Vol. 31, No. 1, 2000, pp. 33.

[24] Mestel, A. J., "Electrohydrodynamic Stability of a Highly Viscous Jet," *Journal of Fluid Mechanics*, Vol. 312, No. 1996, pp. 311-326.

[25] Fernández de la Mora, J. and Loscertales, I. G., "The Current Emitted by Highly Conducting Taylor Cones," *Journal of Fluid Mechanics*, Vol. 260, No. 1, 1994, pp. 155-184.

[26] Gamero-Castaño, M. and Fernandez de la Mora, J., "Direct Measurement of Ion Evaporation Kinetics from Electrified Liquid Surfaces," *Journal of Chemical Physics*, Vol. 113, No. 2, 2000, pp. 815-832.

[27] Lozano, P. C., "Studies on the Ion-Droplet Mixed Regime in Colloid Thrusters," PhD Dissertation, Aeronautics and Astronautics Dept., Massachusetts Institute of Technology, Cambridge, MA, 2003.

[28] Iribarne, J. V. and Thomson, B. A., "On the Evaporation of Small Ions from Charged Droplets," *The Journal of Chemical Physics*, Vol. 64, No. 6, 1976, pp. 2287-2294.

[29] Zeleny, J., "The Electrical Discharge from Liquid Points, and a Hydrostatic Method of Measuring the Electric Intensity at their Surfaces," *The Physical Review*, Vol. 3, No. 2, 1914, pp. 69-91.

[30] Zeleny, J., "Instability of Electrified Liquid Surfaces," *The Physical Review*, Vol. 10, No. 1, 1917, pp. 1-6.

[31] Zeleny, J., "On the Conditions of Stability of Electrified Drops, with Applications to the Electrical Discharge from Liquid Points," *Proceeding of Cambridge Philosophy Society*, Vol. 18, No. 1915, pp. 71-83.

[32] Fernández de la Mora, J., "The Effect of Charge Emission from Electrified Liquid Cones," *Journal of Fluid Mechanics*, Vol. 243, No. 1992, pp. 561-574.

[33] Krohn, V. E., "Liquid Metal Droplets for Heavy Particle Propulsion," *Electrostatic Propulsion*, American Institute of Aeronautics and Astronautics, 1961, pp. 73-80.

[34] Krohn, V. E., "Glycerol Droplets for Electrostatic Propulsion," *Electric Propulsion Development*, American Institute of Aeronautics and Astronautics, 1963, pp. 435-440.

[35] Hendricks, C., "Parametric Studies of Electrohydrodynamic Spraying," *AIAA 5th Electric Propulsion Conference*, San Diego, CA, AIAA Paper 1966-252, 1966.

[36] Kidd, P. W., "Parametric Studies with a Single-Needle Colloid Thruster," *Journal of Spacecraft and Rockets*, Vol. 5, No. 9, 1968, pp. 1034-1039.

[37] Kidd, P. W. and Shelton, H., "Life Test (4350 Hours) of an Advanced Colloid Thruster Module," *AIAA 10th Electric Propulsion Conference*, Lake Tahoe, NV, AIAA Paper 1973-1078, 1973.

[38] Cohen, E., Somol, C. J. and Gordon, D. A., "A 100-kV, 10-W Heavy-Particle Thrustor," *AIAA Second Annual Meeting*, San Francisco, CA, AIAA Paper 1965-377, 1965.

[39] Perel, J., Bates, T., Mahoney, J., Moore, R. D. and Yahiku, A. Y., "Research on a Charged Particle Bipolar Thruster," *AIAA Electric Propulsion and Plasmadynamics Conference*, Colorado Springs, CO, AIAA Paper 1967-728, 1967.

[40] Fenn, J. B., Mann, M., Meng, C. K., Wang, S. K. and Whitehouse, C., "Electrospray Ionization for Mass Spectrometry of Large Biomolecules," *Science*, Vol. 246, No. 1, 1989, pp. 64-71.

[41] Loscertales, I. G. and Fernández de la Mora, J., "Experiments on the Kinetics of Field Evaporation of Small Ions from Droplets," *The Journal of Chemical Physics*, Vol. 103, No. 12, 1995, pp. 5041-5060.

[42] Gañán-Calvo, A. M., "Cone-Jet Analytical Extension of Taylor's Electrostatic Solution and the Asymptotic Universal Scaling Laws in Electrospraying," *Physical Review Letters*, Vol. 79, No. 2, 1997, pp. 217-220.

[43] Hartman, R. P. A., Borra, J. P., Brunner, D. J., Marijnissen, J. C. M. and Scarlett, B., "The Evolution of Electrohydrodynamic Sprays Produced in the Cone-Jet Mode, A Physical Model," *Journal of Electrostatics*, Vol. 47, No. 3, 1999, pp. 143-170.

[44] Hartman, R. P. A., Brunner, D. J., Camelot, D. M. A., Marijnissen, J. C. M. and Scarlett, B., "Electrohydrodynamic Atomization in the Cone-Jet Mode Physical Modeling of the Liquid Cone and Jet," *Journal of Aerosol Science*, Vol. 30, No. 7, 1999, pp. 823-849.

[45] Hartman, R. P. A., Marijnissen, J. C. M. and Scarlett, B., "Electrohydrodynamic Atomization in the Cone-Jet Mode. A Physical Model of the Liquid Cone and Jet," *Journal of Aerosol Science*, Vol. 28, No. Suppl. 1, 1997, pp. S527-S528.

[46] Higuera, F. J., "Flow Rate and Electric Current Emitted by a Taylor Cone," *Journal of Fluid Mechanics*, Vol. 484, No. 2003, pp. 303-327.

[47] Higuera, F. J., "Ion Evaporation from the Surface of a Taylor Cone," *Physical Review E*, Vol. 68, No. 1, 2003, pp. 016304.

[48] Carretero, J. and Martinez-Sanchez, M., "Quasi-One-Dimensional Numerical Simulation of a Single-Emitter Colloidal Jet," *38th AIAA/ASME/SAE/ASEE Joint Propulsion Conference & Exhibit*, AIAA Paper AIAA 2002-3812, 2002.

[49] Carretero, J. A., Lozano, P. and Martinez-Sanchez, M., "Numerical Simulation of Taylor Cone-Jets and Colloid Thruster Plumes," *Proceedings of the 4th International Spacecraft Propulsion Conference*, Vol. No. 2004, pp. 8.

[50] Chiu, Y. and Dressler, R. A., "Ionic Liquids for Space Propulsion," *Ionic Liquids IV: Not Just Solvents Anymore*, American Chemical Society, Washington DC, 2007, pp. 138-161.

[51] Romero-Sanz, I., Aguirre de Carcer, I. and Fernandez de La Mora, J., "Ionic Propulsion Based on Heated Taylor Cones of Ionic Liquids," *Journal of Propulsion and Power*, Vol. 21, No. 2, 2005, pp. 239-242.

[52] Zech, O., Stoppa, A., Buchner, R. and Kunz, W., "The Conductivity of Imidazolium-Based Ionic Liquids from (248 to 468) K. B.Variation of the Anion," *Journal of Chemical and Engineering Data*, Vol. 55, No. 5, 2010, pp. 1774-1778.

[53] Carvalho, P. J., Regueira, T., Santos, L. M. N. B. F. and Coutinho, J. A. P., "Effect of Water on the Viscosities and Densities of 1-Butyl-3-methylimidazolium Dicyanamide and 1-Butyl-3-methylimidazolium Tricyanomethane at Atmospheric Pressure," *Journal of Chemical and Engineering Data*, Vol. 55, No. 2, 2010, pp. 645-652.

[54] Sánchez, L. G., Espel, J. R., Onink, F., Meindersma, G. W. and de Haan, A. B., "Density, Viscosity, and Surface Tension of Synthesis Grade Imidazolium, Pyridinium, and Pyrrolidinium Based Room Temperature Ionic Liquids," *Journal of Chemical and Engineering Data*, Vol. 54, No. 10, 2009, pp. 2803-2812.

[55] Stoppa, A., Hunger, J., Buchner, R., Hefter, G., Thoman, A. and Helm, H., "Interactions and Dynamics in Ionic Liquids," *The Journal of Physical Chemistry B*, Vol. 112, No. 16, 2008, pp. 4854-4858.

[56] Schreiner, C., Zugmann, S., Hartl, R. and Gores, H. J., "Fractional Walden Rule for Ionic Liquids: Examples from Recent Measurements and a Critique of the So-Called Ideal KCl Line for the Walden Plot," *Journal of Chemical & Engineering Data*, Vol. 55, No. 5, 2009, pp. 1784-1788.

[57] Wandschneider, A., Lehmann, J. K. and Heintz, A., "Surface Tension and Density of Pure Ionic Liquids and Some Binary Mixtures with 1-Propanol and 1-Butanol," *Journal of Chemical & Engineering Data*, Vol. 53, No. 2, 2008, pp. 596-599.

[58] Weingärtner, H., "The Static Dielectric Constant of Ionic Liquids," *Zeitschrift für Physikalische Chemie*, Vol. 220, No. 10, 2006, pp. 1395-1405.

[59] Donius, B. R., "Investigation of Dual-Mode Spacecraft Propulsion by Means of Ionic Liquids," Masters Thesis, Mechanical and Aerospace Engineering Dept., Missouri University of Science and Technology, Rolla, MO, 2010.

[60] Schneider, S., Hawkins, T., Rosander, M., Vaghjiani, G., Chambreau, S. and Drake, G., "Ionic Liquids as Hypergolic Fuels," *Energy & Fuels*, Vol. 22, No. 4, 2008, pp. 2871-2872.

[61] Ziemer, J., Randolph, T., Franklin, G. W., Hruby, V., Spence, D., Demmons, N., Roy, T., Ehrbar, E., Zwahlen, J., Martin, R. and Connolly, W., "Delivery of Colloid Micro-Newton Thrusters for the Space Technology 7 Mission," *44th AIAA/ASME/SAE/ASEE Joint Propulsion Conference & Exhibit*, Hartford, CT, AIAA Paper 2008-4826, 2008.

[62] Ziemer, J. K., Randolph, T. M., Franklin, G. W., Hruby, V., Spence, D., Demmons, N., Roy, T., Ehrbar, E., Zwahlen, J., Martin, R. and Connolly, W., "Colloid Micro-Newton Thrusters for the Space Technology 7 Mission," *IEEE Aerospace Conference*, Big Sky, MT, AIAA Paper, 2010.

[63] Ticknor, B. W., Anderson, J. K., Fritz, B. A. and Chiu, Y.-H., "Effect of Aspect Ratio on the Wettability and Electrospray Properties of Porous Tungsten Emitters with the Ionic Liquid [Emim][Im]," *46th AIAA/ASME/SAE/ASEE Joint Propulsion Conference & Exhibit*, Nashville, TN, AIAA Paper 2010-6618, 2010.

[64] Ticknor, B. W., Miller, S. W. and Chiu, Y. H., "Mass Spectrometric Analysis of the Electrospray Plume from an Externally Wetted Tungsten Ribbon Emitter," *45th AIAA/ASME/SAE/ASEE Joint Propulsion Confernce & Exhibit*, Denver,CO, AIAA Paper 2009-5088, 2009.

[65] Chiu, Y., Austin, B., Dressler Rainer, A., Levandier, D., Murray, P. T., Lozano, P. and Martinez-Sanchez, M., "Mass Spectrometric Analysis of Colloid Thruster Ion Emission from Selected Propellants," *Journal of Propulsion and Power*, Vol. 21, No. 3, 2005, pp. 416-423.

[66] Chiu, Y., Gaeta, G., Heine, T. R., Dressler, R. A. and Lavandier, D. J., "Analysis of the Electrospray Plume from the EMI-Im Propellant Externally Wetted on a Tungsten Needle," *42nd AIAA/ASME/SAE/ASEE Joint Propulsion Conference & Exhibit*, Sacramento, CA, AIAA Paper 2006-5010, 2006.

[67] Chiu, Y., Gaeta, G., Levandier, D. J., Dressler, R. A. and Boatz, J. A., "Vacuum Electrospray Ionization Study of the Ionic Liquid, [Emim][Im]," *International Journal of Mass Spectrometry*, Vol. 265, No. 2-3, 2007, pp. 146-158.

[68] Chiu, Y., Levandier, D., Austin, B., Dressler Rainer, A., Murray, P. T., Lozano, P. and Martinez-Sanchez, M., "Mass Spectrometric Analysis of Ion-Emission from Selected Colloid Thruster Fuels," *39th AIAA/ASME/SAE/ASEE Joint Propulsion Conference and Exhibit*, Huntsville, AL, AIAA Paper 2003-4848, 2003.

[69] Prince, B. D., Fritz, B., A. and Chiu, Y.-H., "Ionic Liquids in Electrospray Propulsion Systems," *Ionic Liquids: Science and Applications*, American Chemical Society, 2012, pp. 27-49.

PAPER

I. ELECTROSPRAY OF 1-BUTYL-3-METHYLIMIDAZOLIUM DICYANAMIDE UNDER VARIABLE FLOW RATE OPERATIONS

Shawn W. Miller, Benjamin D. Prince, and Raymond J. Bemish

Air Force Research Laboratory, Space Vehicles Directorate, Kirtland AFB, NM, 87117

Joshua L. Rovey

Missouri University of Science and Technology, Rolla, MO, 65409

ABSTRACT

The ionic liquid [Bmim][DCA] is a propellant candidate for a standalone electrospray thruster or a dual-mode propulsion system. Characterization of positive polarity ions produced by [Bmim][DCA] capillary emitters with a nominal extraction voltage of 2.0 kV is presented, followed by predictions of propulsion performance. Flow rates from 0.27 to 2.18 nanoliters per second (nL/s) are used to investigate the impact variations in the flow parameter have on the electrospray plume. Measurements indicate the presence of $Bmim([Bmim][DCA])_n^+$ ($n = 0, 1, 2, 3, 4$) cation species plus droplet contributions. At 0.27 nL/s the $n = 1$ species dominates the mass spectrum contributing 56.5% of the total intensity, while at 2.18 nL/s the dominant species is $n = 4$ comprising 40.7%. Based on the retarding potential analysis, ions emitted from the capillary are formed below the emitter potential of 500 eV. Angular distributions indicate broadening of both the beam current and mass distribution for increasing flow rates. As flow rate increases from 0.30 to 2.18 nL/s, derived thrust and specific impulse change from 0.84 μN and 200 s to 2.90 μN and 80 s, respectively.

NOMENCLATURE

F = thrust (N)

g = acceleration of gravity (m/s^2)

I = total beam current (A)

I_{sp} = specific impulse (s)

K = ionic liquid electrical conductivity (S/m)

$\dot{m}$ = total mass flow rate (kg/s)

m/q = mass-to-charge ratio (amu/e)

P_e = electrical power (W)

P_0 = reservoir pressure (Torr)

Q = ionic liquid volumetric flow rate (nL/s)

q/m = specific charge (C/kg)

v = propellant ejection velocity (m/s)

V_{acc} = acceleration potential (V)

V_{Ext} = extractor plate potential (V)

V_N = emitter potential (V)

V_Ω = potential due to ohmic losses (V)

γ = ionic liquid surface tension (N/m)

ε = ionic liquid dielectric constant

ε_0 = permittivity of free space (F/m)

μ = ionic liquid viscosity (cP)

ρ = ionic liquid density (kg/m^3)

1. INTRODUCTION

Electrospray thrusters are a class of micro-electric propulsion systems that field evaporate a conductive liquid propellant. Liquid flows to the tip of the electrospray emitter where a strong electric field is present. Under the right conditions of flow rate and field strength, a cone structure (i.e., Taylor cone [1]) develops at the tip of the emitter. This cone results from the balance between the pull of the surface tension of the liquid and of the applied electric field. Two ion emission zones have been proposed for the Taylor cone (see Figure 1.1) [2-5]. The first zone is at the transition region between the cone and jet structure known as the neck. The second zone occurs at the jet breakup region located at the jet tip. Along with small ions, larger charged masses have been detected from this second emission zone. Early studies of electrospray (also termed colloid) thrusters used glycerol or salt solutions as propellants. More recently the choice propellants are molten salts known as ionic liquids (ILs), specifically, room-temperature ionic liquids [6, 7]. A common IL frequently used in electrospray research has been [Emim][Im] (1-ethyl-3-methylimidazolium bis(trifluromethylsulfonyl)imide), which has a conductivity of 0.92 Siemens per meter (S/m) and a viscosity of 32.6 centipoise (cP) at 298 K [8]. These properties facilitate ion extraction at low voltages (i.e., < 3kV) in a single cone-jet mode.

This paper focuses on another IL, [Bmim][DCA] (1-butyl-3-methylimidazolium dicyanamide), that has received less attention as an electrospray propellant under controlled variable flow rate operation. Interest in [Bmim][DCA] stems from its potential to serve as both a chemical propulsion and electrospray propellant, enabling what is called a dual-mode or multi-mode propulsion system. [Bmim][DCA] exhibits physical properties (see Table 1.1) similar to [Emim][Im] including an ease of electrospraying [9-15]. Additionally, the heat of formation of [Bmim][DCA] is double that of hydrazine (206.2 kJ/mol vs. 109.3 kJ/mol for hydrazine) making it a potential candidate for chemical propulsion [16]. Experimental and numerical studies have explored the use of [Bmim][DCA] in chemical engine applications. Schneider et al. [17] studied a variety of liquids with fuel-rich anions, which included liquids with the dicyanamide anion. The study found [Bmim][DCA] to be hypergolic with white fuming

nitric acid (WFNA) resulting in an ignition delay time of 47 ms; longer than the desired maximum of 5 ms. Numerical predictions by Berg and Rovey [18, 19] suggest that pure [Bmim][DCA] has a 20% lower specific impulse than hydrazine, but that a binary combination of [Bmim][DCA] with hydroxylammonium nitrate (HAN) oxidizer may equal or exceed hydrazine performance. Additionally, spacecraft models by Donius and Rovey [20, 21] show that mass savings through common propellant for a dual-mode system more than offset the mass penalty associated with lower performance.
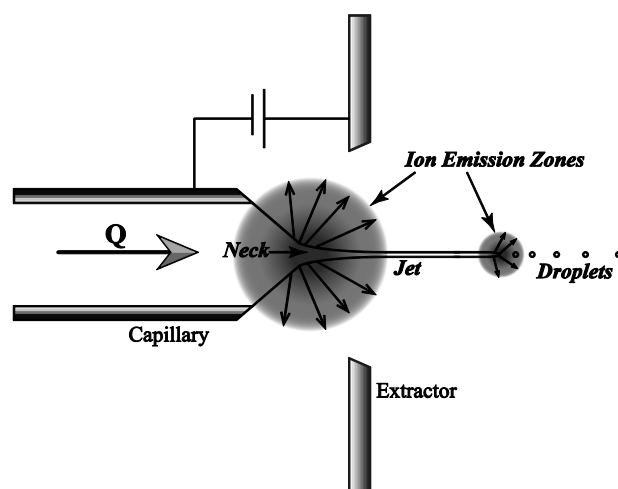
Figure 1.1. Taylor Cone Structure and Ion Emission Zones of a Capillary Emitter.

Table 1.1. Physical properties of the IL [Bmim][DCA] compared to [Emim][Im] at temperature of 298 K.

Ionic Liquid	Formula	K, S/m	μ, cP	ρ, kg/m^3	γ, N/m	ε
[Bmim][DCA]	$C_{10}H_{15}N_5$	1.052	33.2	1063.1	0.0486	11.3
		[10]	[11]	[11]	[12]	[13]
[Emim][Im]	$C_8H_{11}F_6N_3O_4S_2$	0.92	32.5	1519.3	0.0357	12.3
		[8]	[8]	[14]	[14]	[15]

An option for expanding the capability of a capillary electrospray emitter is the use of controlled variable flow rate operations. While this control method has been known for some time, there has been limited research on its implementation and the independent effect of flow rate on electrospray operation. Cloupeau and Prunet-Foch [22] conducted the earliest direct flow control while studying electrospray operating modes and cone-jet mode sprays. These investigations focused on varying electrospray parameters to determine the effect on the observable emission modes (e.g. jet geometry). They investigated how voltage, beam current, and droplet frequency depended on flow rate. The studied flow rate range was 1.0 nanoliters per second (nL/s) to 10 microliters per second (μL/s) for liquids of various conductivities. Gamero-Castaño and Hruby [23] studied the effect of flow rate on beam current and ultimately thrust and I_{sp}. The flow rate was also compared to the flux measured by time-of-flight techniques. For [Emim][Im] emitted at the two flow rates of 0.36 nL/s and 0.14 nL/s, beam current and I_{sp} changed from 307 nA and 126 s to 216 nA and 171 s as thrust output dropped from 0.628 μN to 0.352 μN. Romero-Sanz et al. [6] later conducted a flow controlled experiment for the IL [Emim][BF$_4$] (1-ethyl-3-methylimidazolium tetrafluoroborate) similar to the [Bmim][DCA] study that follows, where a range of backing pressures was explored: 28 to 2310 torr. Only the three smallest cations (i.e., $Emim^+$, $Emim([Emim][BF_4])^+$, $Emim([Emim][BF_4])_2^+$) were distinguishable in the data and were assigned associated currents at each pressure setting. The remaining current that could not be assigned to the small cations was classified as droplet contribution. This droplet contribution consists of all charged species of greater mass than the three cations. For each of the three cations, the current increased to a maximum then decreased as pressure increased; while the current of the droplet contribution increased over the entire pressure range. These current vs. pressure trends suggest a beam composition change as a function of flow rate.

This study investigates emission of the IL [Bmim][DCA] from an internal flow capillary and characterize the [Bmim][DCA] electrospray plume. Experimental results are then used to predict the electrospray propulsion performance of [Bmim][DCA]. By characterizing the plume and predicting performance, the aim is to determine the variability and tunability of the electrospray plume to specific ion emission products and thus specific propulsion performance levels through flow rate adjustment.

2. EXPERIMENT

To predict the electrospray performance, it is necessary to measure current and mass flow rate. Additionally, the ion mass intensities and kinetic energies are measured to ascertain the electrospray beam composition. These measurements are accomplished using the angle-resolved technique detailed by Chiu et al. [24, 25] This technique is chosen over the time-of-flight (TOF)/stopping potential approach due to improved resolution in identifying the ionic species (or m/q ratio) produced in the electrospray cone-jet operation mode and collection of complementary TOF information. In addition, this apparatus is relatively insensitive to the ion energy distribution and allows for energy distribution measurements of the mass-resolved ionic species. To establish the impact of beam divergence, the technique incorporates the measurement of the angular distribution of emitted charged species. These measurements can provide an assessment on such considerations as thrust cosine losses, spacecraft integration and exhaust contamination, operating conditions, and identification of ion emission regions.

2.1. APPARATUS

Figure 2.1 is a schematic diagram of the experimental setup used for the angle-resolved quadrupole mass spectrometric analysis [9, 24, 25]. The setup consists of three sections: rotating emission source, near-field targets, and far-field targets. The rotatable emission source is an internal flow capillary attached to a rotation stage allowing the angle of the spray to be varied with respect to the experimental axis. The source framework supports both an electrified extractor plate and the electrospray emitter. A 1.5-mm-diameter orifice in the extractor plate allows for the passage of the electrospray plume.

Near-field targets are mounted on a translating stage and consist of a Faraday cup, quartz crystal microbalance (QCM; model XTM/2 supplied by Inficon), and a cylindrical electrostatic lens element. These are 18 mm downstream from the emission source. The Faraday cup and QCM measure current and mass flow rate of the electrospray beam. Equal sized apertures with 0.8-mm-diameters are used on both targets. The aperture diameters, with a measurement interval of 2.5 deg, minimize oversampling. When the

cylindrical electrostatic lens element is moved into the electrospray beam path, the electrospray beam can continue onward to the far-field targets; a quadrupole mass filter with a set of focusing lenses at the entrance, a set of three grids used for the retarding potential analysis (RPA), and an off-axis channeltron detector. The channeltron detector is the signal collector for the mass spectrometric or RPA measurements in the far-field. The mass filter selects specific ion masses for the channeltron detector while the RPA establishes the ion kinetic energy. The RPA operates by determining the potential required to block the ions from reaching the channeltron detector.
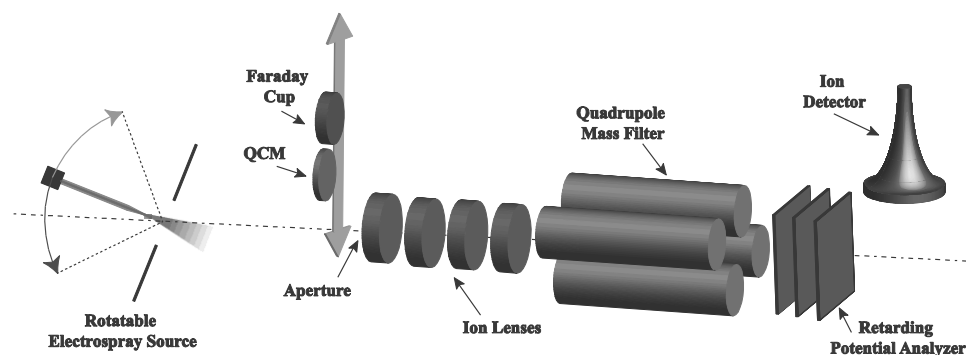
Figure 2.1. Experimental setup.

2.2. CHARGED EMISSION SOURCES

A capillary needle emitter is used for all experiments. The emitter and extractor geometry is shown schematically in Figure 1.1. The capillary needle has an internal flow of IL that is dependent on the backing pressure of the fluid feed system; depicted in Figure 2.2. The reservoir pressure, P_0, provides a backing pressure on the IL. This constant pressure is maintained by admitting an inert gas (in this case nitrogen) into the reservoir and pumping with a mechanical pump. The needle valve allows for direct control and setting of the reservoir pressure in small pressure increments. IL is fed by the fluid feed system from a reservoir, through a transport capillary, and out the tip of the

capillary needle emitter. The transport capillary is fused silica with a 100 µm inner diameter (ID) and an 82.5 cm length. The capillary needle is stainless steel with a tapered tip of 50 µm inner diameter and 3.5 cm length. Both capillaries are commercially available. This feed system is similar to the system used by Lozano[26], but the direct monitoring of the reservoir pressure using a pressure transducer eliminates the need to calculate the reservoir pressure based on the regulated source gas or pumping speed of the mechanical vacuum pump. When not in use, the ionic liquid reservoir remains under rough vacuum (<100 mTorr) to prevent water absorption.

2.3. FLOW RATE CALIBRATION

The reservoir pressure, P_0, is dependent on the nitrogen supply pressure, vacuum pumping speed, and length of gas transport lines of the setup. By expressing data as a function of the volumetric flow rate, the results are independent of the specific capillary fluid feed system. Experiments with other feed systems can therefore be directly compared with results presented here for equivalent flow rate, assuming that the same capillary tip inner diameter is used. To measure the flow rate, a bubble of nitrogen is introduced into the capillary and its velocity is measured using a visual magnifier giving a direct measure of the IL flow rate at various P_0 conditions. For the data collected, the velocity is measured in the transport capillary, external of the vacuum chamber.

Figure 2.3 shows the calibration results of two experimental sets of data collected at the two voltage conditions of 0 V and 2.2 kV. Both data sets have a linear trend and a maximum difference is less than 11%. The average values, with a standard deviation of less than 9%, are shown in Figure 2.3. Based on the trend and correlation between data points, the presence of the electric field does not appear to influence the IL volumetric flow rate as measured in the transport capillary. When the bubble results are compared to the mass flow rate based on QCM measurements, the QCM values are larger and represent a 25% systematic increase over the bubble method. The nominal capillary diameter is used to calculate the bubble method flow rate. The conclusion is that difference in the two flow rates is merely due to a manufacturing tolerance. This difference translates to a required 12% increase in capillary radius (i.e., actual radius of

28 μm, not 25 μm) to obtain the QCM flows. The QCM measurements are not used for calibration since full mass flow collection is not possible for all flow rate conditions.
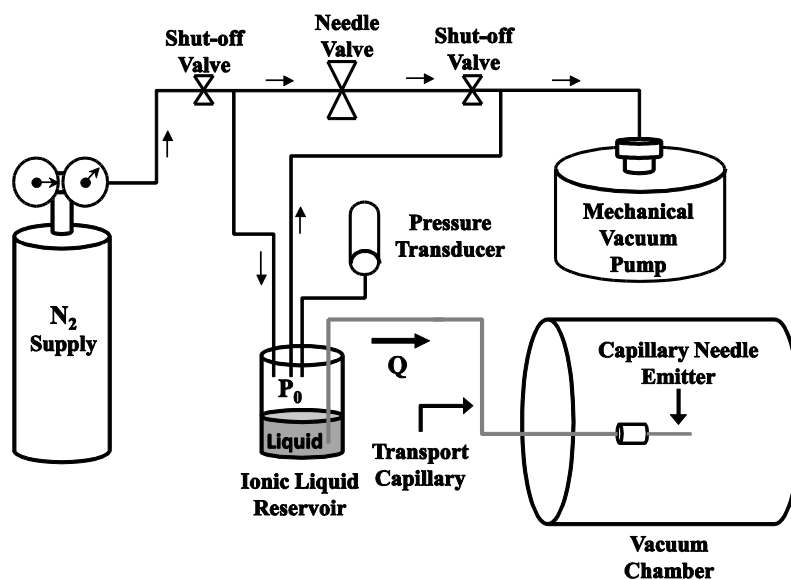
Figure 2.2. Capillary fluid feed system. Arrows indicate flow path of gas.
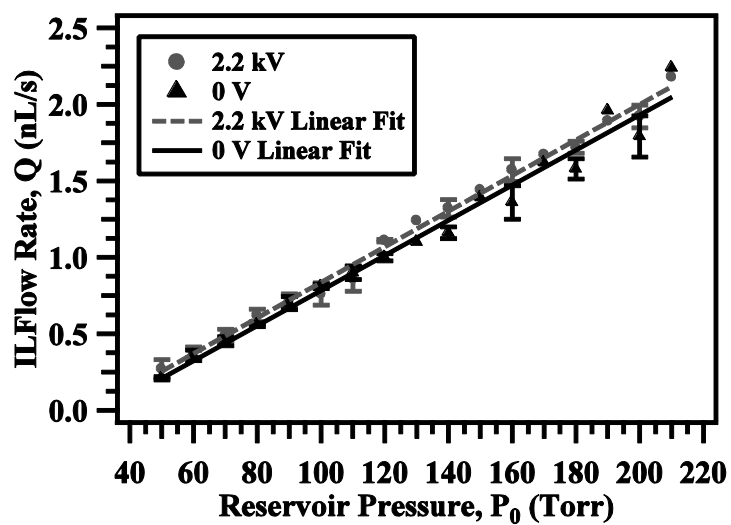
Figure 2.3. Comparison of IL flow rate vs. reservoir pressure, P_0.

3. PLUME ANALYSIS RESULTS

The plume analysis was conducted for a capillary emitter and extractor set with an extraction potential of 2.0 kV (V_N = +500 V, V_{Ext} = -1500 V). In this simple two electrode geometry, the theoretical acceleration, V_{acc}, is equivalent to the potential extraction potential (i.e., $V_{acc} = V_N - V_{Ext}$). However, ohmic losses occur within the jet structure of the Taylor cone reducing the potential of the emitted ions and leading to a reduced acceleration potential. This means the actual acceleration potential is $V_{acc} = V_N - V_{Ext} - V_\Omega$. When the acceleration potential is used to calculated thrust values in the remainder of this paper, V_{acc} will be 1793 V based on the retarding potential analysis results to be discussed. The 0.8-mm-diameter aperture before the near-field targets is set to ground. Given space limitations between the detectors and the rotatable source, angular measurements were possible only between ± 60 deg.

Figure 3.1 and Figure 3.2 illustrate the measured beam current as a function of flow rate, but with respect to two different sampling areas. The current density in Figure 3.1 is the angular measurement normalized to the detector aperture area. The maximum current density per flow rate is maintained at 0 deg (on-axis), but the current profiles broaden as the flow rate increases. At the highest flow rates, the current density profile approaches the acceptance angle limitation of the extractor aperture (~56 deg) resulting in the profile cutoff. The maximum measured current density of 2.09 nA·mm^{-2} is observed at 0 deg for a flow rate of 0.30 nL/s. With the shift in current to higher angles as flow rate increases, the current density at 0 deg drops to 1.15 nA·mm^{-2} for the maximum flow rate, 2.18 nL/s. The redistribution of current is best observed in the polar plot (Figure 3.2) of the angular current contribution. In this current plot, the sampling area varies as a ring of the integrated current hemisphere. Each ring has the circumference at the given angle on the hemisphere and a width of 0.85 mm, the sine component for a 2.5 deg step size between each measurement. The angular current contribution is a percentage normalized by the total integrated current for each flow rate. Unlike the current density profiles, the peak current does not occur at 0 deg for any of the flow rates studied. At 0.30 nL/s, the current percentage peaks at 17.5 deg and as flow rate increases the peak value shifts toward higher angles. The highest angle of current emission occurs at 35 deg.

The shifting maximum current percentage indicates that emission occurs less along 0 deg and more toward the perpendicular direction. Had the current been centered on 0 deg, then most of the emission would have been parallel to the electrospray beam axis.
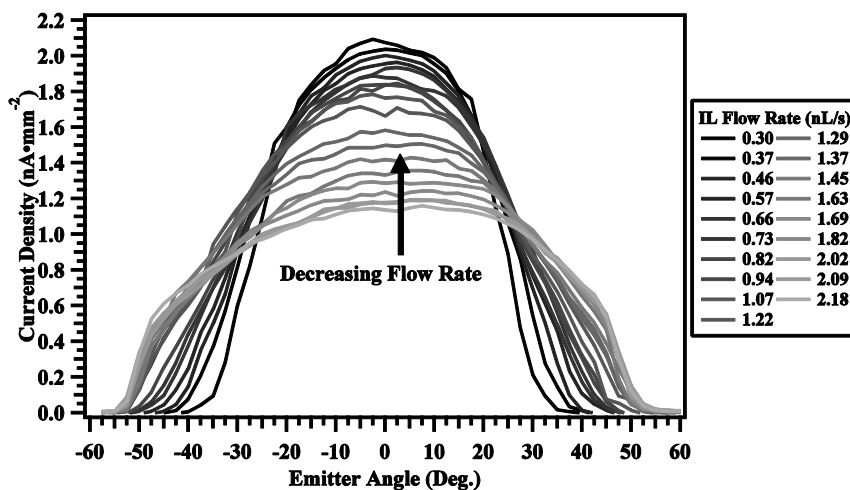
Figure 3.1. Capillary plume current density vs. emitter angle for discrete IL flow rates.
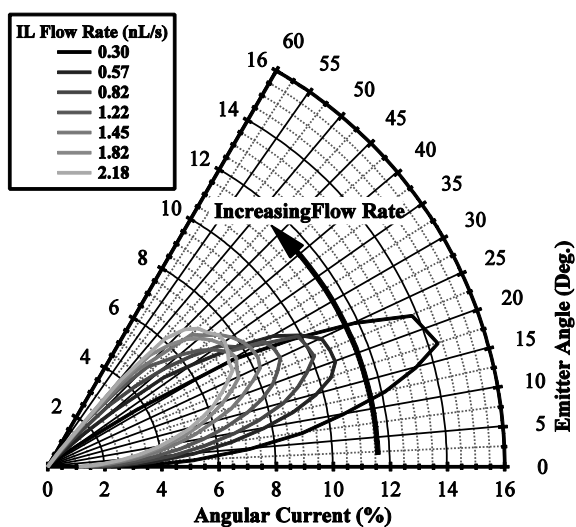
Figure 3.2. Select angular current contribution to integrated beam current.

Similar to the current density trends, the mass flow rate trends (Figure 3.3) indicate mass redistribution occurring as IL flow rate increases for the same angular measure and fixed aperture area. However, unlike current density, the centerline mass flow rate value continues to increase as the high angle values increases. The maximum mass flow at 0.30 nL/s is 2.35 ng·mm^{-2}·s^{-1}. The *m/q* of the capillary at 0.30 nL/s is 90,000 amu or equivalent to an IL cluster of $n = 439$, determined from the integration of the available QCM and Faraday cup data and assuming singly-charged particles. In contrast, the highest IL flow rate, 2.18 nL/s, generates a flow of 9.11 ng·mm^{-2}·s^{-1} and an *m/q* of 566,000 amu (i.e., $n = 2761$). This peak value of mass flow is nearly twelve times larger than the value associated with the more typical etched metal needle IL emitters. Typically for a metal needle, the peak mass flow rate is approximately 0.71 ng·mm^{-2}·s^{-1} to 1.06 ng·mm^{-2}·s^{-1} [9, 25]. Achieving higher mass flow rate as IL flow rate increases is not surprising, since by conservation of mass, the mass flow rate scales to the volumetric flow rate by the IL density.

Mass flow rate data points were collected at intervals of 5 deg and then interpolated for the angles in between for the IL flow rates illustrated in Figure 3.3. The 5 deg angle interval was used to prolong the accuracy of the QCM. Since [Bmim][DCA] has a low vapor pressure and does not vaporize under vacuum, any liquid collected on the surface of the QCM remains on the surface. At flow rates above 0.72 nL/s, the crystal frequency rapidly decreased from the nominal 6 MHz. This result was attributed to the high rate of deposition of IL mass on the crystal surface, which invalidated the thin film assumption. Cleaning the crystal of the IL deposit restored the QCM operation until the IL built up again. Consistent, repeatable results were only obtainable when the IL deposit layer was not significant and the crystal frequency remained higher than 5.9 MHz. This challenge had not been observed with externally wetted needle emitters with much lower mass flow rate [25, 27].

To verify that the Faraday cup fully captures the output of the capillary, the currents on the capillary tip and the extractor plate, hereafter referred to as the emitter current and extractor current, are obtained by measuring the potential across a 4.93 MΩ equivalent resistance on each associated voltage line and applying Ohm's law. This emitter current can be compared to the integrated results of the current density profiles in

Figure 3.1. The integrated beam current is calculated by integrating each current density profile over a hemisphere, similar to the Hall thruster beam current analysis of Manzella and Sankovic [28]. However, unlike their work where the ratio between detector distance to detector aperture size is ~20:1, the ratio for the current experiment is ~25:1.
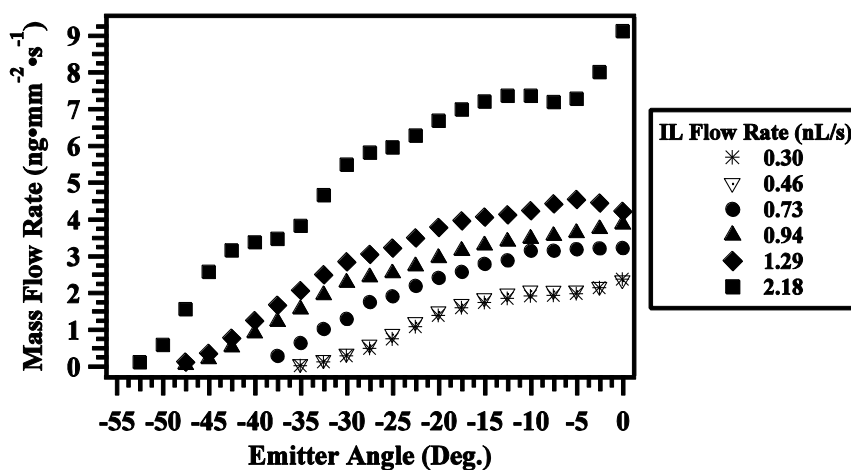
Figure 3.3. Mass flow rate vs. emitter angle for various IL flow rates.

With an IL capillary electrospray setup, a completed circuit can be achieved from both the electrospray tip and the IL reservoir. As a result, the IL reservoir must be insulated so that only the electrical circuit from the capillary tip exists. No emitter potential should be present when electrode potentials are applied on an IL filled capillary with no reservoir backing pressure. If a potential is detected, then a current path is present in the IL reservoir. The extractor plate is the closest point to the capillary tip for establishing an additional current path other than the Faraday cup. An increase in extractor current will correspondingly appear as a reduction in the integrated current when the circuit path is connected.

Figure 3.4 shows the emission current results of a 50 μm stainless steel tip over the same IL flow rate range as Figure 3.1. The emitter current is between 375 nA to 1200

nA. Full current recovery is achieved only by adding the results of the integrated current and extractor current together. This recovery indicates only the extractor is an additional current path and a significant source of current loss for IL flow rates over 0.90 nL/s. The integrated current over 0.90 nL/s accounts for 60 to 90% of the emitter current, but that percentage coincides with the mass flux accounted for by the QCM. The QCM measurement represents nearly 99% of the total mass supplied by the capillary indicating most of the charge is not carried by the bulk of the emitted mass. Instead the remaining 10 to 40% of the emission current is carried by low mass ions (discussed below) representing 0.5% of the total mass and is emitted outside the angle range measured. The detected charge distributed over the associated mass at a given flow rate results in an average *m/q* ranging from 90,000 (at 0.30 nL/s) to 566,000 amu (at 2.18 nL/s), assuming singly-charged species.
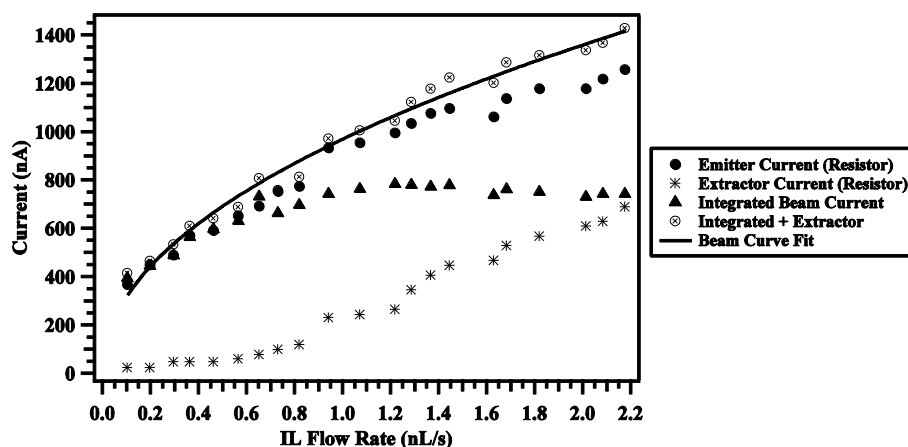
Figure 3.4. Emission current as a function of IL flow rate.

The far-field measurements are presented for the three selected volumetric flow rates of 0.27, 1.24, and 2.18 nL/s per the angular measurement, not integrated over the hemispherical area. The measured mass intensities (arbitrary units, arb.) are assembled into the mass spectra of Figure 3.5 and [Bmim][DCA] cations assigned to each set of

peaks. Table 3.1 lists the relevant cations and associated masses within the detection range of the mass filter. The angle-resolved mass spectra are presented at two different intensity scales in Figure 3.5 since at high volumetric flow rates the identifiable ions occur at a reduced intensity. To maintain comparability, the same voltage settings are used on the channeltron detector for all mass spectra and RPA data. This allows a relative comparison between the data sets of each flow rate. Kinetic energy profiles are presented in Figure 3.6-Figure 3.8 at centerline (i.e., on-axis) and at 17.5 deg (i.e., off-axis). In conducting the RPA scans, the four sampled masses, 344, 754, 800, and $m/q >$ 1000 amu are used to establish the kinetic energy profiles. The first two masses represent cations at the low and high end of the mass filter range. The 800 amu setting is used as a background measurement and is subtracted from the measurements of the cations. For $m/q > 1000$ amu, this is an all pass scan, which allows any mass greater than 1000 amu to pass through the mass filter and into the RPA grids. The all pass scan indicates the presence of larger masses not detected by the mass spectrometric measurements.

The mass spectra results (Figure 3.5) show that all cation species in the quadrupole mass range (Bmim([Bmim][DCA])$_n{}^+$ for n = 0, 1, 2, 3, 4) are present; though under increasing flow rate conditions the intensity of these species decreases. No evidence of multiply charged species or fragmentation of parent cation was observed in the mass spectra. Cation species less than 500 amu only occur in trace amounts (i.e., < 10% of total intensity) at higher flow rates. Mass intensity of each detected species becomes uniform across the angle measurement range as flow rate increases. In addition to the mass spectra, the mass intensity per ion emission product has been integrated establishing a percent contribution of each emission product, excluding $m/q > 1000$ amu. Table 3.2 lists the percent contribution of the measured intensity of each ion species over flow rate and angle. The dominant species for 0.27 nL/s is (Bmim([Bmim][DCA]) $^+$ which contributed 56.5% of the measured intensity. As IL flow rate increases, the dominant species transitions to (Bmim([Bmim][DCA])$_4{}^+$ contributing 40.7% of the measured intensity at 2.18 nL/s. Note that the percentages are for the measured intensities within the range of 0-1000 amu. These percentages do not account for the droplet proportion of the beam since such large masses cannot be measured by the mass spectrometer.
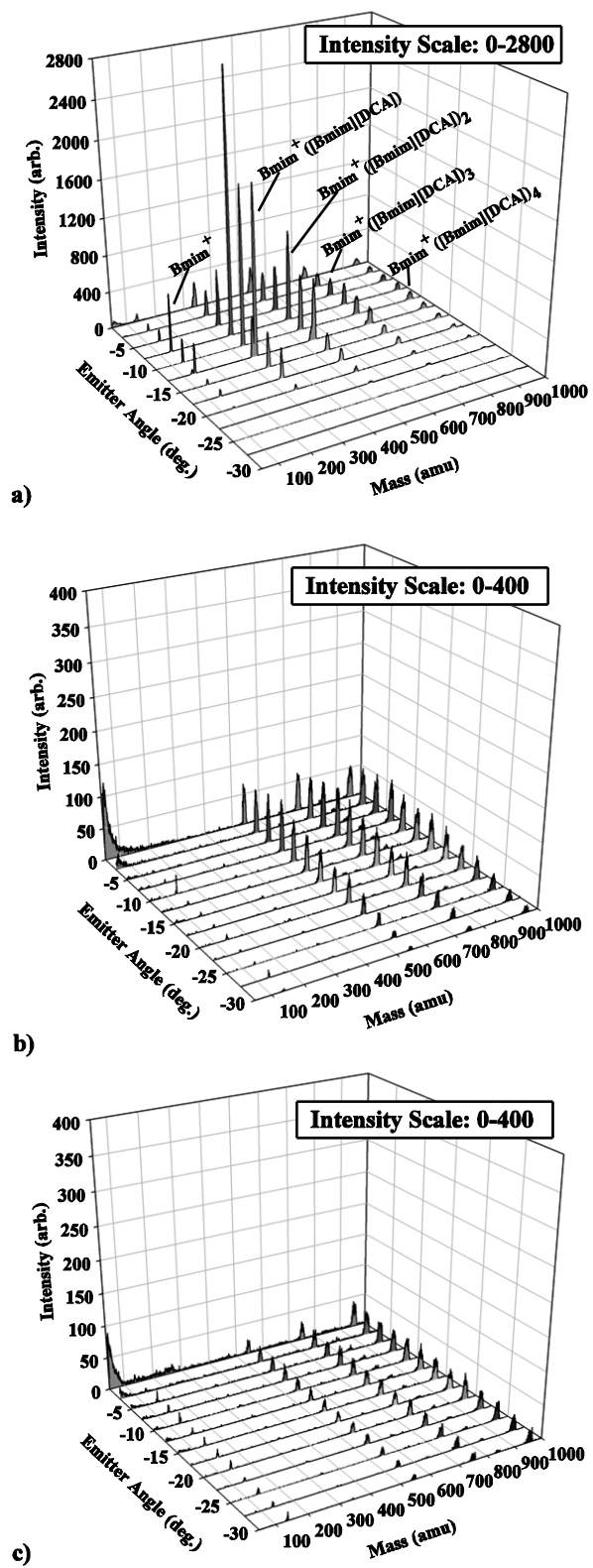
Figure 3.5. Angle-resolved cation mass spectra at flow rates a) 0.27 nL/s, b) 1.24 nL/s, c) 2.18 nL/s.

Table 3.1. [Bmim][DCA] cation species and associated masses for < 1000 amu.

n Value	Cation	Mass, amu
0	Bmim$^+$	139
1	Bmim([Bmim][DCA])$^+$	344
2	Bmim([Bmim][DCA])$_2{}^+$	549
3	Bmim([Bmim][DCA])$_3{}^+$	754
4	Bmim([Bmim][DCA])$_4{}^+$	959

Table 3.2. Species percentage contribution to measured intensity.

Flow Rate, nL/s	Angle Range, deg	Percentage of Contribution to Measured Intensity				
		$n = 0$	$n = 1$	$n = 2$	$n = 3$	$n = 4$
0.27	0 to -30	10.9	56.5	21.6	7.4	3.7
0.49		1.5	2.4	42.6	32.6	20.9
0.72		2.0	1.3	38.2	35.6	22.9
1.24		6.1	1.4	33.5	35.3	23.8
2.18		11.2	1.8	18.0	28.3	40.7
0.27	-20 to -30	0.2	0.3	0.6	0.9	0.6
0.49		0.6	0.1	6.3	6.4	3.5
0.72		1.2	0.4	8.8	9.1	6.7
1.24		2.5	0.3	9.1	12.8	7.3
2.18		5.8	0.8	7.2	14.1	20.3

Figure 3.6-Figure 3.8 show the energy distribution measured by the RPA at two different angles (0 and 17.5 deg). The maximum value of the distributions indicates the most probable kinetic energy of each ion species and is identified by a vertical line. The distribution trends for each cation species (344, 754, and m/q >1000 amu) are similar between changes in flow rate and angle. However, the measured peak value increases with angle and decreases with pressure. At 0.27 nL/s, a 80 (754 amu) and 50 eV (m/q > 1000 amu) increase in peak energy occurs between the on- and off-axis cases. At 1.24 and 2.18 nL/s, a 70 and 40eV increase occurs between the on- and off-axis cases of the

754 and $m/q > 1000$ amu emission products, respectively. The maximum energies of each distribution are less than 400 eV and well under the 500 eV emitter potential suggesting that the ions are born at a lower potential than the capillary. The effect increases with flow rate, but is less effectual at larger angles. Identifying the source of loss will be an important step in maximizing ion kinetic energy. Surprisingly, the data at all three flow rates indicate a significant presence of mass over 1000 amu within the electrospray beam even at high angles. The $m/q > 1000$ amu kinetic energy distribution accounts for the high mass flow rate measurements at high angles even though the mass spectra show minimal mass below 1000 amu at those angles.
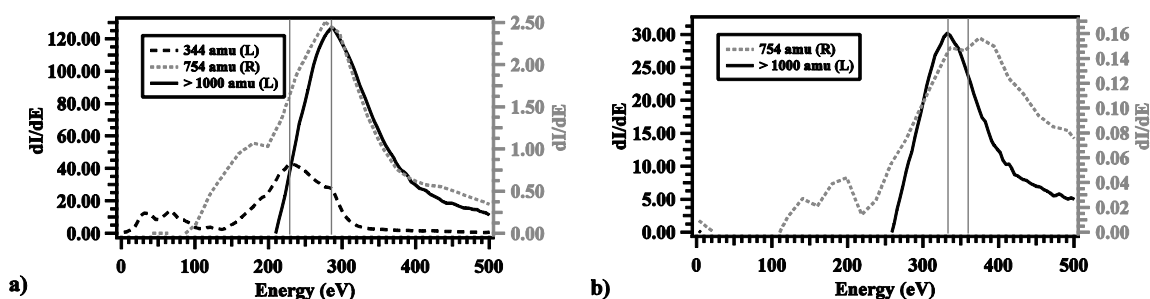
Figure 3.6. RPA of plume at 0.27 nL/s a) 0 deg, b) 17.5 deg for 344 amu (left axis), 754 amu (right axis), and $m/q > 1000$ amu (left axis).
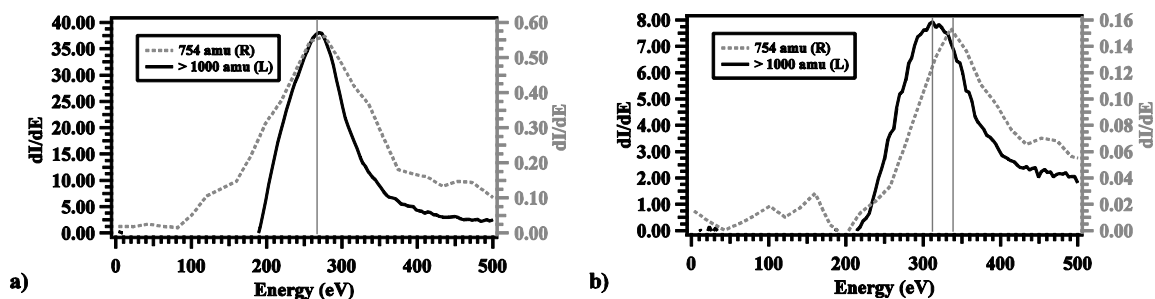
Figure 3.7. RPA of plume at 1.24 nL/s a) 0 deg, b) 17.5 deg for 754 amu, and $m/q > 1000$ amu.
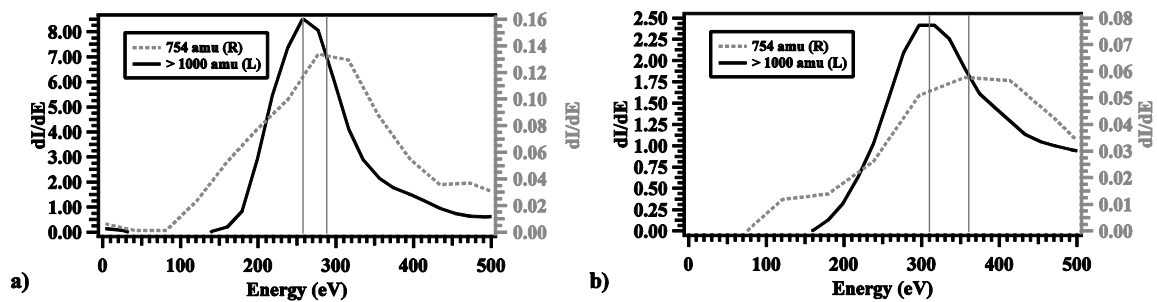
Figure 3.8. RPA of plume at a IL flow rate of 2.18 nL/s a) 0 deg, b) 17.5 deg for 754 amu, and *m/q* > 1000 amu.

4. DISCUSSION

The electrospray cone-jet characteristics do not remain static when the IL flow rate is altered. Instead, the charge distribution, mass distribution, and kinetic energy of the beam modify with the flow rate change. Taken together, these microscopic quantities are the basis for the propulsive performance of the capillary emitter. In the following sections, these electrospray dependencies are discussed based on the exhibited trends in the current density, mass flow rate, mass spectra, and RPA data. When thrust and I_{sp} are calculated using the near-field results, electrospray performance of a single emitter is established and can be connected to the beam characteristics and composition at specific IL flow rates.

4.1. PLUME PROPERTIES

4.1.1. Beam Profile Changes.
The electrospray beam profile significantly changes over the range of IL flow rates sampled. The current profiles in Figure 3.1 and Figure 3.2 indicate a redistribution of charge with changing flow rate. Increasing flow pushes charged species to larger angles until they extend beyond the limit of the measurement range at 56 deg due to acceptance angle of the extractor aperture. The mass flow rates shown in Figure 3.3 corroborate this broadening. No mass is observed at 37.5 deg from center for the lowest flow rate while nearly 38% (i.e., 3.46 ng·mm^{-2}·s^{-1}) of the peak value, 9.11 ng·mm^{-2}·s^{-1}, is observed at the same angle for the highest flow rate examined. The three mass spectra in Figure 3.5 mirror this observed behavior. At the lowest flow rates (Figure 3.5a), ionic species ($n < 4$) are only detected within roughly 20 deg from the center while at larger flow rates ionic species $n = 2$ to 4 are present in the spectra beyond 20 deg. Table 3.2 indicates percent contribution of the measured intensity of each ion species for each IL flow rate over the angle range -20 to -30 deg. For that range, the data indicate a 3 to 20% increase in $n = 2$ to 4 species as flow rate changes. At 2.18 nL/s, the measured spectrum (Figure 3.5c) appears as a nearly flat distribution peaked along the centerline. The data in Table 3.2 correlate with this flat distribution as 20% of the measured intensity is contributed to both the 0 to -20 deg and the -20 to -30 deg angle ranges.

In addition to the increasing divergence as flow rate increases, the compositional makeup of the electrospray plume is significantly affected by the change of flow rate. At the lowest flow rate studied, $n = 1$ species accounts for 56.5% of the measured intensity at this low flow rate. As the flow rate is increased to 2.18 nL/s, the $n = 4$ species accounts for 40.7% of the measured intensity. Further, the intensities of species in the detection range have decreased by roughly a factor of 50 over those intensities observed at the lowest flow rate. The transition in dominant species and the decrease in intensity suggest that the beam composition has transitioned to larger charged masses and that greater contribution result from species of $m/q > 1000$ amu to account for the higher mass flow rates detected by the QCM. The transition in emission product is corroborated by the change in jet diameter. Fernández de la Mora and Loscertales [29] established that the jet diameter scales as a function of IL flow rate. When evaluated at 0.27 nL/s and 2.18 nL/s, the jet diameters are approximately 15 nm and 31 nm, respectively. These diameters are determined using the droplet to jet diameter ratio of 1.89 as established by Cloupeau and Prunet-Foch [22] and the droplet diameter equation specified by Gañán-Calvo et al. [30]. The increasing jet diameters suggest that larger droplets are produced changing the beam composition as flow rate increases. It should be noted that the stated jet diameters result in jet velocities far greater than 500 eV which do not appear in the kinetic energy profiles of the RPA. Jet diameters four times these values are necessary to achieve correspondence with the energy profiles. It appears that this experiment does not follow the accepted ratio of 1.89.

4.1.2. Reduced Ion Energies and Origin Points. The RPA data shown in Figure 3.6 - Figure 3.8 indicate, for any studied flow rate, that all ions emitted from the capillary are at kinetic energy levels well below the emitter bias potential. In the experiment, emitters are biased to 500 V to maintain ion transmission through the apparatus and to minimize the ion energy in the mass filter [25]. If the energy distribution of a charged species peaks at 500 eV, then it can be concluded that the species originated near theemitter. Otherwise, any substantial energy drop is indicative of ohmic losses. These losses occur as a result of the resistivity of the IL. As current flows through the jet which has a large length to cross sectional area ratio (i.e., on the order of 0.3 nm^{-1}), Ohm's law takes effect and the potential is reduced in accordance to the resistance of the jet. The

cone does not experience such ohmic losses due to the much smaller length to cross section ratio (i.e., less than 0.01 nm^{-1}). The width of the energy distribution is indicative of the variation in kinetic energies of the emitted species. The regions of lower kinetic energy in angular RPA measurements have provided a means to identify the origins of ion emission products as seen in Figure 1.1. Since the IL jet structure only suffers from ohmic losses, then the emission products must be originating from the jet. The neck emission zone is close to the emitter where near zero ohmic losses occur in the cone and thus ion emission products are near 500 eV. These observations have been restricted to IL emission from either etched metal needles or small capillaries with tip diameters less than 20 μm [5, 7, 25, 31].

Figure 3.6b illustrates the kinetic energy distributions of the ion emission products at an angle 17.5 deg from center. The energy trends, except the 344 amu case, peak around 350 eV. For increasing IL flow rates, the kinetic energies of these species are reduced further to approximately 330 eV in the case of 1.24 and 2.18 nL/s of Figure 3.7b and Figure 3.8b. The on-axis plots (Figure 3.6a, Figure 3.7a, and Figure 3.8a) show that the emission products of 754 and $m/q > 1000$ amu undergo further reduction in kinetic energy. The peak energies are lower in this narrow region of the spray and are centered at approximately 270 to 290 eV. Based on the kinetic energy profiles, the large masses associated with $m/q > 1000$ amu scans are the resulting products from the jet breakup. In Figure 3.6a, the 344 amu energy profile is centered near the lower end of the $m/q > 1000$ amu profile at approximately 230 eV. The profile suggests that the 344 amu species are predominately emitted from other sources, not from the jet breakup. If the 344 amu ions had originated from the same locations as the larger mass emission products (e.g. the jet tip breakup) then the 344 amu energy distribution would be wider and centered on ~290 eV. The most likely source of the 344 amu emission products is field evaporation from the larger masses emitted from the jet breakup. When the 344 amu products are emitted, the large masses have moved away from the jet and are at a lower potential. As a result, the 344 amu ions are at energies less than the parent large charged masses. The 754 amu profile shows this wider profile better than the 344 amu distribution. The 754 amu energy profile matches the large mass energies and suggests similar emission locations as these large masses. The 754 amu distribution does extend toward 100 eV as well. This

extension suggests some of the 754 amu emission products are likely the result of field evaporation from larger charged masses as well.

The origins of the ion emission products conform to the typical emission zones of a cone-jet structure seen in Figure 1.1, but with two caveats. First, the detected ion emission products are the result of a jet with a wide emission spray angle. Secondly, emission products from the neck are not reaching the detector. Instead the neck emission products are establishing a second current path to the extractor. A wide spraying jet is required to account for large mass species at high angles. Further investigation is needed to explain the mechanism behind the wide spray. The wide variation in the energy profiles of the RPA data would be the result of ion evaporation from the large masses (i.e., droplets) at points away from the jet structure. Emission products from the neck can be distinguished from the jet emission due to the exhibited kinetic energies of the ions and the ion masses associated with those energies. Neck emission tends to be low mass ions, species $n = 0$ to 2 as a result of field evaporation and these ions have peak kinetic energies of ~500 eV [3, 4, 7]. As a result, the neck emission products tend to be sources of charge, not mass. Based on the RPA results, these high energy, low mass ions are not present at any measured angle.

The near-field results listed in Table 4.1 for select IL flow rates justify the conclusion of where the emission products are originating. The integrated mass flow rate and current near-field data are proportionally different. The integrated mass flow from the jet emission approaches the nominal mass flow rate calculated from IL density (1.063 g/cm^3) and volumetric flow rate. By conservation of mass, the mass transmitted by the capillary must be emitted from the tip. The emitter current provides a measure of current flow within the circuit before ion emission from the cone-jet. If a substantial difference is observed between the integrated and emitter currents, then the current flow is being diverted into another circuit path instead of the path to the Faraday cup. The integrated current consistently represents 60 to 90% of the emitter current for IL flow rates over 0.90 nL/s (Figure 3.2) and subsequently, 10 to 40% of the current is recovered by the extractor. Assuming the emission products of the neck are low mass ions, the percentage of mass flux due to the extractor current can be determined. If any of the species of $n = 0$ to 2 are assigned the extractor current, then the extractor mass flux represents less than

0.5% of the total mass flow rate detected. This means that near-field results represent near full mass flow rate collection but only partial charge collection for IL flow rates greater than 0.90 nL/s. Emitted current from the neck is being leaked to the extractor given the proximity to the capillary tip. Simion 8.1 software was used to model a cone-jet structure in a simple electrode configuration with a separation of 2 mm and singly-charged ions emitted from the neck region. Simulation results showed, independent of ion mass, that ions from the neck did not reach the Faraday cup for detection and either impacted the extractor or passed through the extractor aperture at an angle greater than 35 deg.

4.2. PREDICTED PROPULSION PERFORMANCE

4.2.1. Beam Current and Mass Flow Rate. From the current data in Figure 3.2, the empirical current scaling law $I(Q)_{Beam}$ can be determined by curve fitting to the data. This scaling law allows extrapolation of the emission output to flow rates not studied to be used in establishing potential propulsion performance at those flow rates. Electrospray scaling laws have been developed by Fernández de la Mora and Loscertales [29] [see Eq. (1)], and Gañán-Calvo et al. [30]. Those scaling laws were power functions with the constraint of zero current at zero flow rate. Equation (2) was derived by the same method using the combined measurements of the integrated current and extractor current and with the same constraint of zero current at zero flow rate as in references [29] and [30]. The scaling law $I(Q)_{Beam}$ relates the current, in nanoampere, and IL flow rate, in nL/s. Equation (2) is consistent with Eq. (1) developed by Fernández de la Mora and Loscertales. The curve fit established an equivalent power of 0.5. The scale factor of 986 can be broken down into values of $f(\varepsilon)$ and the IL physical properties (see Table 1.1). As a result, $f(\varepsilon)$ equates to 4.6 if the dielectric is assumed to be 11.3 [13]. This functional value is consistent with the results Fernández de la Mora and Loscertales established for dielectric constant for pure solvents. The $f(\varepsilon)$ profile shows that when $\varepsilon =10$, $f(\varepsilon) = 4$ [29].

In addition, a linear fit [Eq. (3)] was applied to the integrated mass flow rate since the measurement exceeded the nominal rates based on IL density and volumetric rate. The minimum current can be calculated using the minimum IL flow rate in Eq. (4) as

determined by Fernandez de la Mora and Loscertales [32] and evaluated in Eq. (2). At the minimum IL flow rate of 4.35 picoliters per second (pL/s), which is much less than the range studied, the minimum current value is 65 nA. The minimum IL flow rate is larger than the required rate of 0.09 pL/s needed to overcome the hydraulic resistance of the capillaries. For this investigation, the minimum IL flow is only used to define a theoretical lower limit of the scaling law.

$$I(Q) = f(\varepsilon) \cdot \left[\frac{\gamma K Q}{\varepsilon} \right]^{0.5} \tag{1}$$

$$I(Q)_{Beam} = 986 \cdot Q^{0.5} \tag{2}$$

$$\dot{m} = 1770 \cdot Q \tag{3}$$

$$Q_{min} = \frac{\gamma \varepsilon \varepsilon_0}{\rho K} \tag{4}$$

The emitted current and mass flow rate are required quantities needed to calculate the mass-to-charge ratio, m/q, output at each IL flow rate. Table 4.1 lists the various values of current, mass flow rate, and m/q output. The current data indicate a 10 to 41% loss in the integrated current measurement at mid to high IL flow rates, but is recovered as a current on the extractor electrode. The current loss is translated to the m/q value calculated using the integrated current and mass flow rate data. The integrated mass-to-charge ratio is 1.5 times higher than the mass-to-charge ratio determined from the results of the current fit in Eq. (2) and mass flow rate fit in Eq. (3) referred to as $I(Q)_{Beam}$ in Table 4.1.

4.2.2. Determination of Thrust and I_{sp}. The propulsion performance of a single emitter is predicted using the collected current density and mass flow rate data. Six ILflow rates (see Table 4.2) were selected to study the performance of the emitter output under variable IL flow rate conditions. These IL flow rates were selected based on the available mass flow rate data collected. Calculations of thrust, I_{sp}, and power required were determined using Eqs. (5-7). Only the total thrust of the electrospray beam, not the thrust provided by each ion species, could be determined. Since the percentage of droplet

contribution could not be determined, it would have been inappropriate to use the percentages reported in Table 3.2 as the droplet contribution would have been completely neglected. For the calculation of thrust [Eq. (5)], the acceleration potential, V_{acc}, is required, but this value actually depends on the ohmic losses occurring within the electrospray beam as IL flow rate changes. For simplification, a standard value of 1793 V is used in all the following calculations. The ohmic loss value used to determine V_{acc} is established by averaging the losses of the peak kinetic energies for both the on and off-axis in the RPA results of $m/q > 1000$ amu.

Table 4.1. Current, mass flow rate ($\dot{m}$), and mass-to-charge ratio (m/q) data at select IL flow rates.

Flow Rate, nL/s	Integ. Current, nA	Emitter Current, nA	Current Diff., %	Ext. Current, nA	Integ. $\dot{m}$, ng/s	Nom. $\dot{m}$, ng/s	Integ. m/q, amu	$I(Q)_{Beam}$ m/q, amu
0.30	486	487	0.2	45	454	317	90,000	95,000
0.46	594	589	0.8	45	503	493	82,000	117,000
0.73	660	751	12.1	95	885	779	129,000	148,000
0.82	694	772	10.1	116	-	874	-	157,000
0.94	740	931	20.5	227	1590	1003	207,000	168,000
1.29	778	1032	24.6	342	2046	1369	254,000	197,000
1.45	777	1094	29.0	443	-	1539	-	209,000
1.82	749	1176	36.3	565	-	1937	-	234,000
2.18	740	1255	41.0	686	4335	2315	566,000	256,000

Table 4.2 lists the propulsion performance of the [Bmim][DCA] capillary emitter at the six selected flow rates. The full thrust value uses the integrated beam current and mass flow rate values in Table 4.1 with no correction for cosine losses. The axial thrust value takes into account cosine losses and is a true representation of the thrust contribution from the emitted products detected by the near-field sensors. Within the detection range of ±60 deg, the cosine loss is less than 13% for up to a flow of 2.18 nL/s. The specific charge, q/m, used to determine these two sets of thrust values are also listed

in Table 4.2 for comparison. At 0.30 nL/s, the axial thrust output is 0.84 μN with an I_{sp} of 200 s. Increasing IL flow rate to 2.18 nL/s increases thrust output to 2.90 μN with an I_{sp} of 80 s. The increasing of IL flow rate results in nearly doubling the thrust output of the single emitter. The impact of charged droplet contributions can be seen in the I_{sp} value. The large mass contributions of the droplets have reduced the I_{sp} of the emitter to nearly 100 s.

Better performance would be achieved above 0.90 nL/s with a minimized extractor current path. To that end, an empirical set of thrust and I_{sp} data have been determined and are presented as well. Unlike the data in Table 4.2, the empirical results derived from Eqs. (2) and (3) do not account for cosine losses and only reflect a theoretical full thrust output. The empirical performance predictions of a single emitter are shown in Figure 4.1 for a IL flow rate of 4.35 pL/s up to 2.5 nL/s. The results of Table 4.2 reflect zero contribution from the extractor current and indicate that the emission products from the jet structure drive the performance of the electrospray emitter at the investigated flow rate range. However, the undetected emission at high angle does affect the performance and operational efficiency of the electrospray emitter. For the electrode configuration operated at below 0.9 nL/s, the results of Table 4.2 and of Figure 4.1 provides the clear propulsion performance of an [Bmim][DCA] electrospray emitter. The maximum thrust achievable is approximately 1.83 μN with an I_{sp} of 132 s with a beam divergence limited to less than ±50 deg based on near-field data. Operating the electrospray emitter above 0.90 nL/s will result in limited thrust gains and IL contamination of the extractor.

$$F = \dot{m}v = \dot{m}\sqrt{\frac{2V_{acc}q}{m}} = \sqrt{2V_{acc}\dot{m}I} \qquad (5)$$

$$I_{sp} = \frac{F}{\dot{m}g} \qquad (6)$$

$$P_e = IV_{acc} \qquad (7)$$

Table 4.2. Predicted propulsion performance of a single electrospray emitter operating on [Bmim][DCA] at select IL flow rates.

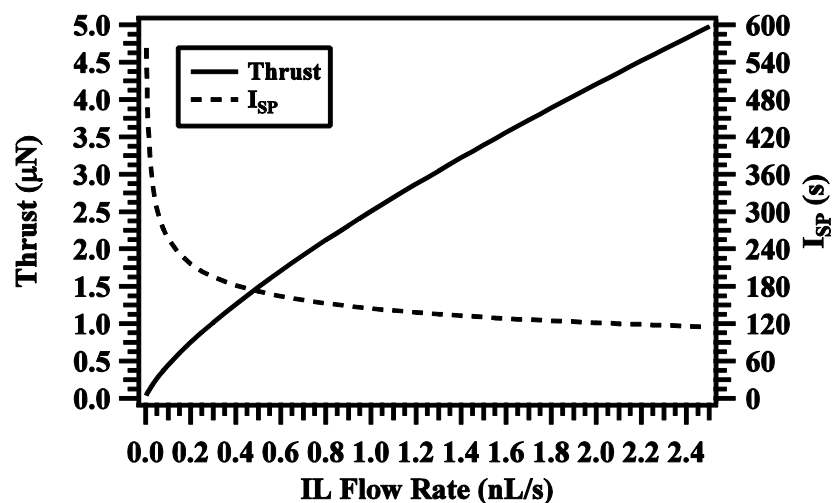| IL Flow Rate, nL/s	Full q/m, C/kg	Full Thrust, μN	Axial q/m, C/kg	Axial Thrust, μN	Cosine Thrust Loss, %	I_{sp}, s	Emission Power, mW
0.30	1071	0.89	1059	0.84	5.7	200	0.87
0.46	1180	1.03	1146	0.96	6.8	210	1.06
0.73	745	1.45	726	1.32	8.8	167	1.18
0.94	465	2.05	458	1.83	11.2	132	1.33
1.29	380	2.39	370	2.10	12.0	119	1.39
2.18	171	3.39	167	2.90	13.0	80	1.33

Figure 4.1. Predicted propulsion performance of a single electrospray emitter based on empirical current scaling law of Figure 3.2.

5. CONCLUSION

From the [Bmim][DCA] results, there will be trade-offs in electrospray performance when the IL flow rate is adjusted to vary propulsive output. Based on the mass spectra collected, the electrospray beam is composed of a mix of ions (Bmim([Bmim][DCA])$_n^+$; $n = 0$ to 4) and charged droplets for the IL flow rate range studied. When the IL flow rate is increased, the droplet contribution begins to dominate the beam composition. This droplet domination leads to increased thrust, but with a penalty in efficient use of the IL propellant (i.e., decreased I_{sp}). For the [Bmim][DCA] 50 μm ID emitter as configured, angled-resolved near-field measurements indicate the IL flow rate should be limited to a maximum of 0.90 nL/s to maximize the specific charge and to avoid establishing a extractor path. At these low flow rates, the beam divergence remains under ±50 deg. In reducing the flow rate, the electrospray beam composition will shift toward pure ionic contributions and increased q/m ratios will be established at low angle. Operating above 0.90 nL/s will result in the acceleration of 99% of the emitted IL mass, but only a proportion of the total charge input will contribute due to the presence of the extractor current. At 0.90 nL/s, the thrust and I_{sp} are 1.83 μN and 132 s, respectively. Increasing IL flow rate to 2.18 nL/s only achieves an additional 1.07 μN of thrust at 80 s I_{sp}.

The data suggest minimizing current loss to the extractor from neck of the Taylor cone and ohmic losses along the jet structure. Current loss impacts the calculated propulsion output of the emitter and such values do not truly reflect the performance of the emitter. Adjustment to the experimental setup, such as reducing electrode spacing and increasing the diameter of the extractor aperture, should ensure reduced current loss and allow additional emission product reaches the detectors. Ohmic losses are inherent to electrospray systems due to the size of the jet structure and properties of the electrospray propellant. Minimizing ohmic losses ensures energetic emission products and can only be achieved by controlling the size of the jet. Overall the data showed that IL flow rate can be adjusted to change performance just as well as the beam current through voltage variation. Flow rate adjustment does not require a robust electrical system to handle higher voltages (3-20 kV).

REFERENCES

[1] Taylor, G. I., "Disintegration of Water Drops in an Electric Field," *Proceedings of the Royal Society of London. Series A, Mathematical and Physical Sciences*, Vol. 280, No. 1382, 1964, pp. 383-397.

[2] Iribarne, J. V. and Thomson, B. A., "On the Evaporation of Small Ions from Charged Droplets," *The Journal of Chemical Physics*, Vol. 64, No. 6, 1976, pp. 2287-2294.

[3] Gamero-Castaño, M. and Fernandez de la Mora, J., "Direct Measurement of Ion Evaporation Kinetics from Electrified Liquid Surfaces," *Journal of Chemical Physics*, Vol. 113, No. 2, 2000, pp. 815-832.

[4] Gamero-Castaño, M., "Electric-Field-Induced Ion Evaporation from Dielectric Liquid," *Physical Review Letters*, Vol. 89, No. 14, 2002, pp. 147602.

[5] Chiu, Y., Gaeta, G., Heine, T. R., Dressler, R. A. and Lavandier, D. J., "Analysis of the Electrospray Plume from the EMI-Im Propellant Externally Wetted on a Tungsten Needle," *42nd AIAA/ASME/SAE/ASEE Joint Propulsion Conference & Exhibit*, Sacramento, CA, AIAA Paper 2006-5010, 2006.

[6] Romero-Sanz, I., Bocanegra, R., Fernandez de la Mora, J. and Gamero-Castaño, M., "Source of Heavy Molecular Ions Based on Taylor Cones of Ionic Liquids Operating in the Pure Ion Evaporation Regime," *Journal of Applied Physics*, Vol. 94, No. 5, 2003, pp. 3599-3605.

[7] Chiu, Y. and Dressler, R. A., "Ionic Liquids for Space Propulsion," *Ionic Liquids IV: Not Just Solvents Anymore*, American Chemical Society, Washington DC, 2007, pp. 138-161.

[8] Schreiner, C., Zugmann, S., Hartl, R. and Gores, H. J., "Fractional Walden Rule for Ionic Liquids: Examples from Recent Measurements and a Critique of the So-Called Ideal KCl Line for the Walden Plot," *Journal of Chemical & Engineering Data*, Vol. 55, No. 5, 2009, pp. 1784-1788.

[9] Miller, S. W., Prince, B. D. and Rovey, J. L., "Capillary Extraction of the Ionic Liquid [Bmim][DCA] for Variable Flow Rate Operations," *48th AIAA/ASME/SAE/ASEE Joint Propulsion Conference & Exhibit*, Atlantia, GA, AIAA Paper 2012-3738, 2012.

[10] Zech, O., Stoppa, A., Buchner, R. and Kunz, W., "The Conductivity of Imidazolium-Based Ionic Liquids from (248 to 468) K. B.Variation of the Anion," *Journal of Chemical and Engineering Data*, Vol. 55, No. 5, 2010, pp. 1774-1778.

[11] Carvalho, P. J., Regueira, T., Santos, L. M. N. B. F. and Coutinho, J. A. P., "Effect of Water on the Viscosities and Densities of 1-Butyl-3-methylimidazolium Dicyanamide and 1-Butyl-3-methylimidazolium Tricyanomethane at Atmospheric Pressure," *Journal of Chemical and Engineering Data*, Vol. 55, No. 2, 2010, pp. 645-652.

[12] Sánchez, L. G., Espel, J. R., Onink, F., Meindersma, G. W. and de Haan, A. B., "Density, Viscosity, and Surface Tension of Synthesis Grade Imidazolium, Pyridinium, and Pyrrolidinium Based Room Temperature Ionic Liquids," *Journal of Chemical and Engineering Data*, Vol. 54, No. 10, 2009, pp. 2803-2812.

[13] Stoppa, A., Hunger, J., Buchner, R., Hefter, G., Thoman, A. and Helm, H., "Interactions and Dynamics in Ionic Liquids," *The Journal of Physical Chemistry B*, Vol. 112, No. 16, 2008, pp. 4854-4858.

[14] Wandschneider, A., Lehmann, J. K. and Heintz, A., "Surface Tension and Density of Pure Ionic Liquids and Some Binary Mixtures with 1-Propanol and 1-Butanol," *Journal of Chemical & Engineering Data*, Vol. 53, No. 2, 2008, pp. 596-599.

[15] Weingärtner, H., "The Static Dielectric Constant of Ionic Liquids," *Zeitschrift für Physikalische Chemie*, Vol. 220, No. 10, 2006, pp. 1395-1405.

[16] Berg, S. P., "Design and Development of Ionic Liquid Dual-Mode Spacecraft Propellants," Masters Thesis, Mechanical and Aerospace Engineering Dept., Missouri University of Science & Technology, Rolla, MO, 2012.

[17] Schneider, S., Hawkins, T., Rosander, M., Vaghjiani, G., Chambreau, S. and Drake, G., "Ionic Liquids as Hypergolic Fuels," *Energy & Fuels*, Vol. 22, No. 4, 2008, pp. 2871-2872.

[18] Berg, S. P. and Rovey, J. L., "Dual-Mode Propellant Properties and Performance Analysis of Energetic Ionic Liquids," *50th Aerospace Sciences Meeting*, Nashville, TN, AIAA Paper 2012-0975, 2012.

[19] Berg, S. P. and Rovey, J. L., "Assessment of Imidazole-Based Ionic Liquids as Dual-Mode Spacecraft Propellants," *Journal of Propulsion and Power*, Vol. 29, No. 2, 2013, pp. 339-351.

[20] Donius, B. R. and Rovey, J. L., "Ionic Liquid Dual-Mode Spacecraft Propulsion Assessment," *Journal of Spacecraft and Rocket*, Vol. 48, No. 1, 2011, pp. 110-123.

[21] Donius, B. R. and Rovey, J. L., "Analysis and Prediction of Dual-Mode Chemical and Electric Ionic Liquid Propulsion Preformance," *48th Aerospace Sciences Meeting*, Orlando, FL, AIAA Paper 2010-1328, 2010.

[22] Cloupeau, M. and Prunet-Foch, B., "Electrostatic Spraying of Liquids in Cone-Jet Mode," *Journal of Electrostatics*, Vol. 22, No. 2, 1989, pp. 135-159.

[23] Gamero-Castaño, M. and Hruby, V., "Electrospray as a Source of Nanoparticles for Efficient Colloid Thrusters," *Journal of Propulsion and Power*, Vol. 17, No. 5, 2001, pp. 977-987.

[24] Chiu, Y., Levandier, D., Austin, B., Dressler Rainer, A., Murray, P. T., Lozano, P. and Martinez-Sanchez, M., "Mass Spectrometric Analysis of Ion-Emission from Selected Colloid Thruster Fuels," *39th AIAA/ASME/SAE/ASEE Joint Propulsion Conference and Exhibit*, Huntsville, AL, AIAA Paper 2003-4848, 2003.

[25] Chiu, Y., Gaeta, G., Levandier, D. J., Dressler, R. A. and Boatz, J. A., "Vacuum Electrospray Ionization Study of the Ionic Liquid, [Emim][Im]," *International Journal of Mass Spectrometry*, Vol. 265, No. 2-3, 2007, pp. 146-158.

[26] Lozano, P. C., "Studies on the Ion-Droplet Mixed Regime in Colloid Thrusters," PhD Dissertation, Aeronautics and Astronautics Dept., Massachusetts Institute of Technology, Cambridge, MA, 2003.

[27] Ticknor, B. W., Anderson, J. K., Fritz, B. A. and Chiu, Y.-H., "Effect of Aspect Ratio on the Wettability and Electrospray Properties of Porous Tungsten Emitters with the Ionic Liquid [Emim][Im]," *46th AIAA/ASME/SAE/ASEE Joint Propulsion Conference & Exhibit*, Nashville, TN, AIAA Paper 2010-6618, 2010.

[28] Manzella, D. H. and Sankovic, J. M., "Hall Thruster Ion Beam Characterization," *31st AIAA/ASME/ASEE Joint Propulsion Conference and Exhibit*, San Diego, CA, AIAA Paper 1995-2927, 1995.

[29] Fernández de la Mora, J. and Loscertales, I. G., "The Current Emitted by Highly Conducting Taylor Cones," *Journal of Fluid Mechanics*, Vol. 260, No. 1, 1994, pp. 155-184.

[30] Gañán-Calvo, A. M., Dávila, J. and Barrero, A., "Current and droplet size in the electrospraying of liquids. Scaling laws," *Journal of Aerosol Science*, Vol. 28, No. 2, 1997, pp. 249-275.

[31] Ticknor, B. W., Miller, S. W. and Chiu, Y. H., "Mass Spectrometric Analysis of the Electrospray Plume from an Externally Wetted Tungsten Ribbon Emitter," *45th AIAA/ASME/SAE/ASEE Joint Propulsion Confernce & Exhibit*, Denver,CO, AIAA Paper 2009-5088, 2009.

[32] Fernández de la Mora, J., "On the Outcome of the Coulombic Fission of a Charged Isolated Drop," *Journal of Colloid and Interface Science*, Vol. 178, No. 1, 1996, pp. 209-218.

II.   ORTHOGONAL TIME-OF-FLIGHT MASS SPECTROMETRY AND ELECTRIC FIELD MODEL OF 1-BUTYL-3-METHYLIMIDAZOLIUM DICYANAMIDE ELECTROSPRAY

Shawn W. Miller

Boston College, Institute for Scientific Research, Chestnut Hill, MA 02467

Benjamin D. Prince, and Raymond J. Bemish

Air Force Research Laboratory, Space Vehicles Directorate, Kirtland AFB, NM 87117

Joshua L. Rovey

Missouri University of Science and Technology, Rolla, MO 65409

ABSTRACT

Orthogonal time-of-flight (TOF) measurements of the electrospray of 1-butyl-3-methylimidazolium dicyanamide at controlled flow rates from 0.05 to 2.18 nL/s are presented. The TOF measurements show two distinct droplet distributions with mass-to-charge ratio of 2,000 to 40,000 amu/q and 50,000 to 300,000 amu/q. These droplets are multiply-charged species. The wide mass-to-charge distribution results from variation in the electric field surrounding the parent jet during droplet formation. For the studied flow rates, a nominal electric field of 0.5 V·nm^{-1} exists on the jet structure. Additionally, the data show that the charged species emitted in the electrospray beam vary in mass and charge with flow rate. The beam composition changes from containing ions to a composition dominated by massive droplets. The combination of TOF and quadrupole measurements suggest that ionic liquid electrospray from 0.05 to 2.18 nL/s does not conform to the traditional view of emission from the electrospray cone-jet. The emitted species indicate that the primary jet tapers down resulting in large mass droplet ejection, but also suggests that secondary structures emanate from the primary jet. These structures are responsible for much of the ions and smaller mass droplets detected by the

TOF instrument. Additionally presented is an electrostatic model that was developed using the data for 0.3 and 2.18 nL/s from a quadrupole based experiment. The electrospray electrostatic model does reproduce the electric field and related potential conditions necessary for ion emission from the cone-jet structure, which occurs at the emission zones corresponding to locations assumed in literature of near the transition region (i.e. neck) and the jet tip.

1. INTRODUCTION

Electrospray is an electrostatic method for generating charged particles from a conductive liquid surface. The technique is commonly used in mass spectrometry, electrostatic deposition, electric propulsion, and the food and pharmaceutical industries. Of interest to this particular article is the application of electrospray to electric propulsion and achieving efficient thrust from an emission source. Physically, an electrospray is created by applying a potential to a liquid meniscus. The meniscus deforms into a conical shape often called a Taylor cone, which is the result of the balance between the forces of the applied electric field and the liquid surface tension. At the end of the cone, a jet forms; this is the single Taylor cone-jet structure typical of modern electrospray applications. The transition region or neck between the cone and jet is the point where current flow changes from the bulk conduction to convective current within the jet. This region serves as the region of ion generation, where an ion is defined as a single molecular ion or small ion clusters (e.g. a molecular ion clustered with a few neutral pairs). At the neck, the electric field conditions on the liquid surface are sufficiently large that only such ions are emitted. Generally, this ion emission is described by an Iribarne and Thomson mechanism [1]. Further downstream in the jet structure, wave perturbations start to set in resulting in droplet generation, defined here as large clusters of neutral pairs with excess charges from the jet. As a result, electrospray is considered a generator of droplets, ion-droplet mixed mode, or just ions in a pure ionic regime.

The emission modes of the electrostatic acceleration of charged particles from a fluid surface were first categorized by Cloupeau in the late 1980's and early 1990's [2-4]. Different emission modes were described and illustrated throughout those references. Of interest was the stable cone-jet structure that formed and the different associated emission phenomena that were observed from the highly charged jets. For general consideration, two phenomena or instabilities were observed and discussed: varicose or axisymmetric, and lateral kink. Varicose instability formation was based on Rayleigh's work on jet instabilities and produced droplets sized correspondingly to the wavelength of the active wave perturbation [5]. Lateral kink instability was based on a lateral component

developing within the wave perturbation leading to a whipping motion of the jet. The whipping jet would break up into randomly sized droplets.

When interest was renewed in electrospray in the 1990's and early 2000's, studies focused on the evaluation of the cone-jet current output, describing droplet size and breakup, Coulombic fission of droplets into ions, and ion evaporation under an electric field. These studies continued with the electrospray of polar fluids over a range of conductivity values [6-8]. Electrospray of ionic liquids (ILs) began in earnest in the early 2000's with works from Romero-Sanz *et al.* and Lozano [9, 10]. Both authors evaluated the current output of the electrospray beam of 1-ethyl-3-methylimidazolium tetrafluoroborate ([Emim][BF$_4$]) and identified ionic liquids as a source of heavy molecular ions. At sufficiently low flow rates only the first three ionic species were identified using time-of-flight measurements. Several using ionic liquid propellants have been analyzed for various attributes, emitters, or performance. The recent work by Miller *et al.* presented the angle-resolved output of current, mass flow rate, mass spectrometry, and retarding potential of the ionic liquid 1-butyl-3-methylimidazolium dicyanamide ([Bmim][DCA]) using a quadrupole mass spectrometer based system [11]. The mass spectrometer was limited to a scanning range of 1000 amu/q; however, near field measurements indicated that masses greater than 1000 amu/q were also present. These unknown masses impacted the propulsive performance of the electrospray system. The relationship between the output current of this system and flow rate followed the scaling law proposed by Fernández de la Mora [7].

Numerical solutions have been proposed for the droplet generation from a formamide liquid surface; the most recent being proposed by Higuera and Carretero. Higuera's [12, 13] numerical model combined the Iribarne and Thomson mechanism [1] with Navier-Stokes equations providing an evaluation of the Laplacian of the electric potential of the simulated cone-jet flow. Expressed in dimensionless values, the numerical solution showed ion emission peaking, as expected, within the transition region, the maximum electric field condition occurs in the neck, and the bulk current of the beam decreases as the transition to the convective current occurs. Ultimately, Higuera numerical solution captured the effect of evaporated ions from the transition region coexisting with charged drops generated from the jet producing a simulated mixed

mode. Additionally, Higuera showed that ion evaporation provided most of the current source while most of the mass was still carried as droplets. Carretero [14, 15] took the one-dimensional Navier-Stokes numerical solution further by incorporating a particle-in-cell component. This allowed an analysis with beam divergence angles and provided energy distributions. None of these studies looked at the static cone-jet structure and the associated electric field. Recent molecular dynamics simulations of the ionic liquid 1-ethyl-3-methylimidazolium tetrafluroborate have examined the flow of the IL through a simulated capillary under several electric field conditions [16]. The authors report the formation of a Taylor cone at the tip of the capillary and the formation of a jet ,under some electric field boundary conditions, with ion emission occurring at the end of this jet at considerably less electric field magnitude than that reported for a static, gas phase droplet [17].

The propellant used for this paper is the ionic liquid 1-butyl-3-methylimidazolium dicyanamide, which like many ILs is a molten salt below 100 C. As a liquid, the ILs are quasi-neutral with both cations and anions dispersed throughout the fluid. These liquids tend to have a high conductivity (order of 1 S/m), negligible associated vapor pressure, and a low surface tension or viscosity (order of 40 mN/m or 30 cP, respectively). These physical properties enable ILs to be utilized at room temperature for electrospray purposes. Operated either in opposite polarity or in an alternating current mode, the IL electrospray enables ion emission without the need for an electron neutralizer downstream to neutralize the emitted flow. ILs are also of particular interest due to achieving lower mass emission during extraction. As seen in Figure 1.1, ILs can achieve a broad range on the low end of the mass-to-charge ratio spectrum unlike traditional polar liquids and solvents such as glycerol and formamide. Colloids from these fluids tend to be larger droplets on the order of nanometers or micrometers in diameter.

In this study, work was complete using a orthogonal time-of-flight experimental setup to identify not only the ionic species but the droplet distribution from 0.05 to 2.18 nL/s for the electrospray of [Bmim][DCA]. Electrostatic field data is presented to define the static conditions surrounding an assumed cone-jet derived from the data of Miller *et al*. [11]. The focus of this paper is on evaluating the emission of the beam and discussing the sources of the droplets and ions from the cone-jet structure.
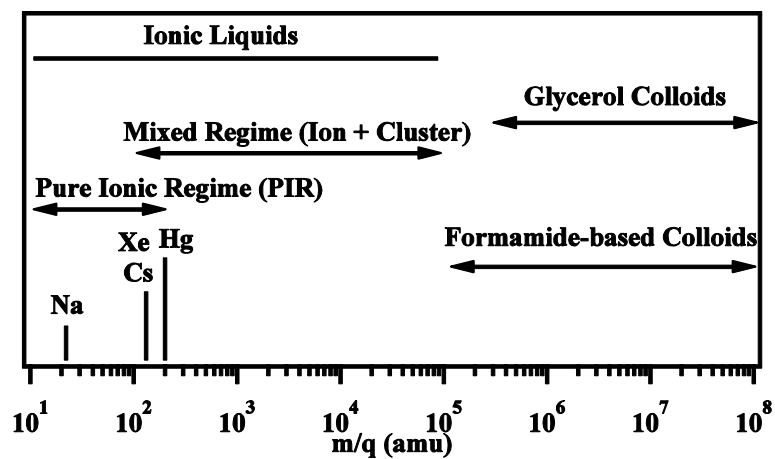
Figure 1.1.   Room temperature ionic liquids mass-to-charge range in comparison to other colloidal liquids [18].

2. EXPERIMENTAL SETUP

The experimental system combines a previously described rotatable electrospray capillary ion source [11] with an orthogonal time-of-flight (TOF) setup as seen in Figure 2.1. The electrospray source is simply the pairing of an extractor plate with a 1.5 mm diameter aperture and a conductive emitter (i.e. metal coated fused-silica capillary at 50 μm diameter) set approximately 1.5 mm apart.   In the work reported here, the ion source is operated with a +900 V needle potential and -900 V extractor potential to achieve a stable ion beam. Emitted charged species from the source are introduced into a lens stack and the lens voltages are optimized for maximal current measured on the Faraday cup. In addition to measuring the current, mass deposition can be determined using the quartz crystal microbalance (QCM) that is mounted along with the Faraday cup on a linear translation stage beyond the pulsing region.

Once an optimized beam is achieved, two pulsing plates extract charged species into an Einzel lens and deflector plate before entering the field free flight tube. A retarding potential analysis of the total current from all of the emitted species indicated that the median axial kinetic energy is 550 V, thus setting the base voltage of the plates. For improved resolution of the low m/q species, the pulsing plates are operated at 550 and 785 V for a pulse duration of 2.5 μs, pulser voltage of 235 V, and repetition rate of 500 Hz. Alternatively for optimized droplet collection (125,000 amu/q or greater), the pulsing plates operate at 550 and 925 V and the pulse set to nominally 400 V, 10 μs pulse length, and 250 Hz repetition rate. The Einzel lens and deflector remain fixed at 350 and 0 V, respectively, for all data collection.

Once in the flight tube, the ion beam will either impact a microchannel plate (MCP) detector or encounter the electric field of the reflectron. When in the reflectron operational mode, the ion beam tracks the flight tube, effectively doubling the flight length. Typical voltages for the reflectron are 300 and 1300 V. Variation of the reflectron voltages did not alter the ion or droplet distribution. The MCP detectors are paired with a multi-channel scaler triggered at a rate of 500 Hz (e.g. ion collection) or 250 Hz (droplet collection) to record ion impacts within a specific binned time interval

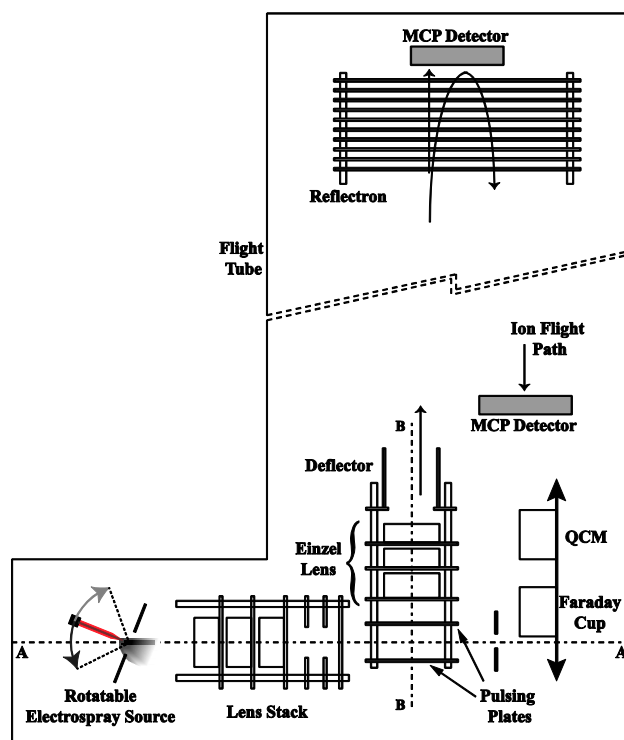with bin size of 640 ns/bin. Each TOF spectrum was normalized with an identical number of pulses.

Figure 2.1. Orthogonal TOF experimental setup featuring translating Farday cup and QCM. The ion beam is optimized using the Faraday cup and QCM before the pulsing plates are activated. The ion beam flight occurs along axis A-A, but the pulsing plates redirect the ion beam along axis B-B into the TOF flight tube.

3. METHODS

SIMION 8.1 software [19] was used to model the electric field and associated potential of the static cone-jet structure for the flow rates of 0.30 and 2.18 nL/s. This model assumes only ion emission and does not support any fluid dynamics associated with the jet. The SIMION model is represented by the Poisson equation of Eq. (1) where the surface current density is calculated from the conductivity, K, and potential, Φ. The Poisson equation is solved in SIMION to determine the potential and electric field conditions. The simulated cone-jet structure is assumed to have a Taylor cone of 49.3 deg half angle with a base size the same diameter as the emitter capillary (i.e. 50 μm). Further, a uniform jet diameter with no taper and round end is assumed. Equation (2) is used to determine the electric field in the transition region, E_{TR}, between the Taylor cone and the jet. Here, the propellant properties of conductivity and surface tension, γ, along with the flow rate, Q, and the permittivity, ε_0, contribute to the electric field calculation. The model assumes that the electric field must converge from the cone and from the jet to a local maximum at the transition region to a value determined in Eq. (2) [8]. By equating Eq. (2) and (3) through the electric field, the jet radius, R_{Jet}, is determined at a specific flow rate and assumed constant along the entire jet length. As a result, only the ionic liquid physical properties, electric field, and the previously determined current, I, (see reference [11]) are used to establish the radius of the jet structure extending from the Taylor cone.

The model was built using the data set and the experimental setup of Miller *et al*. [11]. The model space represents the region of potential between the capillary emitter, extractor, and the downstream detector plate. Each of these is held at a fixed potential of 500, -1700, and 0 V, respectively. The model space is constructed to a width of 46 mm and length of 21 mm, where the length represents the spray axis. 21 mm denotes the distance to the near-field targets of the experimental setup in the reference [11]. Figure 3.1 presents a zoomed image of the cone-jet generated for a flow rate of 2.18 nL/s. The potential lines are represented by the red lines and are generally perpendicular to the jet direction while the electric field contour lines are depicted in blue and surround the cone-

jet. The maximum electric field locations occur at the transition region and the jet end where the field contour lines converge. The minimum electric field magnitude of 0.6 V·nm^{-1} required to generate emission has been proposed by Prince *et al*. [20]. This field condition provides a lower limit on regions contributing to emission in the model.

$$KV^2\Phi = 0 \tag{1}$$

$$E_{TR} = \frac{\gamma^{1/2}}{\varepsilon_0^{2/3}}\left(\frac{K}{Q}\right)^{1/6} \tag{2}$$

$$R_{Jet} = \frac{2\left(E_{Jet}Q\varepsilon_0\right)}{I} \tag{3}$$

$$P^* = 4.2\times10^{-5}\left(\frac{q}{m}\right)^{-1/2}\left[I\cdot\Phi^{-3/2}\right] \tag{4}$$

Four assumptions about the SIMION model have been instituted. 1) The modelled cone-jet structure is a resistive conductor. This is done to achieve electric field conditions at the end of the jet structure so that a sufficient field above 0.6 V·nm^{-1} occurs at the end of the jet and ions can be emitted. 2) The perveance, P*, (see Eq. (4)) of the emitted charged particles is low and space charge effects can be neglected. The perveance is calculated using the data of the previously mentioned source [11]. 3) The experimentally determined most probable kinetic energy value obtained from a retarding potential analysis (RPA) occurs along the centerline of the emission plume at the end of the jet structure. This value is also provided from reference [11]. The determination of the length of the jet in the model is based on this assumption. The jet length is severed at an appropriate crossing potential line established from the RPA data. It is then necessary to iterate SIMION to achieve a length comparable to the actual jet described by the data. 4) The terminus of the jet is rounded. The round end is consistent with the curvature or cusp that liquids assume under electric fields such as in liquid metal ion sources and in the transition region of the cone-jet. The cusp regions concentrate the surrounding electric field and serve as structures for emitting charged species.
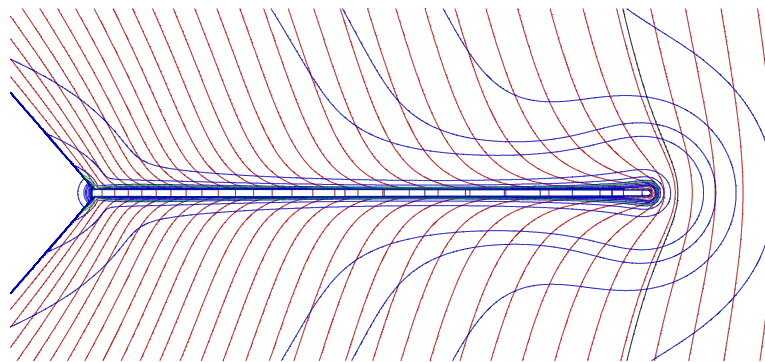
Figure 3.1. Model of the cone-jet structure at 2.18 nL/s for electrostatic simulations. The red lines represent the potential, while the blue lines represent the electric field contours.

4. RESULTS

4.1. EXPERIMENTAL DATA

TOF measurements were collected for flow rates ranging from 0.05 to 2.18 nL/s. The flow rates of 0.05, 0.10, and 0.20 nL/s were not directly measured as in reference [11] but instead assumed using a linear extrapolation to the data in the above reference. The measured [Bmim][DCA] count versus flight time raw data has been manipulated in three ways: (1) converting the initial position axis (i.e. charged species time dispersal) to an appropriate mass axis, (2) curve fitting the distinct distribution peaks (e.g. droplets and obvious ions) and recording fit details (i.e. central distribution value), and (3) integrating different regions of the curve fits to obtain intensities as a percentage of the total contribution of each component. The figures that follow provide illustration of the electrospray beam TOF measurements.

Figure 4.1 contains the mass spectra of the [Bmim][DCA] electrospray beam for flow rates (a) under 1.0 nL/s and (b) over 1.0 nL/s with the source emission angle set at 0 deg. The primary graph features the droplet mass distribution ($m/q > 2000$ amu/q) for up to 300,000 amu/q. The inset plot depicts the magnification of the mass distribution from 0 to 1,200 amu/q. This narrowed range covers the singly-charged ion spectra. For flows between 0.05 nL/s to 0.30 nL/s there is little if any high mass species (> 2,000 amu), but by 0.46 nL/s, there is a distribution of larger masses, primarily confined to below 60,000 amu/q. This distribution is well modelled by two Maxwell-Boltzmann distributions. At 0.82 nL/s, there is a significant contribution from a higher mass distribution centered at approximately 90,000 amu/q. As the flow rate increases from 0.30 to 0.82 nL/s, the intensity contribution from the low mass droplets (2,000 – 60,000 amu/q) increases. In addition, the width of the mass distribution for these species also increases with flow rate. At the higher flow rates depicted in Figure 4.1(b), there are two distinct distributions: one, the low mass component, containing mass values within the 2000 to 37,500 amu/q range, and the other, the high mass component, within the 50,000 to 300,000 amu/q range. This high mass component shifts further toward 300,000 amu/q with increasing flow rate. The ion inset of Figure 4.1(a) shows the $Bmim^+$, $Bmim^+([Bmim][DCA])$, and $Bmim^+([Bmim][DCA])_2$ species (i.e. the $n = 0, 1, 2$ ion species) at low flow rates. In

addition, ion fragment components (i.e. ions less than 139 amu/q and composed of parts of the Bmim$^+$ molecule) and trace amounts of the $n = 3$ species are seen. At the higher flow rates portrayed in the ion inset of Figure 4.1(b), those same species are observed but $n = 4$ and $n = 5$ are additionally observed in trace amounts while the $n = 3$ provides a count intensity of 10,000. In both inset plots, the ion peaks are broadened due to the broad distribution of energies (velocities) the ions have post-emission. The small ion species measured match the spectral results obtained in the experiments described in reference [11]. Additionally, at around 0.30 nL/s, the $n = 1$ species shows the greatest intensity in agreement with the experimental results presented in reference [11].

Figure 4.2(a) illustrates the intensity percentage of each component of the electrospray beam as a function of flow rate. For simplicity, the data are restricted to components that are low mass droplets (i.e. peak at 2,000 to 40,000 amu/q), high mass droplets (i.e. peak at 50,000 to 300,000 amu/q) and the ions (i.e. any of the singly-charged species from 0 to 1,200 amu/q). The integrated values of each component are combined and processed as a percentage of the total integrated intensity for a given flow rate. The ion integral is evaluated as the intensity in the m/q region less than 2000 amu/q. The high and low mass droplet integral values are determined by integrating the TOF spectrum over the above mentioned ranges. Only intensity from ions was observed at the lowest flow rates. As the flow rate increases to 0.20 nL/s, the low mass droplet component appears and begins increasing as a percentage of the total signal until approximately 0.6 nL/s. At this flow rate, the highest mass droplets are first measured and this component begins its relative percentage increase as the flow rate increases. By 1.0 nL/s, all three components have reached an approximate steady state with respect to their percentage contribution to the total current.
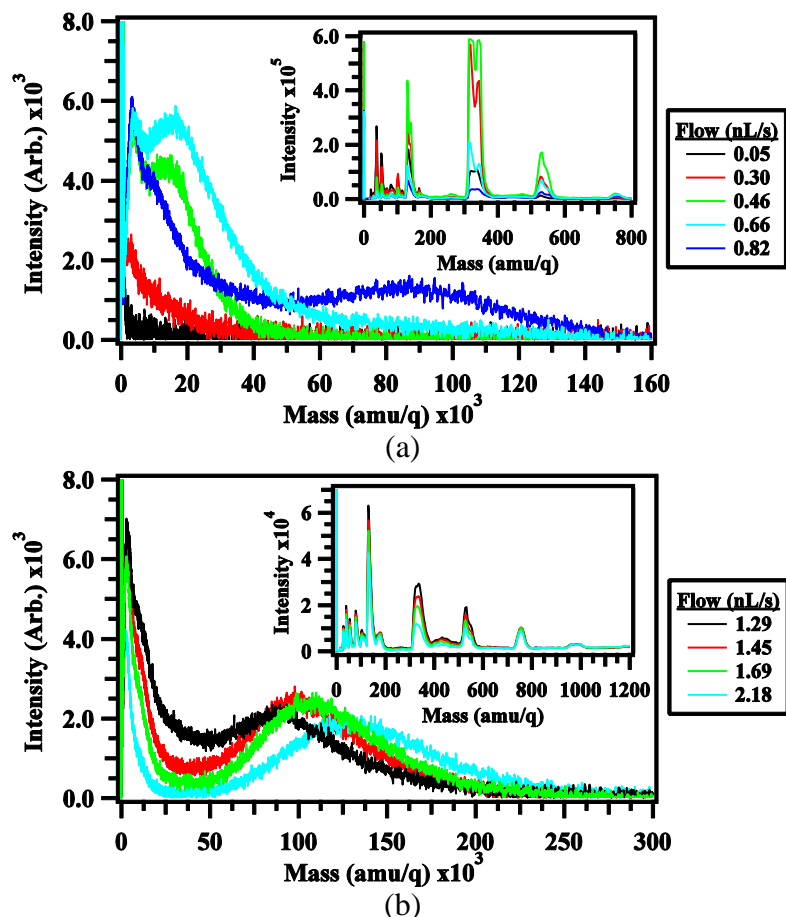
Figure 4.1. Mass Spectra of a [Bmim][DCA] IL beam as a function of select flow rates; (a) flow rates under 1.0 nL/s and masses up to 160,000 amu/q, (b) flow rates above 1.0 nL/s and masses up to 300,000 amu/q. Inset graphs illustrate the mass spectra of the associated rate for masses under 1200 amu/q.

The ion contribution can be divided and independently analyzed further by integrating each curve fit of the ions. These ion contributions are seen in Figure 4.2(b), where the $n = 0$ to 3 species are compared against the low and high mass droplet components. The $n = 0$ to 3 [Bmim][DCA] species components are shown as a percentage of the total ion signal (i.e. only the total intensity due to $n = 0$ to 3). While the $n = 0$ and 1 species dominate the results for under 1.0 nL/s, the $n = 2$ and 3 species increase and contribute a greater percentage at higher flow rates. The $n = 1$ species is the dominant ion between 0.11 and 0.82 nL/s. The $n = 3$ species is the only singly-charged, higher mass included in the figure, since the species above $n = 4$ have effectively zero

intensity. Interestingly, the $n = 0$ to 2 species persist above 1.0 nL/s each contributing to approximately 5 to 10% of the intensity, which is counter to the mass spectra presented in reference [11]. These species (above 1.0 nL/s) and the fragments were not seen in the mass spectra using a quadrupole mass spectrometer. That experiment used a directly targeted electrospray beam instead of an orthogonally targeted beam. Most likely these ion species and the fragments seen in Figure 4.1 at high flow rates are due to orthogonal pulsing of the beam and the increased flight time compared to the quadrupole, which ultimately introduce additional artifacts into the beam.

One aspect of the droplet mass distributions is the well-defined features which can be fitted by a Gaussian or Maxwell-Boltzmann distribution curve. Figure 4.3 shows the change in distribution peak center value as a function of flow rate. Note that two low mass droplet peaks are listed. These provide the peak values of Maxwell-Boltzmann fits to the low mass curve in Figure 4.1. The high mass peak was fit to a single Maxwell-Boltzmann distribution. The low 1 peak is nominally 5,000 amu/q while the low 2 peak is nominally 10,000 amu/q for all flow rates. The high mass component continuously increases with flow rate.

The data illustrated in Figure 4.4 were collected without the reflectron as opposed to the previous data. Figure 4.4 shows the angle distribution of the droplet component of the electrospray beam when the central axis of the beam is at 0 deg and 45 deg. Only three select flow rates are shown for clarity. The flow rate increases from 0.30 nL/s to 2.18 nL/s from top to bottom. The primary plots represent the low mass distribution under 60,000 amu/q, while the inset graph shows the high mass distribution in the 100,000's of amu/q range. The low mass distribution is present only at 0 deg, but no mass is ejected at higher angles for 0.30 nL/s. At 1.07 nL/s, the high angle mass is present but the distribution of the high mass droplet is only starting to appear in the measurement of the middle inset. By 2.18 nL/s, both mass distributions are present at 0 deg, but only the low mass distribution exists at 45 deg in a well-defined count. This indicates that the mass generating source is mostly along 0 deg, but either the source emits more low mass at high angle with increasing flow rate or other sources that emit low masses become active and contribute at high angle with increasing flow rate.
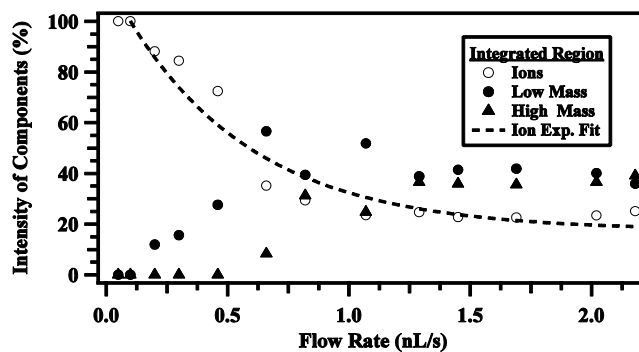
(a)
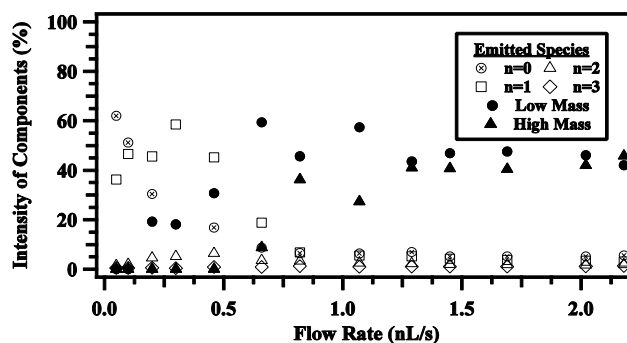
(b)

Figure 4.2. Integrated ion beam component breakdown as a percentage of total beam intensity vs. flow rate; (a) the ion component represents the total integral of masses less than approximately 2000 amu/q, (b) the ion contribution is divided into individual components from $n = 0$ to $n = 3$. As noted in (a), the ion component exponentially decays with the increasing flow.
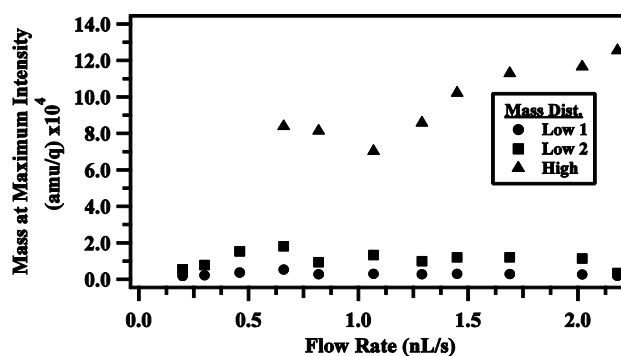
Figure 4.3. Maximum intensity in the mass distribution as a function of flow rate. The high mass droplet distribution has a single peak that increases with flow rate, whereas the low mass droplet distribution has two peaks (low 1 and low 2) that remain approximately constant with flow rate.
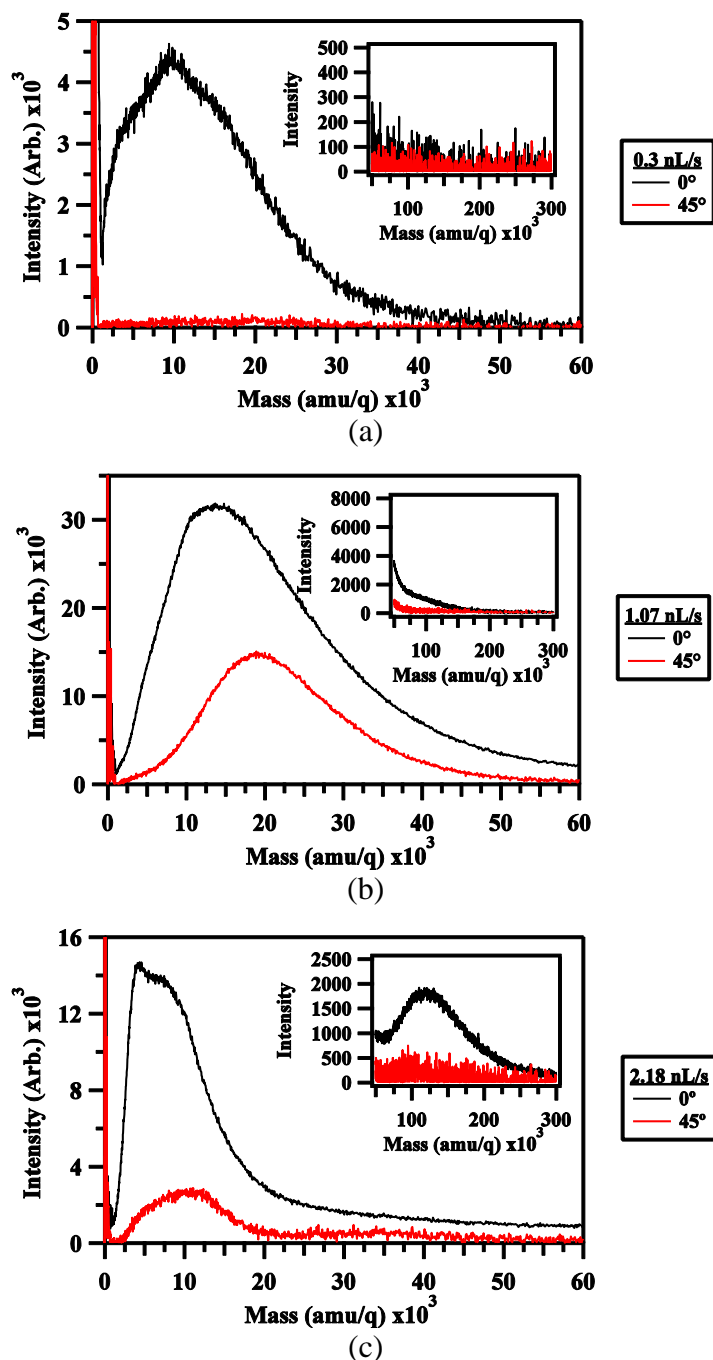
Figure 4.4. Angle distribution of the mass profiles greater than 2000 amu/q for the angles 0° and 45° using a linear flight configuration instead of the reflectron. Each of the three main plots represent the distribution at a different IL flow rate starting at the lowest on top and increasing going down; (a) 0.30 nL/s, (b) 1.07 nL/s, and (c) 2.18 nL/s. The main graphs illustrate the lower mass distribution up to 60,000 amu/q. The inset graphs represent the higher mass distribution from 50,000 to 300,000 amu/q. Note that higher mass distribution does not take on a log normal distribution until the highest flow rates and does not appear at 45°.

4.2. ELECTRIC FIELD MODEL DATA

The SIMION model is used to simulate the ejection of ions from the surface of a cone-jet structure, map the apparent trajectories, and identify the ion distribution downstream of the source. All ions were stopped 21 mm from the extraction plate as would happen in the experimental setup of Miller *et al*. [11]. At this distance, a Faraday cup or QCM detector would intercept the electrospray beam. Figure 4.5 shows the simulated ions positioned around the cone-jet for the two flow rates. Ions are classified by the starting locations of neck, side, and tip. The jet radii, established by Eq. (2) and (3), are 7.0 and 13.0 nm for 0.30 and 2.18 nL/s, respectively. The lower graphs in Figure 4.5(a) and (b) show the initial ion distribution while the upper graphs show the distribution after considering the local electric field value. Any ion at a position where the electric field was less than 0.6 V·nm^{-1} was eliminated and thus only the contributing distribution was left as seen in the upper graphs. Again, 0.6 V·nm^{-1} is the minimum electric field condition per reference [21] that ion emission could occur using molecular dynamic simulations. Two different contributing distributions appear for the two flow rates. For 0.30 nL/s in Figure 4.5(a), ions born at locations above 0.6 V·nm$^{-1}$ exist at the transition region (i.e. highlighted by neck and side ions) and at the tip of the jet. For 2.18 nL/s, only the ions at the tip of the jet contribute. By calculating Eq. (2), it is immediately noticeable that the electric field value (0.45 V·nm^{-1}) in the transition region for 2.18 nL/s is below the field limit value and is reflected in this model.

Figure 4.6 illustrates the associated potential energy at the ion starting locations. Again, the lower graphs of the (a) and (b) figures reflect the initial distribution while the upper graphs reflect the contributing distribution. The potential energies are restricted by the electric field limit to the same locations as was done in Figure 4.5. Since the charge is transported by conduction in the cone, the potential in the neck region for both flow rates is a constant 500 eV (i.e. the emitter bias voltage of reference [11]). In the jet, the charge transport is by convection and as a result, the potential energy lines penetrate into the jet resulting in the decaying distribution seen in the lower plots. Notice the potential energies reflect nominally 300 eV at the tip and 500 eV at the transition. Such energies are reflective of the distributions of the retarding potential by Miller *et al*. [11].
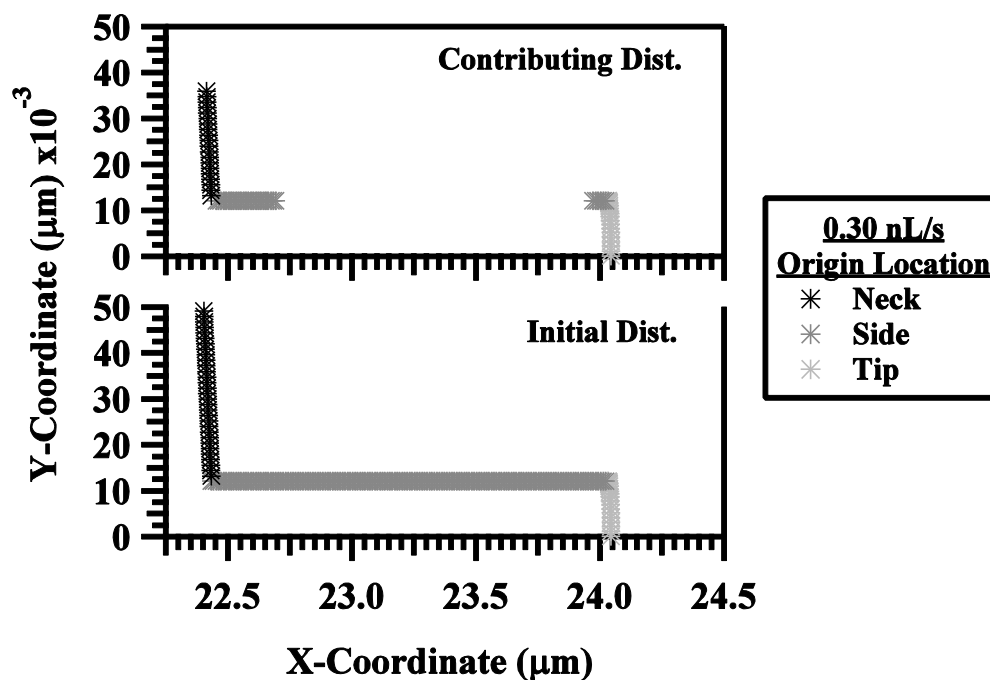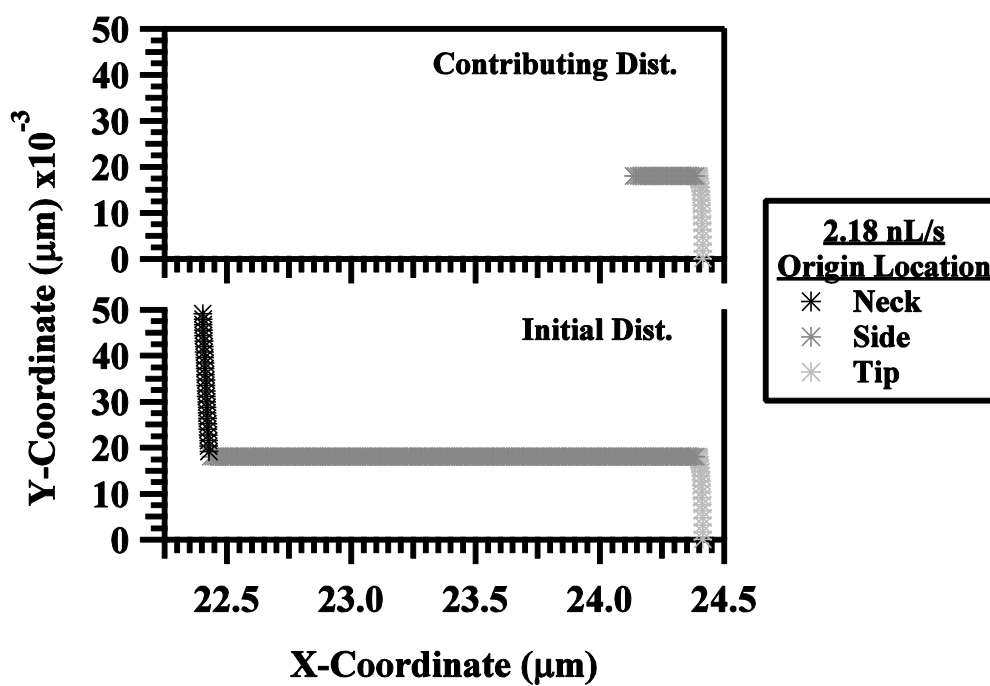
Figure 4.5. Starting location of simulated ions in model for two flows; (a) 0.30 nL/s distribution and (b) 2.18 nL/s distribution. The initial distribution represent all ions considered and the contributing distribution represent only the ions that are at a location where the electric field is greater than 0.6 V·nm^{-1}.

Figure 4.7 shows the electric field value distribution at the ion locations for both flow rates. The horizontal dashed line marks the 0.6 V·nm^{-1} level. As expected, the electric field along the jet length is less than the transition region field; however, the electric field increases as the tip is approached and the potential energy lines become concentrated around the tip. A stronger field exists at the tip of the 2.18 nL/s than at the tip of the 0.30 nL/s case assuming a stationary, uniform sized jet.

Figure 4.8 illustrates the angle distribution at the downstream detector of the ions by the three starting locations. The vertical axes indicate the corresponding initial electric field value. For each plot, two initial ion kinetic energies are show to illustrate the change of angular spread if ions are released with energy greater than at a thermal condition. Again, the dashed line represents 0.6 V·nm^{-1} limit. In Figure 4.8(a), the distribution of the tip ions is limited to less than 15 deg. As kinetic energy is increased, the tip distribution narrows to less than 5 deg meaning there is little to distinguish the tip ions of various kinetic energies from each other. Ions along the side and neck are confined to narrow, vertical distributions above 15 deg; however, these distributions depend on the initial kinetic energy of the ions. If the kinetic energy is near 0.1 eV then the side and neck ions are limited between 15 deg and 25 deg, but increasing the energy results in vertical bands of the neck ions between 15 deg and 25 deg while the side ions spread out to a 40 deg distribution. Based on the ion angular measurements of Miller *et al*. [11], the kinetic energy does not reach 50 eV for the 0.30 nL/s flow rate since the measurements do not show a 40 deg spread. In Figure 4.8(b), the tip distribution is broader, extending to approximately 25 deg for the 0.1 eV case. This does overlap with the ions from side and neck regions. Notice that similar to the 0.30 nL/s case, the 50 eV side and neck ions reach 45 deg. This suggests, based on the work by Miller *et al*. [11], that the initial ion kinetic energy is not necessarily near 0.1 eV as was the case with 0.30 nL/s in order to get an ion distribution out to 45 deg.
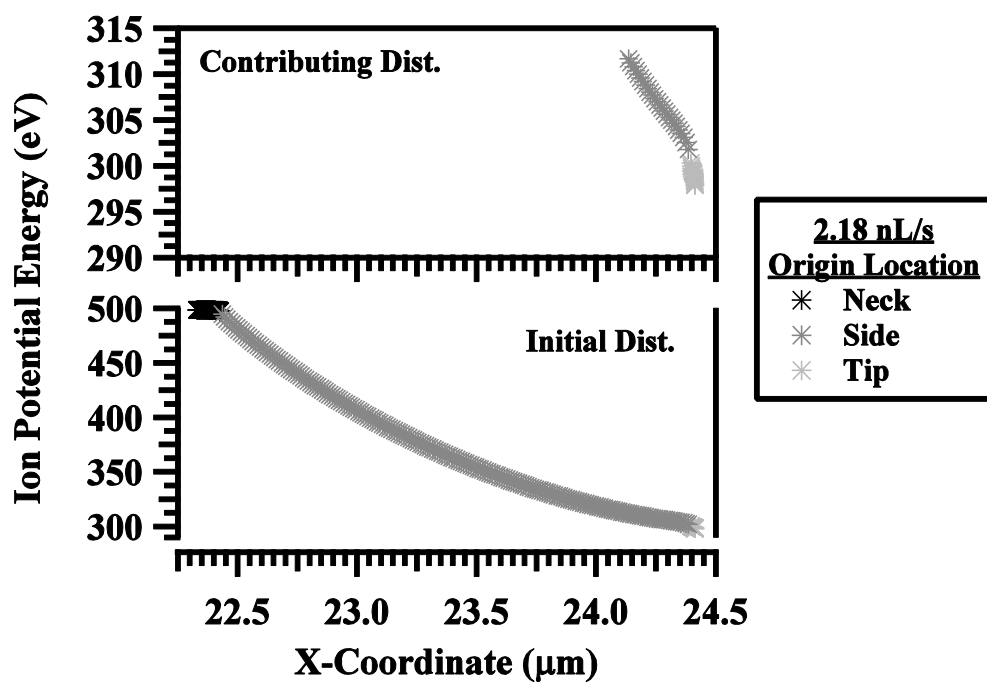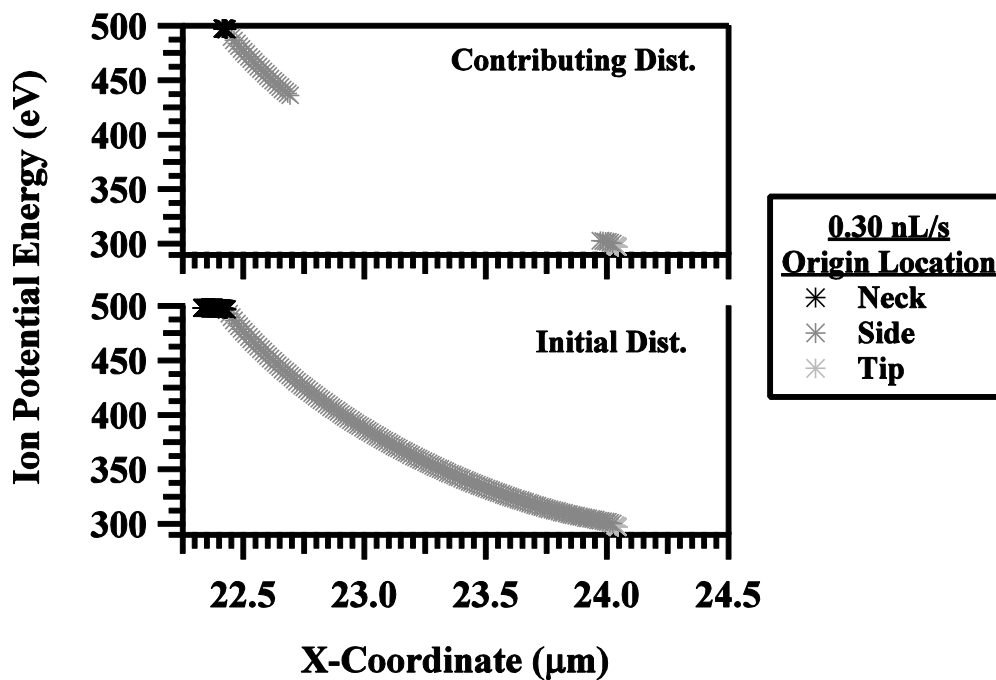
Figure 4.6. The potential energy of simulated ions at associated starting location along the cone-jet; (a) 0.30 nL/s and (b) 2.18 nL/s. The contributing distribution considers that the electric field is greater than 0.6 V·nm^{-1}.
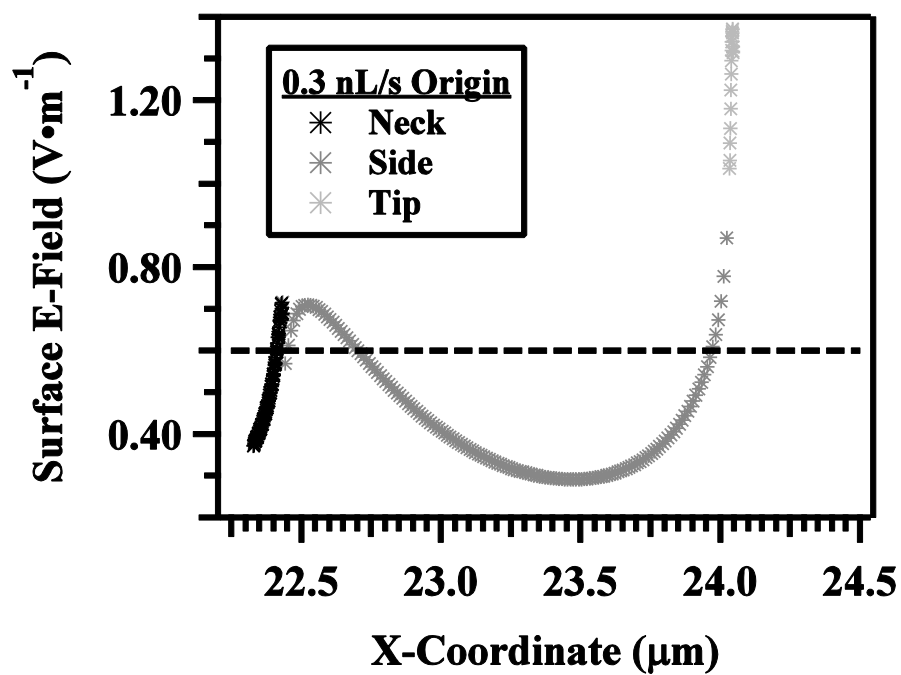
(a)
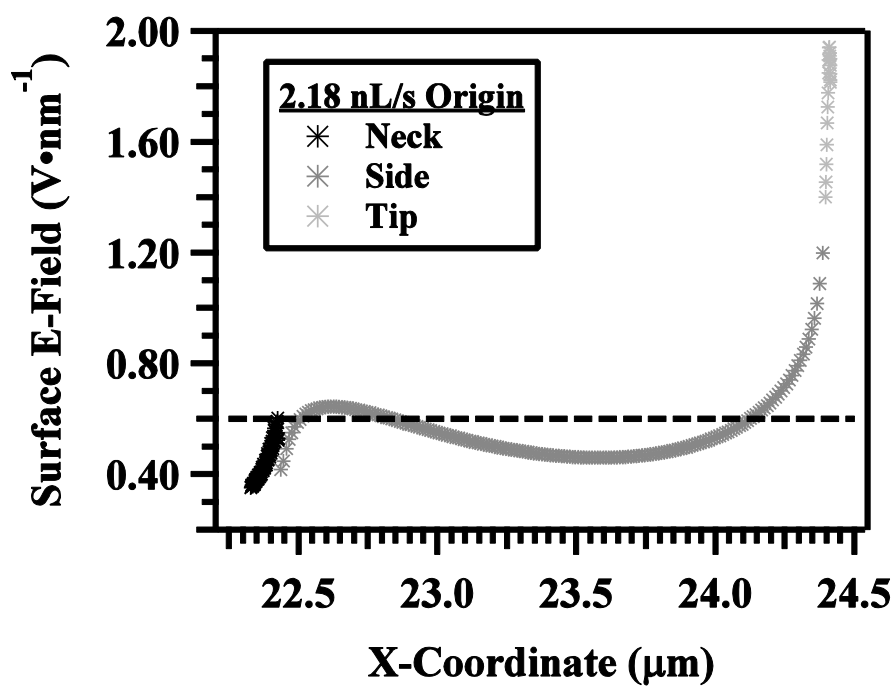
(b)

Figure 4.7. The electric field along the simulated cone-jet structure; (a) 0.30 nL/s and (b) 2.18 nL/s.
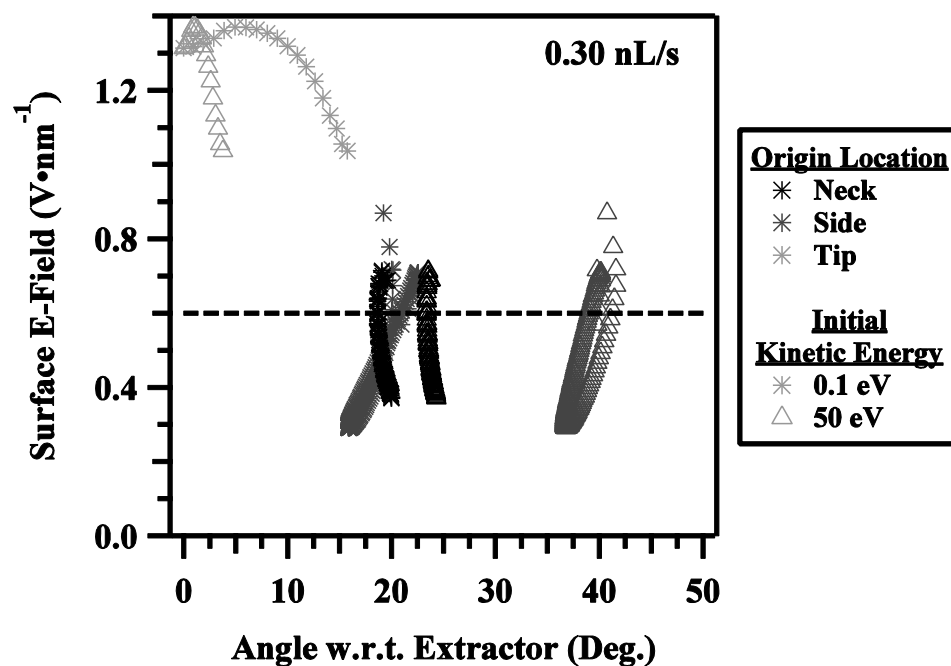
(a)
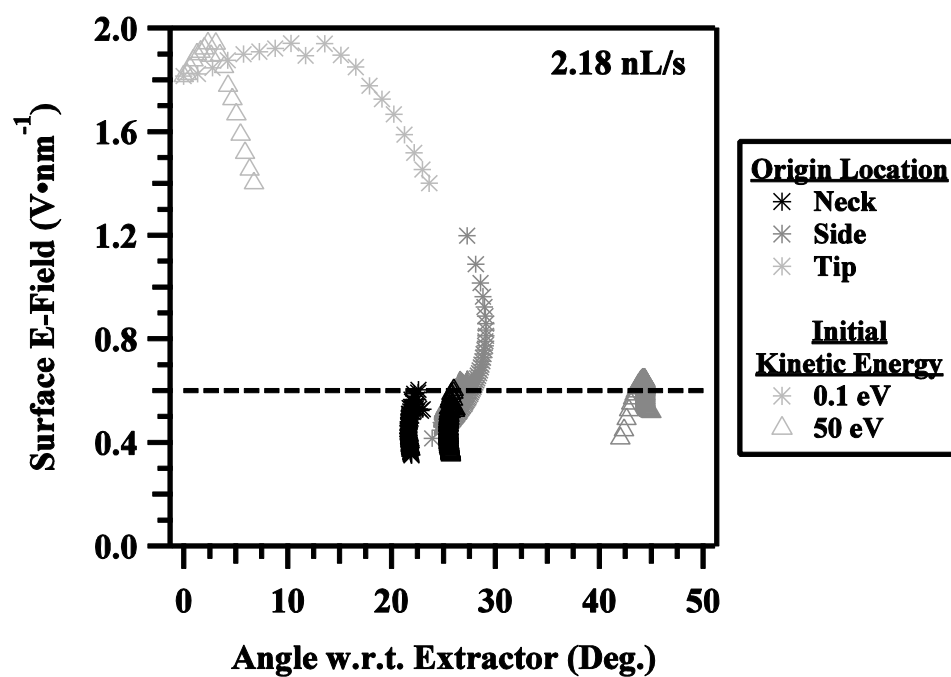
(b)

Figure 4.8. The angular distribution ions at the three origination locations and the associated initial electric fields with initial kinetic energies of 0.1 and 50 eV for two different flow rates; (a) 0.30 nL/s and (b) 2.18 nL/s. the 0.6 V·nm-1 electric field is highlighted by the dashed line. Any data point above the line may be extracted where as any point below the electric field is too weak for ion extraction.

5. DISCUSSION

The discussion is divided into three parts for further consideration.

5.1. EVALUATION OF THE TOF ELECTROSPRAY COMPOSITION

The TOF data collected in this study directly corroborates the results of Romero-Sanz in reference [9]. The results Romero-Sanz reported were TOF current measurements indicating singular inflexion points for various flow rates with gradual current decays as time increased. Count intensity is used in this study instead of current measurement as was done by Romero-Sanz. As a result, clear intensity peaks of individual species at a given time interval are seen. The species peaks are illustrated in both plots of Figure 4.1. Monitoring the intensity of the electrospray beam resulted in discreet ion species under 1200 amu/q. The intensity of low mass ions (i.e. $n = 0, 1, 2$) decreases and higher mass ions ($n = 3, 4, 5$) intensity increases with flow rate, which is also supported by ion intensity profiles of Figure 4.2(b). This clearly indicates the development of higher massed, singly-charged species within the emission with increasing flow rate. Along with the ions are the plots of droplet contribution from 0 to 300,000 amu/q. The droplet component of the beam is not confined to narrow, distinguishable peaks, but instead broad distributions due to the various associated charge configuration (i.e. singly-charged or multiply-charged) with the droplets. There are three distinct distributions that appear in the recorded droplet distributions, which have not been observed in previous studies due to measurements solely based on current collection. Up to three distributions are considered due to the double Maxwell-Boltzmann fit required for approximating the low mass droplet distribution (under 50,000 amu/q). Again, these distributions are not completely fixed, but shift location as flow rate is increased. The low mass distribution shifts to lower masses suggesting that at a high enough flow rate (i.e. above 2.18 nL/s) the distribution may disappear or become more distinct in shape. The high mass droplet distribution shifts to higher mass-per-charge range with increased flow rate (see Figure 4.2(b)). This result points toward larger droplets being produced with increasing flow rate.

The electrospray beam component profiles illustrated in Figure 4.2(a) not only provide a breakdown of the beam charged species population, but also lend support to the conclusion of previous electrospray studies. Gamero-Castaño, Fernández de la Mora, and Lozano produced current measurements of electrosprayed NaI/Formamide solutions dependent on flow rate [8, 10]. In both cases, the current registered decreased with decreasing flow rate, but would reach a minimum before exponentially growing as the flow rate approached zero. Additionally, Lozano calculated supposed droplet current dependent on flow rate which matched the ion current until the minimum value was reached. Beyond the minimum value the ion and droplets diverged and droplet current rapidly decayed to zero with zero flow rate. The ion currents and calculated droplet current profiles of those studies are reflected in Figure 4.2(a) even though this figure illustrates percentage of intensity. The ion profile exponentially decays while the droplet profile develops within the electrospray beam with increasing flow. At approximately 0.50 nL/s, the droplet profile develops and should result in a convergence of the ion and droplet currents as happened in Lozano's current measurements. All data above this flow rate represents a droplet dominated beam and thus a droplet dominated current profile. Figure 4.2(b) does reflect this since the data is further broken down by ion components. The ion components represent less than 10% of the beam intensity above 0.50 nL/s. Further, the droplet profile in Figure 4.2(a) and (b) should continue to increase in percentage at higher flow rates, but since the beam broadens beyond the lens optics acceptance angle some of the droplet data is missed. This beam broadening was shown in the work by Miller *et al*. [11].

The mass-to-charge range covered by Figure 4.1 for the flow rate regime is consistent with the *m/q* results of Miller *et al*. [11]. The *m/q* ratio based on the scaling laws used in that work fit with the present TOF results; however, those *m/q* ratios were assumed to be singly-charged where the TOF results in Figure 4.1 suggest, as will be discussed below, multiply-charged droplets present in the beam. Further, the TOF measurements show that even at rates below 2.18 nL/s droplets of various sizes and charges exist. The corresponding spectra show that a single, equally sized droplet (evidenced by the broad *m/q* distribution) does not exist within the studied flow regime. Further analysis of the droplet components is required to ascertain if varicose instability

is involved and whether nominally determining the droplet size based on the 1.89 ratio of droplet-to-jet radius from Rayleigh instability is valid as has been assumed in the past [10].

5.2. DROPLET ANALYSIS

Of the two mass distributions seen in Figure 4.1, the higher mass component (50,000 to 300,000 amu/q) is the best candidate for further analysis of droplets and discussed first. Figure 4.1 depicts the m/q distribution for each flow rate, but the charge conditions on the distributions are unknown. Two approaches are used to determine the charge distribution, droplet mass, and electric field conditions for these high mass droplet distributions. Before addressing these two approaches, it is worthwhile to discuss why an assumption of a singly-charged droplet is not appropriate. If the large m/q droplets were assumed to be singly-charged, the resulting droplet radius, at the most probable value, would only vary from 3.12 to 3.60 nm over the entire flow rate range of 0.82 to 2.18 nL/s. R_{jet}, as calculated from Eq. (3), varies from 8.73 to 12.10 nm over this same range, which expects droplet radii of 16.5 to 22.87 nm assuming the 1.89 scaling. Moreover, at a flow rate of 0.82 nL/s, the droplet radius would have to encompass the range of 2.30 to 3.91 nm to include the entirety of the observed m/q data. A radius ratio, assuming singly-charged droplets, varying from 1.7 to 1.5 is found for the droplet size at the high m/q to low m/q end for flow rates from 0.82 to 2.18 nL/s. This indicates a droplet radius and jet radius variation of at least 50%. Finally, the total mass flow over the range of 0.82 to 2.18 nL/s is expected to increase by a factor of 2.65, yet the most probable value increases only by ~1.5 times in the single charge assumption.

5.2.1. Rayleigh Charge Limit Approach. The first approach to determine the charge conditions and associated droplet masses assumes that the lowest m/q value represents the maximum charge limit on the droplet. Stated another way, the low m/q end of the large m/q species is not closer to zero because droplets formed at those m/q values exceed the Rayleigh limit and are not stable. It is assumed that the droplet mass is approximately constant for the entire range and that all other m/q values are cases where $q < q_{ray,}$ the Rayleigh charge limit. The minimum m/q of a distribution is assigned at 10% of the total intensity on the low m/q side of the distribution shown in Figure 4.1.

The maximum charge limit is expressed as the Rayleigh charge limit, q_{Ray}, as stated in Eq. (5). Here, the only physical property of the IL required to define the charge limit is the surface tension, γ. Using the minimum m/q for a distribution (see m/q_{Ray} in Table 5.1) in Eq. (6) and assuming a spherical volume for the droplet, the m/q ratio can be related by surface tension and density, ρ, to the droplet radius, r_{Drop}. From Eq. (6), the Rayleigh charge is determined and the corresponding jet radius, r_{Jet}, is evaluated using Eq. (7). The 1.89 factor in Eq. (7) is assuming the droplets are generated by a varicose instability breakup of the parent jet structure [5]. This assumption is valid given that the high mass distribution is only observed along the 0 degree axis of the electrospray beam.

With the known Rayleigh charge limit, the mass of the droplet can be calculated from the m/q value. Applying all of the charge values less than the charge limit at the calculated mass will provide a full range of m/q values. In Figure 5.1, the charge distribution across the high mass component is shown for 0.82 to 2.18 nL/s using this approach, and depicted for the intensity as a function of the droplet charge. Noticeably, the most probable charge at the maximum intensity is not near the Rayleigh limit. For increasing flow rate, the charge distributions broaden and shift to contain more charges as the droplet volumes increases. Figure 5.2 depicts the normalized data of Figure 5.1. Here, the intensity has been normalized using the maximum intensity value of the distribution for the specific flow rate. The charge distribution has been normalized using the maximum charge value indicated in Figure 5.1 where the maximum charge is actually the Rayleigh charge limit. As seen, there is general agreement at all flow rates that the maximum intensity occurs at a charge ratio of approximately 50-55% of the Rayleigh limit with the exception of the outlier at 0.82 nL/s, where the maximum occurs at approximately 35%. The data at 0.82 nL/s contains the greatest overlap between the low mass and high mass droplet components and it is possible that the determination of the Rayleigh charge was not accurate. These figures suggest that the droplets are not near the charge limit, but slowly approaching the limit as the flow rate is increased. Previous work has shown that the Coulombic fission does not set in until 80% of the Rayleigh charge [6, 10, 19, 22, 23].
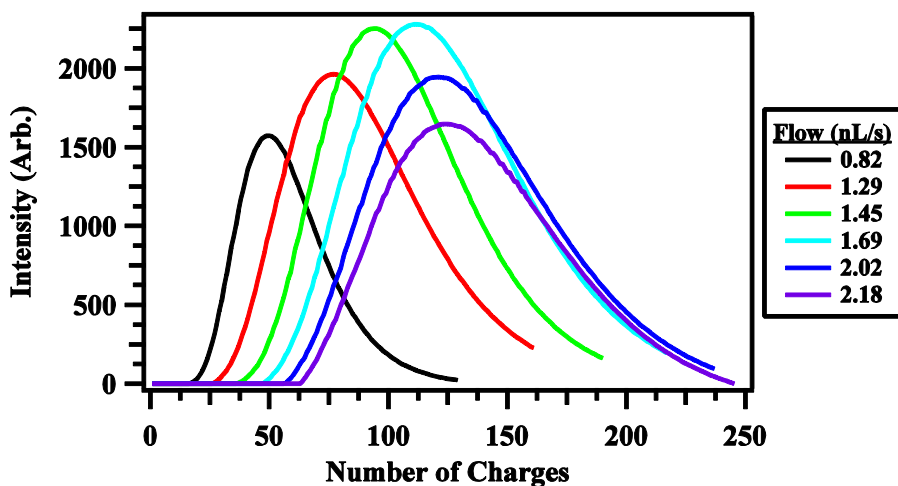
Figure 5.1. The observed high mass distributions specified in terms of the number of charges across the distributions. The upper end of charge represents the Rayleigh limit for a given droplet size.
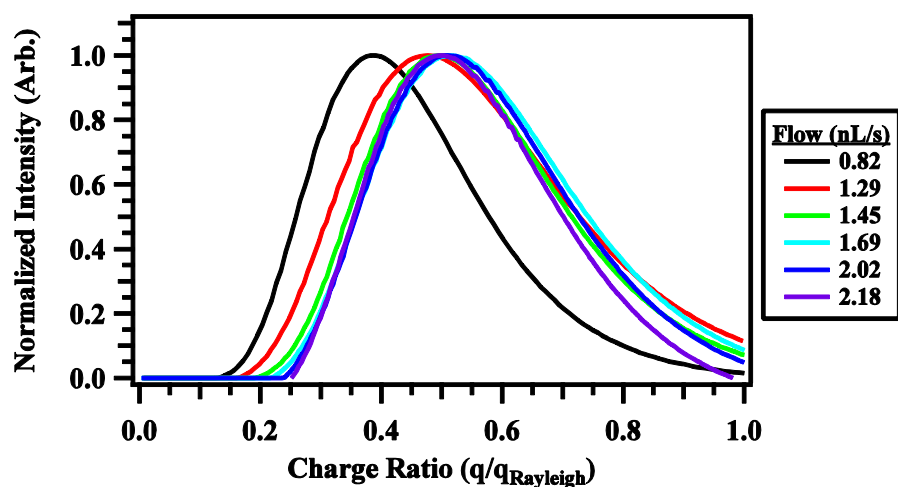
Figure 5.2. The high mass distributions specified in terms of charge ratio and normalized intensity. The data is normalized using the maximum intensity for a given distribution, while the charge ratio is simply normalized based on the maximum Rayleigh charge limit.

Table 5.1 is generated from the conversion of the m/q distributions to charge distributions. This table lists not only the m/q_{Ray} and mass values, but also the charge and

dimension values. The mass of the droplets effectively quadruples from 4.1 x 10^6 to 15.8 x 10^6 amu over the flow rates analyzed and resulting in a significant amount of mass being highly charged. The most probable charge in each distribution is represented by q_{MP}. Here, the most probable charge is essentially 50% of the Rayleigh charge listed. The low and high ends of the charge range are found to increase with increasing flow rate and the rationale for the specific progression is discussed below. Dimensional characteristics can be gleaned from the charge values assessed so far in the analysis. Already the maximum droplet radius due to charge has been established by Eq. (5) and Eq. (6). Since a varicose breakup is assumed for droplet generation, the droplet volume should be equivalent to some cylindrical volume on the jet. Equation (7) provides the relationship between drop and jet radii. Rayleigh determined that this cylindrical length, l, is equal to the wavelength, λ, of the perturbation within the jet [5]. The jet cylinder length is specified by Eq. (8). Given the charge and dimensional data in Table 5.1, the electric field and surface charge density on the droplet and jet cylinder can be established. It is assumed that the equivalent mass and charge found within the droplet proportionally existed within the jet cylinder as well. Within this assumption scheme, the mass of the droplet is found to increase by a factor of 3.85 over the flow rate range, significantly larger than the expected 2.65 factor from the mass flow over the same range. Some portion of this excess factor has to offset the decreasing mass values of the low mass droplets which have significantly narrowed (moved to lower m/q values) over this same range. A discussion of the two low mass species is presented below. The expected jet radius (Eq. 3) at the extremes was 8.7 and 12.1 nm and this analysis generates jet radii of 6.1 and 9.6 nm, respectively, which, while not quantitatively exact, trends correctly. The expected jet radius calculated in Eq. 3 is the radius of the jet at the transition region which may reduce as the jet extends into vacuum. As such, a slightly smaller jet radius is to be expected.

Table 5.2 lists the electric field and charge density for each flow rate calculated from using Eq. (9). The first step to determining the field and charge density values is to establish the surface area of the spherical droplet and cylindrical jet. The next step is simply to divide the charge within the given volume by the associated surface area. Conserving mass, the two volumes are the same and the charge is assumed to be applied

only to the surfaces. Finally, the only step remaining is to evaluate Eq. (9). Each set of electric field and surface charge density values reported in Table 5.2 can be divided by origination and charge condition. The data either originate in the droplet or jet (i.e. subscript *Drop* or *Jet*). The charge condition is either at the Rayleigh limit (i.e. subscript *Ray*) or the most probable value (i.e. subscript *MP*) in the distribution. It should be noted that the resulting surface charge density and electric field values are assumed to be uniformly applied. This assumes an ideal case for the cylinder, not the actual case where the electric field and thus surface charge density varies along the cylinder of the jet as with SIMION results reported in Figure 4.7 and Figure 4.8. Notice that the electric field due to Rayleigh on the jet cylinder at 0.82 nL/s is approximately 1.0 V·nm^{-1} and decreases with rising flow rate. This suggests that at flow rates below 0.82 nL/s the field is strong enough for ion evaporation from the jet to occur. Of course this does assume near Rayleigh charge within the droplet contained within that jet segment. Additionally, Eq. (10) as specified by Gamero-Castaño and Fernández de la Mora [8] can be calculated to determine the radius of the droplet necessary for Coulombic fission to occur. This equation utilizes only IL physical properties. The $F(\varepsilon)$ value is equivalent to 4.6 as per Miller *et al*. [11]. Calculating Eq. (10) reveals the R_d values listed in Table 5.1. Gamero-Castaño specified that the droplet radius must be greater than the value calculated by Eq. (10). In comparing the droplet radius due to Rayleigh and the R_d value, the droplets featured in Figure 4.1 are well below this criterion and therefore no fission of droplets is occurring.

$$q_{Ray} = \left[8\pi^2 \gamma \left(2r_{Drop}\right)^3\right]^{1/2} \tag{5}$$

$$\frac{m}{q_{Ray}} = \frac{\left(\frac{4}{3}\pi r_{Drop}^3\right)\rho}{\left[8\pi^2 \varepsilon_0 \gamma \left(2r_{Drop}\right)^3\right]^{1/2}} = \frac{\rho\left(r_{Drop}\right)^{3/2}}{6\left(\varepsilon_0 \gamma\right)^{1/2}} \tag{6}$$

$$r_{Drop} = 1.89 \times r_{Jet} \tag{7}$$

$$l = \lambda = 4.508 \times 2\left(r_{Jet}\right) \tag{8}$$

$$\sigma = \varepsilon_0 E \tag{9}$$

$$R_d = \left[\frac{36\varepsilon_0}{F^2(\varepsilon)} \right]^{\frac{1}{3}} \left(\frac{Q}{K} \right)^{\frac{1}{3}} \tag{10}$$

Table 5.1. Charge and dimensions of the electrospray beam for given flow rates.

Flow (nL/s)	m/q_{Ray} (amu/q)	Mass, m (amu, x10^6)	Charge Range	q_{Ray}	q_{MP}	r_{Ray} (nm)	r_{Jet} (nm)	l (nm)	R_d (nm)
0.82	32,411	4.1	17-128	128	50	11.6	6.1	55.3	22.8
1.29	40,776	6.6	27-161	161	77	13.5	7.1	64.4	26.4
1.45	47,991	9.1	37-190	190	94	15.1	8.0	71.8	27.5
1.69	54,776	11.8	48-216	216	112	16.4	8.7	78.4	28.9
2.02	59,892	14.2	57-237	237	121	17.5	9.2	83.2	30.7
2.18	63,165	15.8	64-250	250	124	18.1	9.6	86.2	31.5

Table 5.2. Uniformly applied electric field and surface charge density of the electrospray beam for given flow rates.

Flow (nL/s)	E_{MPDrop} (V/nm)	$\sigma_{MP\ Drop}$ (C/m^2)	$E_{MP\ Cyl}$ (V/nm)	$\sigma_{MP\ Cyl}$ (C/m^2)	$E_{Ray\ Drop}$ (V/nm)	$\sigma_{Ray\ Drop}$ (C/m^2)	$E_{Ray\ Cyl}$ (V/nm)	$\sigma_{Ray\ Cyl}$ (C/m^2)
0.82	0.54	0.0047	0.40	0.0036	1.42	0.0126	1.03	0.0092
1.29	0.61	0.0054	0.46	0.0040	1.28	0.0113	0.96	0.0085
1.45	0.6	0.0053	0.45	0.0040	1.21	0.0107	0.91	0.0080
1.69	0.6	0.0053	0.45	0.0040	1.16	0.0102	0.87	0.0077
2.02	0.57	0.0051	0.43	0.0038	1.12	0.0099	0.84	0.0075
2.18	0.55	0.0048	0.41	0.0036	1.10	0.0098	0.83	0.0073

5.2.2. Near-Field Condition Approach. An alternative approach is used to determine the droplet and jet cylinder size by using the experimentally determined emitter current (I), nominal mass flow rate ($\dot{m}$), and the m/q value at the peak of the large droplet distribution in addition to the density of the ionic liquid ($\rho = 1062$ kg·m^{-3}). Within the assumption that the majority of the total current and mass flow is contained in the high mass droplets, the $I/\dot{m}$ ratio is first multiplied by the density and then subsequently by the volume of a cylinder (e.g. $V_{cyl} = \pi r_{MPJet}^2 l_{MP}$) where l is determined from Eq. (8) to yield a total charge, q, at the end of the jet. Assuming all charge in this volume becomes the most probable charge of the resulting spherical droplet and that the radius of the spherical drop scales according to (10), the radius of the drop is calculated such that this charge is equivalent to 50% of the Rayleigh limit. The 50% value is chosen based on previous experimental findings for flow rates below the fission limit [2, 24, 25]. The r_{MPJet} value is iterated until the contained jet charge is equivalent to the 50% Rayleigh charge of the associated droplet.

The jet radius, r_{MPJet}, established using the near-field matches closely to the scaling radius by Fernandez de la Mora and Loscertales [7] in Eq. (11) (see Table 5.3). The deviation in radius value is no worse than 3%. The excellent agreement between the respective R_{jet} values in light of the presence of significantly smaller droplets (the low m/q drops) suggests that the determination of R_{jet} is at best an upper limit. Unfortunately, the relative intensity of the low mass to high mass droplets was subject to alignment conditions in this experiment and subsequently, no quantitative ratio could be determined. The presence of low mass species (either ion or low mass drops) in any quantity will have significant impacts on the respective current breakdown while leaving the mass largely unaffected (nearly all mass on the large droplets). By using this $I/\dot{m}$ approach, the most probable droplet is increased in size, mass, volume, and charge compared against the droplet determined from the other method. Effectively, the electric field and surface charge density on the jet cylinder and most probable droplet remain nearly constant (see Table 5.4) between the two approaches.

$$R_{Jet} = 0.2 \left[\frac{Q\varepsilon\varepsilon_0}{K} \right]^{1/3}$$

(11)

Table 5.3. Charge and dimensions of the electrospray beam for given flow rates using near-field data.

Flow	m/q_{MP}	Mass, m	q_{MP}	r_{MPDrop}	R_{Jet}	r_{MPJet}	l_{MP}
(nL/s)	(amu/q)	(amu, x10^6)		(nm)	(nm)	(nm)	(nm)
0.82	109,000	11.7	107	16.4	8.5	8.7	78.1
1.29	128,000	16.1	126	18.2	9.9	9.6	86.7
1.45	135,000	18.1	133	18.9	10.3	10	90.2
2.18	178,000	31.2	175	22.7	11.8	12	108.1

Table 5.4. Uniformly applied electric field and surface charge density of the electrospray beam for given flow rates based on near-field data.

Flow	E_{MPDrop}	$\sigma_{MP\,Drop}$	$E_{MP\,Cyl}$	$\sigma_{MP\,Cyl}$
(nL/s)	(V/nm)	(C/m^2)	(V/nm)	(C/m^2)
0.82	0.58	0.0051	0.43	0.0038
1.29	0.55	0.0049	0.41	0.0036
1.45	0.54	0.0048	0.40	0.0036
2.18	0.49	0.0044	0.37	0.0033

In the end, the conclusion about the droplet size remains consistent with previous electrospray work. Time-of-flight studies have delineated current versus time plots indicating the presence of droplets within the electrospray beam. Images capturing the droplet formation have provided size and scaling laws defining droplets for various flow regimes. Now the nature of the charge conditions on the droplets has been established

through this study on low flow IL emission. With the establishment of a varicose instability, each droplet generated equates to the same volume and thus mass. The variation with previous electrospray experiments and lacking data has been with defining the charge contained within the droplets. For each droplet generated, the charge condition exhibited tends to be unique and variable, but the charge remains consistent around a most probable value for a given flow rate. The result is that the emission from 0.82 to 2.18 nL/s features uniform droplets, but not uniform charging. Only a consistent charge distribution exists for the flow regime.

5.2.3. Low Mass Distributions. The low mass droplets consist of two separate components, *C1*, centered at roughly 3000 amu/q, and *C2*, centered near 11,500 amu/q. In contrast to the bin resolution of ~70 amu/bin at 80,000 amu/q, the experimental binning of ions in these low *m/q* regions had a spacing of 8-10 amu per bin which should allow the resolution of individual ions if they are not overlapped. These two low mass droplet components were curve-fit simultaneously at each flow rate with two log normal distributions. An attempt to assign both of these distributions to singly-charged ion-cluster progressions was first attempted, but such an assumption required the full-width half maximum (FWHM) of each *n*-cluster to be greater than 200 amu to generate the smoothness observed in the raw data. The $n = 1$ to 5 ion species observed in the ion region had FWHM values of approximately 30-40 amu, and while isotope effects are likely to broaden the FWHM values as *n* increases, it should not occur to the extent necessary to give widths of 200 amu by $n = 14$ (~3000 amu/q).

Alternatively, an approach involving the simulation of the resulting mass spectrum was attempted. This approach used a Gaussian distribution of droplet sizes given by a center radius, r_{center}, and a FWHM, r_{FWHM}; and a Gaussian distribution of charges given by a center charge, q_{center}, taken as its percentage of q_{Ray} and a FWHM, q_{FWHM}, also taken as a percentage of q_{Ray}. The simulation stepped through each droplet radius with 0.005 nm resolution. At each radius value, all possible *m/q* values were calculated with intensities derived from the amplitude of droplets at that radius and the amplitude factor for drops having that *q* value. The resulting summed mass spectrum was compared to the log normal fit of respective low mass component. Each *m/q* value obtained with these distributions was assumed to have a FWHM of 50 amu along the

mass axis. An example fit and droplet parameters are shown in Figure 5.3 for the 2.02 nL/s flow rate under an assumed center q value of 50% of q_{Ray}. In the course of the simulations, it became clear that all of the simulation parameters were not necessarily independent of one another; the width of the distribution could be increased by either increasing r_{FWHM} or q_{FWHM} or by some combination of both. In addition, the choice of a q_{center} value largely determined the acceptable r_{center} value. In the large droplet investigation, this limitation was overcome by the assumption of an approximate single mass and, consequently, a single radius of the droplet. This assumption, paired with the assumption that the lowest m/q value is that of the ion at the Rayleigh limit, greatly simplified the analysis.

In these simulations, providing a q_{center} on the low end, such as 20%, resulted in droplet radii that were smaller than those with larger q_{center}. For the *C2* component, a resulting radius would be near 2 nm, and significant structure that should be within the instrumental resolution would be apparent in the simulated data. At the opposite end, choosing q_{center} at ~80% resulted in larger droplets with radius near 5 nm for the *C2* component and had smooth curvature at the mass axis resolution of the instrument. Unfortunately, the drops with these large q values had difficulty in reproducing the asymmetry of the data on the higher m/q end of the spectrum for most flow rates. In light of these two constraints and drawing upon the finding of the most probable q/q_{ray} value from the large mass droplet investigations of ~0.5, a decision to fix q_{center}/q_{Ray} at 0.5 was made [2, 24, 25]. While these fits reproduce the data quite well, it is possible that these solutions are just one of many acceptable solutions. Without the experimental ability to resolve the droplets into their respective charges, it is impossible to be certain that the predictions of the simulation are completely accurate.

The resulting best fit parameters for reproducing the experimental data are shown in Table 5.5 for both the *C1* and *C2* components assuming q_{center} = 50% of q_{Ray}. The *C1* component is largely unchanged over the entirety of the flow rates sampled with a radius of nearly 2.0 nm and a droplet width, as determined by the FWHM, of 1.5 to 1.9 nm. At a radius of 2.0 nm, these drops encompass 1 to 9 charges, centered at 4 or 5 charges. The relative population of each charge becomes more equal as the flow rate increases (i.e. q_{FWHM} of 55% increasing to 95%). The *C2* component is significantly more dynamic as

the flow rate increases. The best fit radius indicates that droplets with a spherical radius of approximately 4.1 to 3.6 nm exist over the entire flow rate range sampled. In Figure 4.1, the *C2* component can be seen to narrow as the flow rate is increased and the simulations capture this change in the droplet distribution decreasing from nearly 2.0 nm to 0.85 nm. In addition, the charge distribution also narrows, changing from spanning approximately 8 to 18 charges (FWHM) at 0.82 nL/s to 8 to 12 charges at 2.18 nL/s. Assuming spherical shapes to these droplets, the associated mass, calculated at the center radius value of *C1* is approximately 21,500 amu and *C2* is 170,000 amu.
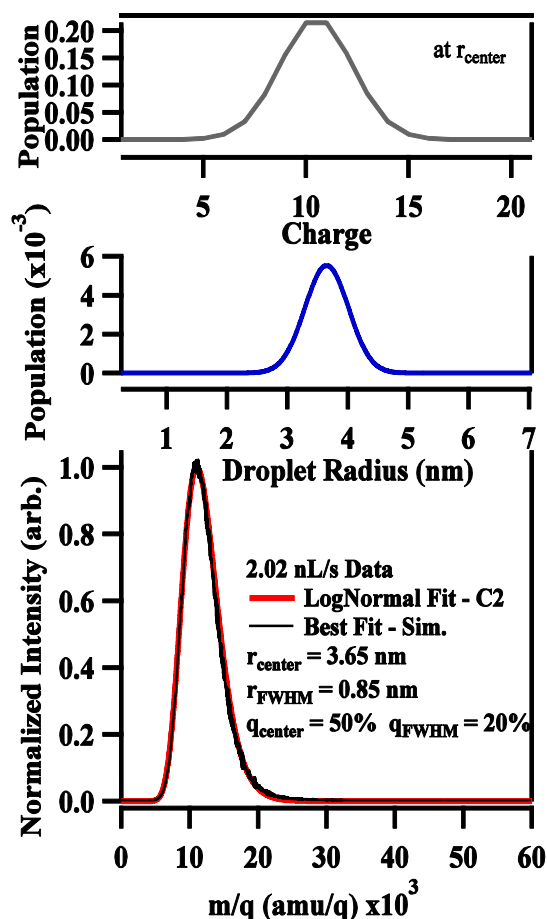

Figure 5.3. Example simulation results for the *C2* component. The bottom trace details the fit to the raw data and the simulation with the described parameters. The middle trace depicts the droplet radius distribution that composes the best fit while the top trace details the charge distribution at r_{center}.

5.2.4. Electric Field Condition. The charge distribution in the studied flow regime is due to the electric field at the droplet origin on the jet. In the case of the high mass droplet, this field condition is at the jet tip before the droplet breaks away. Figure 5.4 illustrates the uniform electric field condition on the cylinder (Figure 5.4(a)) and on the droplet (Figure 5.4(b)) for the normalized population. The field condition is achieved by applying the charge distribution in Figure 5.2 to the surface of the representative volume (dimensions in Table 5.1) and simply solving for the analytical field solution. The width of the field condition in Figure 5.4 is noticeable. This is an indication of electric field fluctuation at the tip, but the peak value is the most probable electric field most of the time. The field condition at the jet tip is nominally 0.5 $V \cdot nm^{-1}$ while for the droplet the field increases to approximately 0.6 $V \cdot nm^{-1}$. These electric field values are consistent for any of the flow rates listed. The electric field on the jet is limited at 1.0 $V \cdot nm^{-1}$, which is the field condition that ionic species are most commonly field evaporated from an IL surface. The field stays above 0.2 $V \cdot nm^{-1}$, never reaching zero, indicating that a field is always present on the jet and during droplet production. The electric field condition of the droplet increases above that of the jet tip. The upper limit shifts toward 1.3 $V \cdot nm^{-1}$. The increased field value is simply due to the surface area minimization that occurs when going from a cylindrical volume to a spherical one.

Direct comparison of Figure 5.4 to the SIMION electric field results in Figure 4.7 cannot be made given that Figure 5.4 illustrates a uniform electric field at the tip while Figure 4.7 shows a variable field. However that distinction does not eliminate drawing some comparison. The electric field at the jet tip is at a value comparable to the field at the transition region. It is a known fact that the electric field drops off in both directions (i.e. toward the cone and toward the tip) away from the neck [8]. Since the tip field is nearly as high as the transition electric field, the SIMION model is correct to say the field approaches a minimum along the jet, but then returns to a second local maxima. The field conditions reported in the SIMION models are on the same magnitude order as the field values reported in Figure 5.4. For the flow rates studied, the SIMION reproduces the similar electric fields around the jet, but not necessarily the correct field, since the fluid dynamics are not captured in SIMION.

Table 5.5. Best fit parameters for the simulations assuming $q_{center} = 0.5*q_{Ray}$.

Flow	C1 r_{center}	C1 r_{FWHM}	C1 q_{FWHM}	C2 r_{center}	C2 r_{FWHM}	C2 q_{FWHM}
(nL/s)	(nm)	(nm)	(%)	(nm)	(nm)	(%)
0.82	2.0	1.5	55	4.0	2.0	35
1.29	2.0	1.5	55	4.1	2.0	35
1.45	2.0	1.7	55	4.0	1.3	35
1.69	1.9	1.9	65	3.6	1.0	25
2.02	1.9	1.9	65	3.7	0.95	25
2.18	1.9	1.9	95	3.6	0.85	13

5.3. EMISSION SOURCE OF THE CONE-JET STRUCTURE

The striking conclusion from the TOF and electric field model data is that the electrospray of the IL [Bmim][DCA] within 0.05 to 2.18 nL/s does not conform to traditional view of the cone-jet mode emission. The emission is not simply ionic species originating from the transition region while droplets are generated from the jet. In this study, any ions emitted from the jet do not appear to originate from secondary ions generated by Coulombic fission of discharged droplets, field extracted ions from droplets, or thermally unstable droplets ejecting mass to obtain energy stability. Based on the data presented here, ions are generated from both the transition region and the jet when the surrounding electric field is sufficiently high (see Figure 4.7). Droplets are produced for all but the lowest flow rates; however, the physical properties of the IL (e.g. negligible vapor pressure) reduce the possibility that ions are generated from pure evaporation off the droplets. The conclusion is that the IL cone-jet is formed no matter the flow rate for all rates studied in this work; however, the tip shape and configuration of the jet varies with the flow rate. The jet breaks up into secondary structures near the tip instead of arriving as a unified structure. These secondary structures (i.e. branches or dendrites) are the source of ions and small droplets. The following discussion will highlight how this conclusion concerning the IL jet is derived.
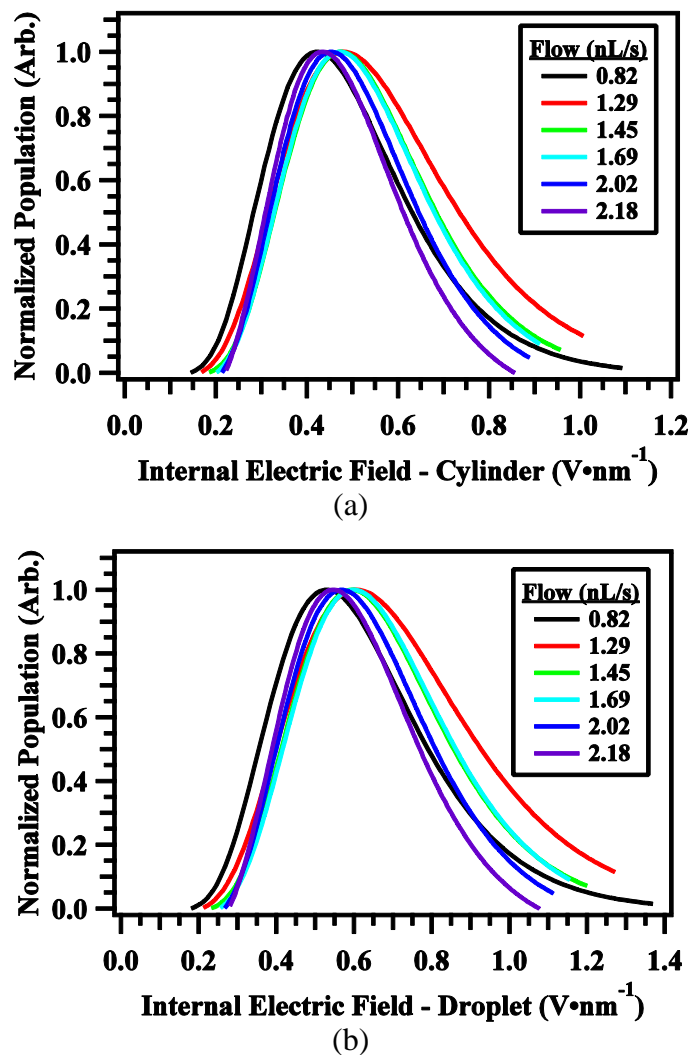
Figure 5.4. The electric field conversion of high mass droplet charge distribution over the normalized population for; (a) the representative jet cylinder volume and (b) the droplet volume.

The first consideration of cone-jet emission is origination of the ions. Looking at Figure 4.5 and Figure 4.7 of the SIMION model, there are limited locations for ions to develop. Low flow rates, near 0.3 nL/s, have two origination locations while flow rates near 2.18 nL/s only have one origination, the tip. Clearly, the ions along the spray centerline and for higher flow rates must be from a source elsewhere besides the transition region. One could assume, in agreement with previous electrospray findings of

large droplets in solute/volatile solvent systems, that the droplets merely undergo Coulombic fission producing small ions. However, the breakup of droplets in such a manner is unlikely given that [Bmim][DCA] (many other ILs included) has a negligible vapor pressure and droplet sizes appear to be well below the established fissional size limit as determined in the above sections [6, 10, 19, 22, 23]. This fact is unlike formamide and other solvents used to dissolve ions into solutions when initial study of cone-jets took place between the 1960's to 1990's. With such solutions, the solvent component of a droplet would evaporate forcing charges closer together, approaching the Rayleigh charge limit, and ultimately disintegrate into randomly sized ions due to repulsion. Fragment ions are apparent in the TOF measurements, as seen in the inset plots of Figure 4.1, despite the absence of these fragments in the [Bmim][DCA] quadrupole mass spectra of Miller *et al*. [11]. This difference between data results suggests that the most likely source of fragmentation in the orthogonal TOF data is due to the 90 deg turn and possible impacts of some species on the flight tube surfaces as well as the longer flight time for fragmented species to propagate compared to the quadrupole system. The fragmentation is only limited to masses under 139 amu/q and no combination of fragment and neutral pair(s) appears to exist above 139 amu/q. Thermally unstable droplets as the source of ions also fall into the same argument as the Coulombic explosion. A variety of ions and fragments should be seen, not defined peaks of $n = 0, 1, 2$, etc. species as in Figure 4.1. As for ions extracted from the droplets by the electric field, that does not occur based on the field drop-off reported by the electric field model. From the jet tip, the field reduces to 0.6 V·nm^{-1} within 14 and 22 nm for 0.3 and 2.18 nL/s, respectively. Such a field beyond those distances is too weak to generate ions. This conclusion on electric fields is supported by the molecular dynamic work of Prince *et al*. where constant electric fields are applied to equilibrated droplets and why the 0.6 V·nm^{-1} limit is used in this study [21].

By eliminating droplets as the source for centerline ions and for ions generated at high flow rates, only field evaporation of the IL at the jet tip remains as the sole source of ions. Again, since the transition region electric field is below the field limit, the ions are not from this region leaving emission from the tip. Based on the field data of Figure 4.7 and Figure 5.4, the electric field at the jet tip becomes sufficient to allow ion emission. In

fact, the angle distribution shown in Figure 4.8 coincides with the appearance of ions in the mass spectra presented. Additionally, the TOF angular ion distributions that correspond with Figure 4.4 (not shown in figure) show that the intensity of ions at 45 deg increases with increasing flow. Finally, the potential drop along the jet structure in Figure 4.6 presents the fact that test ions from the tip are nominally 300 V, as compared to the 500 V expected from the transition region, in excellent agreement with the retarding potential analysis of Miller *et al*. [11].

With the location of ion origination identified, the behavior of the droplets is now considered. Figure 4.4 illustrates the angular divergence of all droplet components as a function of flow rate. Only the low mass droplet distributions are observed at 45 deg. The large mass droplets conform to the expected central axis orientation and are thought of as simply being derived from varicose instability. However, the angular distribution measurements indicate that the jet emission is not only a single jet with varicose, axisymmetric fluid instability otherwise no droplets should be present at high angles. The two distinct *m/q* distributions also rule out uniform droplets of varicose instability. Alternatively, a kink instability of the jet is possible, but a wide distribution across the entire mass and angle ranges would be expected. A kink instability features a laterally whipping jet that breakups into randomly sized droplets.

The droplet distribution data suggest that fluid flow influences emission along centerline and thus the higher mass distribution is seen, but the data also suggest that secondary structures exist for the additional droplets seen elsewhere in the spectra. The low mass component assessed by the two Maxwell Boltzmann distributions represents two distinct droplets with two overlapping charge distributions. The small droplets originating from these secondary structures exhibit independent behavior from that of the behavior of the larger droplet. The obvious behavioral difference is that the smaller droplets are of less mass and thus size (radius < 2.0 nm) than the droplets in the high mass distribution. These low mass distributions are features in spectra of high angles and illustrate a separate charge distribution (q_{Ray} limited to 9 charges) compared against the large mass distribution. Further, the small droplet charge distributions are generated from different electric field conditions that are applied at the emission location of the small

droplets. As the central jet grows in size and fully develops, these secondary droplets disappear as more mass is ejected from the central jet.

Collecting all evidence together leads to the conclusion that a complex emission structure exists at the jet tip. In order to get a wide angular droplet range, the primary jet must break into secondary jets with a central jet that evolves with increased flow. This central jet is responsible for the high mass droplet distributions and its formation leads to the reduction of the other secondary jets as the flow rate changes. These secondary structures are also a source of ions through field evaporation. The exact relationship between the two emission sources is unclear from the data. One possibility is that some structures undergo field evaporation while others are subject to fluid instabilities nominally assumed to be a varicose instability. The other possibility is that the emission is bimodal. This emission would feature the alternation between field evaporation and fluid instability. The fluid instability would essentially disrupt the field evaporation temporarily, but once a droplet is ejected a stable surface would reform and field evaporation would restart. More study is required to provide a definitive answer on the nature of the jet tip and mechanism responsible for secondary structure formation.

6. CONCLUSION

The following details have been revealed by the orthogonal TOF mass spectrometric study and the use of an electrostatic field model of the full plume from a cone-jet of [Bmim][DCA].

1) Clear droplet distributions are seen for the first time within this low flow rate range. Droplets are seen shifting within 2,000 to 40,000 amu/q and 50,000 to 300,000 amu/q with changing flow rate.

2) High mass droplet distribution represents a range of multiply-charged species assuming a single mass value, but with different charge configurations limited up to the Rayleigh charge value.

3) A consistent, uniform electric field condition is applied to the jet tip nominally 0.5 $V \cdot nm^{-1}$. It is this condition that is responsible for the charge and m/q distributions of the droplets.

4) Ion production is apparent within the spectra as well. Distinct intensity peaks of [Bmim][DCA] species of $n = 0$ to 5 are seen in the spectra. Reduction of ion intensity of lower mass ion species is present as well as the growth of the higher mass ion species with increasing flow rate.

5) Breakdown of the beam components reveal an intensity distribution reflective of the current profiles of the ions and droplets as specified by Gamero-Castaño, Fernández de la Mora, and Lozano. Ion and droplet contributions follow two distinct different data trend as the flow rate increases. Ion contribution exponentially decays while the droplet contribution follows a power growth trend with flow rate.

6) Field model shows test ions exist only at the two emission points (transition region and tip) and that the downstream distribution on the detector reflects the distribution seen by Miller *et al*. [11] by limiting the low end of the electric field to 0.6 $V \cdot nm^{-1}$.

7) Initial kinetic energy of the emitted species effects downstream angle distribution. The widest distribution from the jet tip is seen from kinetic energy at 0.1 eV.

8) Droplet production is not limited to centerline, but also appears at high angles. Only the low mass droplet distribution signature detected at high angles.

9) Ion production is not due to Coulombic fission, droplet thermal instability, or droplet field evaporation. IL physical properties and analyzed charge configuration eliminate Coulombic fission while the lack of high massed fragmentation eliminates thermal instability. Droplet field evaporation does not occur due to rapid field drop-off from the tip.

10) Together, the results identify a different/expanded emission mode for a cone-jet structure. Secondary jets are formed from primary jet. These secondary jets are responsible for ion and droplet generation.

REFERENCES

[1] Iribarne, J. V. and Thomson, B. A., "On the Evaporation of Small Ions from Charged Droplets," *The Journal of Chemical Physics*, Vol. 64, No. 6, 1976, pp. 2287-2294.

[2] Cloupeau, M. and Prunet-Foch, B., "Electrohydrodynamic Spraying Functioning Modes: A Critical Review," *Journal of Aerosol Science*, Vol. 25, No. 6, 1994, pp. 1021-1036.

[3] Cloupeau, M. and Prunet-Foch, B., "Electrostatic Spraying of Liquids in Cone-Jet Mode," *Journal of Electrostatics*, Vol. 22, No. 2, 1989, pp. 135-159.

[4] Cloupeau, M. and Prunet-Foch, B., "Electrostatic Spraying of Liquids: Main Functioning Modes," *Journal of Electrostatics*, Vol. 25, No. 2, 1990, pp. 165-184.

[5] Rayleigh, L., "On the Instability of Jets," *Proceeding of the London Mathematical Society*, Vol. 10, No. 1878, pp. 4-13.

[6] Fernández de la Mora, J., "On the Outcome of the Coulombic Fission of a Charged Isolated Drop," *Journal of Colloid and Interface Science*, Vol. 178, No. 1, 1996, pp. 209-218.

[7] Fernández de la Mora, J. and Loscertales, I. G., "The Current Emitted by Highly Conducting Taylor Cones," *Journal of Fluid Mechanics*, Vol. 260, No. 1, 1994, pp. 155-184.

[8] Gamero-Castaño, M. and Fernandez de la Mora, J., "Direct Measurement of Ion Evaporation Kinetics from Electrified Liquid Surfaces," *Journal of Chemical Physics*, Vol. 113, No. 2, 2000, pp. 815-832.

[9] Romero-Sanz, I., Bocanegra, R., Fernandez de la Mora, J. and Gamero-Castaño, M., "Source of Heavy Molecular Ions Based on Taylor Cones of Ionic Liquids Operating in the Pure Ion Evaporation Regime," *Journal of Applied Physics*, Vol. 94, No. 5, 2003, pp. 3599-3605.

[10] Lozano, P. C., "Studies on the Ion-Droplet Mixed Regime in Colloid Thrusters," PhD Dissertation, Aeronautics and Astronautics Dept., Massachusetts Institute of Technology, Cambridge, MA, 2003.

[11] Miller, S. W., Prince, B. D., Bemish, R. J. and Rovey, J. L., "Electrospray of 1-Butyl-3-Methylimidazolium Dicyanamide Under Variable Flow Rate Operations," *Journal of Propulsion and Power*, Vol. 30, No. 6, 2014, pp. 1701-1710.

[12] Higuera, F. J., "Flow Rate and Electric Current Emitted by a Taylor Cone," *Journal of Fluid Mechanics*, Vol. 484, No. 2003, pp. 303-327.

[13] Higuera, F. J., "Ion Evaporation from the Surface of a Taylor Cone," *Physical Review E*, Vol. 68, No. 1, 2003, pp. 016304-1-016304-10.

[14] Carretero, J. and Martinez-Sanchez, M., "Quasi-One-Dimensional Numerical Simulation of a Single-Emitter Colloidal Jet," *38th AIAA/ASME/SAE/ASEE Joint Propulsion Conference & Exhibit*, AIAA Paper 2002-3812, 2002.

[15] Carretero, J. A., Lozano, P. and Martinez-Sanchez, M., "Numerical Simulation of Taylor Cone-Jets and Colloid Thruster Plumes," *Proceedings of the 4th International Spacecraft Propulsion Conference*, Vol. No. 2004, pp. 106.

[16] Borner, A., Wang, P. and Levin, D. A., "Influence of Electrical Boundary Conditions on Molecular Dynamics Simulations of Ionic Liquid Electrosprays," *Physical Review E*, Vol. 90, No. 6, 2014, pp. 063303.

[17] Takahashi, N. and Lozano, P., "Computational Investigation of Molecular Ion Evaporation in Electrospray Thruster," 44th AIAA/ASME/SAE/ASEE Joint Propulsion Conference & Exhibit, AIAA Paper 2008-4533, 2008.

[18] Romero-Sanz, I., Aguirre de Carcer, I. and Fernandez de La Mora, J., "Ionic Propulsion Based on Heated Taylor Cones of Ionic Liquids," *Journal of Propulsion and Power*, Vol. 21, No. 2, 2005, pp. 239-242.

[19] Davis, E. J. and Bridges, M. A., "The Rayleigh Limit of Charge Revisted: Light Scattering from Exploding Droplets," *Journal of Aerosol Science*, Vol. 25, No. 6, 1994, pp. 1179-1199.

[20] Prince, B. D., Fritz, B., A. and Chiu, Y.-H., "Ionic Liquids in Electrospray Propulsion Systems," *Ionic Liquids: Science and Applications*, American Chemical Society, 2012, pp. 27-49.

[21] Prince, B. D., Tiruppathi, P., Chiu, Y.-H. and Maginn, E. J., "Molcular Dynamic Simulations of 1-Ethyl-3-Methylimidazolium Bis(trifluromethylsulfonyl)imide Clusters and Nanodroplets," *Journal of Physical Chemistry A*, Vol. 119, No. 2, 2015, pp. 352-368.

[22] Rayleigh, L., "On the Equilibrium of Liquid Conducting Masses Charged with Electricity," *Philosophical Magazine: Series 5*, Vol. 14, No. 87, 1882, pp. 184-186.

[23] Taflin, D. C., Ward, T. L. and Davis, E. J., "Electrified Droplet Fission and the Rayleigh Limit," *Langmuir*, Vol. 5, No. 2, 1989, pp. 376-384.

[24] Collins, R. T., Sambath, K., T., H. M. and Basaran, O. A., "Universal Scaling Laws for the Disintegration of Electrified Drops," *Proceedings of the National Academy of Sciences of the United States of America*, Vol. 110, No. 13, 2013, pp. 4905-4910.

[25] de Juan, L. and Fernández de la Mora, J., "Charge and Size Distributions of Electrospray Drops," *Journal of Colloid and Interface Science*, Vol. 186, No. 2, 1997, pp. 280-293.

SECTION

2. CONCLUSION

Through the use of a quadrupole and a time-of-flight mass spectrometers, results from the electrospray of the IL [Bmim][DCA] were obtained and quantified. We see for the flow rate range of 0.05 to 2.18 nL/s the emission process change from being nearly ionic with n = 0, 1, 2 species to a complex emission process that includes a variety of ionic species plus three distinct droplets. These droplets possess uniform size and mass, but are represented by wide charge distribution ranges. These distributions in turn result in a measured mass-to-charge ratio that widely varies from 2,000 to 50,000 amu/q and 60,000 to 300,000 amu/q. The lowest mass droplets are slightly charged emanating from source structures less than 1 nm in radius. The largest droplets are highly charged from 20 to 250 charges per drop. This means that while droplets uniform in size, the charge carried is not. The difference in size and mass due to a few hundred charges is irrelevant when the mass of the largest droplets are 4,000,000 to 16,000,000 amu. These droplet charging conditions are a direct result of the applied electric at the tip of the parent jet and represents a field from 0.2 to 1.0 V·nm^{-1}. In all flow rate cases, the nominal electric field on the jet was 0.5 V·nm^{-1}.

Each charged species detected in the electrospray beam has a unique origination point. At these low flow rates, the cone-jet structure does not fully conform to traditional views. The cone-jet in fact has two local maxima for the electric field; one is located at the transition region, the other at the jet tip. It is in this second maximum that the jet deviates from tradition. The jet structure does not exist as a unified jet, but instead has multiple emission points or structures surrounding a central jet. As the flow increases, the central jet produces the large mass droplet reducing the role of the secondary structures for ions and the two smaller droplets. Eventually the jet will assume a unified structure conforming to the traditional view that only one sized droplet is generated from the jet if the flow rate is sufficiently high.

The result of the droplets in the electrospray beam means that there will be trade-offs in electrospray performance when the IL flow rate is adjusted to vary propulsive output. When the IL flow rate is increased, the droplet contribution begins to dominate the beam composition. This droplet domination leads to increased thrust, but with a penalty in efficient use of the IL propellant. At 0.90 nL/s, the thrust and I_{sp} are 1.83 μN and 132 s, respectively. Increasing IL flow rate to 2.18 nL/s only achieves an additional 1.07 μN of thrust at 80 s I_{sp}. Overall the data showed that IL flow rate can be adjusted to change performance just as well as the beam current through voltage variation. Flow rate adjustment does not require a robust electrical system to handle higher voltages (3-20 kV).

VITA

Shawn Wayne Miller was born in Poplar Bluff, Missouri. In 2006, he graduated Magna Cum Laude with a Bachelor's of Science Degree in Aerospace Engineering from University of Missouri-Rolla (named changed to Missouri University of Science and Technology in 2008). He continued his education in graduate school at Missouri S&T and completed a Master of Science in Aerospace Engineering in 2010. For his MS, he used his experience as Program Manager and a member of the propulsion subsystem to provide a description of the management process used by the Missouri S&T Satellite Design Team to develop the nanosatellite configuration. Shawn received the Academy of Mechanical and Aerospace Engineer's Student Excellence Award for his contribution on the Missouri S&T Satellite Design Team. He was awarded a Doctor of Philosophy Degree in Aerospace Engineering in 2015 from Missouri S&T contributing to the enhancement of research from the Aerospace Plasma Laboratory.